ISSN 2222-5617

МІНІСТЕРСТВО ОСВІТИ І НАУКИ УКРАЇНИ

Вісник
Харківського
Національного
Університету
імені В.Н.Каразіна

№ 1135

Серія “Фізика”

Випуск 21

Серія започаткована 1998 р.

Харків 2014

УДК 530.1/539.8

Вісник містить статті, присвячені сучасному стану теоретичних та експериментальних досліджень в галузі фізики Видання призначене для науковців, викладачів, аспірантів та студентів фізичних спеціальностей вищих навчальних закладів та наукових установ

Затверджено до друку рішенням Вченої ради Харківського національного університету імені В.Н.Каразіна (протокол №3 від 19 листопада 2014 р.)

Редакційна колегія:
Головний редактор
Вовк Р.В. - доктор фіз. - мат. наук, професор , ХНУ імені В.Н.Каразіна, Україна
Заступник головного редактора
Єрмолаєв О.М. - доктор фіз.-мат. наук, професор , ХНУ імені В.Н.Каразіна, Україна
Відповідальний секретар
Криловський В.С. - канд. фіз. - мат. наук, доцент, ХНУ імені В.Н.Каразіна, Україна
Редакційна колегія
Агеєв Л.О. - доктор фіз. - мат. наук, професор, ХНУ імені В.Н.Каразіна, Україна
Андерс О.Г. - доктор фіз. - мат. наук, професор, ХНУ імені В.Н.Каразіна, Україна
Бойко Ю.І. - доктор фіз. - мат. наук, професор, ХНУ імені В.Н.Каразіна, Україна
Гуревич Ю.Г. - доктор фіз. - мат. наук, професор, Дослідницький центр, Мексика
Зиман З.З. - доктор фіз. - мат. наук, професор, ХНУ імені В.Н.Каразіна, Україна
Кагановський Ю.С. - доктор фіз. - мат. наук, професор, Бар - Іланський університет, Ізраїль
Камзін А.С. - доктор фіз. - мат. наук, професор, ФТІ імені Іоффе, Росія
Кунцевич С.П. - доктор фіз. - мат. наук, професор, ХНУ імені В.Н.Каразіна, Україна
Милославський В.К. - доктор фіз. - мат. наук, професор, ХНУ імені В.Н.Каразіна, Україна
Пархоменко А.А. - доктор фіз. - мат. наук, професор, ННЦ ХФТИ НАНУ, Україна
Пойда В.П. - доктор тех. наук, професор, ХНУ імені В.Н.Каразіна, Україна
Портной М.Е. - доктор фізики, професор, університет Эксетеру, Великобританія
Рожко А.Ф. - доктор фізики наук, професор, Лондонський центр нанотехнологій, Великобританія
Хронеос Олександр - доктор фізики наук, професор, Империал коледж, Великобританія
Фегер Олександр - доктор фіз. - мат. наук, професор, інститут фізики університету імені Шафарика, Кошице, Словакія
Федоров П.М. - доктор фіз. - мат. наук, професор, ХНУ імені В.Н.Каразіна, Україна
Шехтер Роберт - доктор фіз. - мат. наук, професор, Гетеборгський університет, Швеція
Шкловський В.А. - доктор фіз. - мат. наук, професор, ННЦ ХФТИ НАНУ, Україна
Шкуратов Ю.Г. - член-кор. НАН України, доктор фіз. - мат. наук, професор, ХНУ імені В.Н.Каразіна, Україна
Ямпольський В.А. - член-кор. НАН України, доктор фіз. - мат. наук, професор, ХНУ імені В.Н.Каразіна, Україна

Адреса редакції:
Україна, 61022, Харків, майдан Свободи, 4, Харківський національний університет імені В.Н. Каразіна, фізичний факультет, 057-707-53-83, ruslan.v.vovk@univer.kharkov.ua

Статті пройшли внутрішнє та зовнішнє рецензування.

Свідоцтво про державну реєстрацію КВ №11825-696 ПР від 04.10.2006

© Харківський національний університет
імені В.Н. Каразіна, оформлення, 2014

UDC 530.1/539.8

Bulletin contains articles on the current state of theoretical and experimental research in the field of physics.
The publication is intended for researchers, teachers and students of physical specialties of higher education and research institutions.

Approved for publication by the decision of the Academic Council of Kharkiv Karazin National University. (Minutes № 3 dated November 19, 2014)

Editorial Board
Editor-in-Chief -
Vovk R.V. - Dr. Sci., Prof., V.N. Karazin Kharkiv National University, Ukraine
Deputy Editor-in-Chief -
Yermolaev O.M. - Dr. Sci., Prof., V.N. Karazin Kharkiv National University, Ukraine
Assistant Editor -
Krylovskiy V.S. – Ph.D., Assoc. Prof. , V.N. Karazin Kharkiv National University, Ukraine
Ageev L.O. - Dr. Sci., Prof., V.N. Karazin Kharkiv National University, Ukraine
Anders O.G. - Dr. Sci., Prof., V.N. Karazin Kharkiv National University, Ukraine
Boiko Yu.I. - Dr. Sci., Prof., V.N. Karazin Kharkiv National University, Ukraine
Gurevich Yu.G. - Dr. Sci., Prof., Center for Research and Advanced, Mexico
Zyman Z.Z. - Dr. Sci., Prof., V.N. Karazin Kharkiv National University, Ukraine
Kaganovskiy Yu.S. - Dr. Sci., Prof., Bar - Ilan University, Israel
Kamzin A.S. - Dr. Sci., Prof., Ioffe Institute, Russia
Kuncevich S.B. - Dr. Sci., Prof., V.N. Karazin Kharkiv National University, Ukraine
Miloslavskii V.K. - Dr. Sci., Prof., V.N. Karazin Kharkiv National University, Ukraine
Parhomenko A.A. - Dr. Sci., Prof., NSC "Kharkov Institute of Physics & Technology", Ukraine
PoidaV.P. - Dr. Sci., Prof., V.N. Karazin Kharkiv National University, Ukraine
Portnoi M. E - Dr. Sci., Prof., University of Exeter, UK
Rozhko A.Ф. - Dr. Sci., Prof., London Centre for Nanotechnology, UK
Chroneos A. - Dr. Sci., Prof., Imperial Colledge, UK
Feher A. - Dr. Sci., Prof., , Pavol Jozef Šafárik University in Košice, Kosice, Slovakia
Shekhter R.I. - Dr. Sci., Prof., University of Goteborg, Sweden
Shklovskij V. A. - Dr. Sci., Prof., NSC "Kharkov Institute of Physics & Technology", Ukraine
Shkuratov J.G.- Corresponding Member of the NAS of Ukraine, Dr. Sci., Prof., V.N. Karazin Kharkiv National University, Ukraine
Yampol'skii V. A. - Corresponding Member of the NAS of Ukraine, Dr. Sci., Prof., V.N. Karazin Kharkiv National University, Ukraine

Editorial address:
Svobody Sq. 4, 61022, Kharkiv, Ukraine, V.N. Karazin Kharkiv National University, Department of Physics, 057-707-53-83,ruslan.v.vovk@univer.kharkov.ua
All articles reviewed.
Certificate of state registration of CT number 11825-696 PR on 04/10/2006

© V.N. Karazin Kharkiv National University,
design, 2014

Content

Вісник ХНУ, № 1135, серія «Фізика», вип. 21, 2014. с. 6-9

УДК: 538.915, 538.975.
PACS: 71.10.Pm, 72.10.-d, 72.15.Lh, 73.20.Qt.

Scattering process without conserving plasmon number in one-dimensional Wigner crystal

S. S. Apostolov

V. N. Karazin Kharkiv National University,
Svobody Sq. 4, 61022, Kharkiv, Ukraine

In this paper we consider a quantum wire, the electrons in which form a one-dimensional Wigner crystal. One-dimensional electrons in a crystal are equivalent to plasmon modes describing the long-wavelength fluctuations of the charge density. We have studied the basic process of the plasmon scattering that is not conserved the total number of particles, – the scattering of two plasmons in three, and vice versa. For this process, the scattering rate is calculated and an equation for the relaxation of the artificial chemical potential are derived.

Keywords: one-dimensional Wigner crystal, plasma waves, collision integral, chemical potential.

В работе рассмотрен квантовый провод, электроны в котором формируют одномерный вигнеровский кристалл. Одномерные электроны в таком кристалле эквивалентны системе плазмонных мод, описывающих длинноволновые колебания зарядовой плотности. В работе исследован основной процесс рассеяния плазмонов, при котором не сохраняется полное число частиц, – процесс рассеяния двух плазмонов в три, и наоборот. Для этого процесса вычислена амплитуда рассеяния и получено уравнение для релаксации искусственно созданного химического потенциала.

Ключевые слова: одномерный вигнеровский кристалл, плазменные волны, интеграл столкновений, химический потенциал.

У роботі розглянуто квантовий дріт, електрони в якому формують одновимірний вігнеровський кристал. Одновимірні електрони у такому кристалі еквівалентні системі плазмонних мод, що описують довгохвильові коливання зарядової густини. У роботі досліджено основний процес розсіювання плазмонів, при якому не зберігається повне число частинок, – процес розсіювання двох плазмонів в три, і навпаки. Для цього процесу обчислена амплітуда розсіювання та отримано рівняння для релаксації штучно створеного хімічного потенціалу.

Ключові слова: одновимірний вігнеровський кристал, плазмові хвилі, інтеграл зіткнень, хімічний потенціал.

Introduction

One of the key areas of modern research is the kinetics of the nearly integrable quantum many-body systems. From this perspective the one-dimensional (1D) systems are particularly relevant as some exact solutions are known [1-2] that can be used to solve more general models in which integrability is broken weakly. Integrability ensures that the scattering of particles in 1D many-particle system is exactly equivalent to the sequence of the pair-particle collisions, and hence the set of initial momenta for each scattering event coincides with the set of finite momenta. Such scattering does not change the distribution function and are unable to lead the system to thermal equilibrium. A striking example of such long-lived non-equilibrium quantum states is a quantum Newton pendulum created using 1D-Bose gas in a trap [3].

To describe the 1D electron crystals (Wigner crystals) that are formed in the quantum wires, the nanotubes and the edge states, we can use exactly solvable Tomonaga-Luttinger model [4-6]. This model predicts the special properties of 1D electron systems: the power-law anomalies in the tunneling density of states [7] and the effect of charge and spin separation [8]. However, this model has some serious deficiencies. Particularly in the framework of the model excitations have an infinite lifetime, which implies a lack of equilibration.

Renewed interest in 1D electron crystals stems from the new experimental results that do not fit into the paradigm of the Tomonaga-Luttinger model. Tunneling spectroscopy of quantum wires [9,10] and thermometry of quantum edge states [11,12] are a direct proof of thermal equilibrium in 1D electron systems. The deviations from perfect conductance quantization [13-17] and a violation of the Wiedemann-Franz law [18,19] in the wires with a low electron density are found. These observations have attracted considerable attention and require construction of a new theoretical model.

In the present paper we study the microscopic mechanisms of relaxation in the generalized Tomonaga-Luttinger description of one-dimensional electron liquids, which amounts to keeping anharmonic interactions between plasmons. We follow and extend the way used in [20]. The 1D Wigner crystal [21-22] represents an extreme case of the Tomonaga-Luttinger liquid with small interaction parameter $\kappa = \pi\hbar\nu^2/ms \ll 1$. Here ν is particle density, m is electron mass, s is sound velocity of plasmons.

We model the system of strongly interacting spinless electrons of mass m by the Hamiltonian (hereafter $\hbar = 1$)

$$H = \sum_l \frac{p_l^2}{2m} + \frac{1}{2}\sum_{l \neq l'} U(x_l - x_{l'}), \tag{1}$$

where p_l and x_l are the momentum and coordinate of the l th particle, and $V(x)$ is the interaction potential.

In order to involve the standard second-quantized representation we expand (1) with respect to small $u_l - u_{l'}$, which measures deviations of electrons from their respective equilibrium positions $x_l = l/\nu + u_l$, and introduce collective coordinates

$$\begin{aligned} u_l &= \sum_q \sqrt{\frac{1}{2mN\omega_q}}(b_q + b_{-q}^\dagger)e^{iql}, \\ p_l &= -i\sum_q \sqrt{\frac{m\omega_q}{2N}}(b_q - b_{-q}^\dagger)e^{iql}, \end{aligned} \tag{2}$$

where N is a number of electrons in a crystal, and plasmon creation and annihilation operators obey canonical commutation relations

$$\left[b_q, b_{q'}\right] = 0, \quad \left[b_q^\dagger, b_{q'}^\dagger\right] = 0, \quad \left[b_q, b_{q'}^\dagger\right] = \delta_{qq'},$$

The resulting Hamiltonian consists of the usual Wigner crystal part

$$H_0 = \sum_q \omega_q (b_q^\dagger b_q + 1/2), \tag{3}$$

and anharmonic terms discussed in the next section in details. Here the plasmon dispersion is given by

$$\omega_k^2 = \frac{2}{m}\sum_l V''(x = l/n)[1 - \cos(kl/n)]. \tag{4}$$

At the sufficiently small temperatures T the characteristic value of plasmon momentum q is small also, and we can simplify the dispersion relation to

$$\omega_q = s|q|(1 - \alpha q^2), \quad q \sim T/s \ll 1.$$

Here $s = \sqrt{V_{22}/m}$, $\alpha = V_{24}/24V_{22}$, and

$$V_{mn} = \sum_{l=1}^{\infty} V_l^{(m)} l^n, \quad V_l^{(m)} = V^{(m)}(x = l/n).$$

The nonlinearity of the dispersion strictly prohibits the decay of a single boson into two or more because of the momentum and energy conservation. The simplest scattering process involves two bosons both in the initial and in the final states and the typical relaxation rate scales as the fifth power of temperature [20]. Essential feature of the two-into-two process is the conserving of the number of plasmons. So, this process leads the system to not-exact equilibrium state. Indeed, the resulting "equilibrium" distribution function is expected to have a chemical potential. Below we discuss the two-into-three process which changes the number of plasmons and thereby relaxes the chemical potential.

Two-into-three scattering process

As discussed in the introduction we expand the Hamiltonian H with respect to deviations $u_l - u_{l'}$ keeping terms up to the fifth order, $H \approx H_0 + H_3 + H_4 + H_5$,

$$\begin{aligned} H_{n=3,4,5} &= \frac{1}{2\cdot n!}\sum_{ll'} V_l^{(n)}(u_{l+l'} - u_{l'})^n \\ &= \frac{i^n N}{n(2mN)^{n/2}} \sum_{q_1,\dots,q_{n-1}} \frac{\phi_n(q_1,\dots,q_{n-1})}{\sqrt{\omega_{q_1}\dots\omega_{q_{n-1}}\omega_{\bar{q}_n}}} \\ &\quad \times (b_{q_1} + b_{-q_1}^\dagger)\dots(b_{q_{n-1}} + b_{-q_{n-1}}^\dagger)(b_{\bar{q}_n} + b_{-\bar{q}_n}^\dagger), \end{aligned} \tag{5}$$

where $\bar{q}_n = q_1 + \dots + q_{n-1}$ and

$$\begin{aligned} \phi_n(q_1,\dots,q_{n-1}) &= -2^{n-1}\sum_{l=1}^{\infty} V_l^{(n)} \sin(\bar{q}_n l/2) \\ &\quad \times \sin(q_1 l/2)\dots\sin(q_{n-1}l/2). \end{aligned}$$

The leading order inelastic scattering process that not conserving the plasmon numbers, involves two plasmons in the initial state and three plasmons in the final, or vise versa. The corresponding rate is generated to the first order in the interaction Hamiltonian H_5, to the second order in the crossed terms between H_3 and H_4, and finally from H_3 iterated to the third order. For the purpose of finding this rate we introduce $\mathcal{T}$-matrix

$$\mathcal{T} = H_5 + H_4 G_0 H_3 + H_3 G_0 H_4 + H_3 G_0 H_3 G_0 H_3, \tag{6}$$

where $G_0 = (\Omega\ - H_0)$, with energy Ω_i of the initial plasmons. Then the transition rate for plasmon scattering is defined by $\mathcal{T}$-matrix and given by the Fermi golden rule expression

$$W_{Q_i}^{Q_f} = 2\pi|\langle Q_f|\mathcal{T}|Q_i\rangle|^2\,\delta(\Omega_f - \Omega_i), \tag{7}$$

where $Q_{i/f}$ and $\Omega_{i/f}$ abbreviate total initial/final momenta and energies of the plasmons respectively.

Scattering rate

The detailed calculation of the transition rate is cumbersome and technically. Here we shortly describe the steps taken to calculate the rate. After applying Eq. (5) into Eq. (6) and then into Eq. (7) we express the matrix element

$\langle Q_f \,|\, \mathcal{T} \,|\, Q_i \rangle$ as a sum of the averaged products of the creation and annihilation operators. Each of these averaged products can be reduced by commutation relations to the composition of Kronecker's delta symbols. As a result we get the transition rate in the following form

$$W_{Q_i}^{Q_f} = 2\pi \,|\, A_{Q_i}^{Q_f} \,|^2 \, \delta_{Q_i, Q_f} \delta(\Omega_i - \Omega_f), \tag{8}$$

where amplitude of the scattering rate can be written in the following form,

$$A_{q_1', q_2', q_3'}^{q_1, q_2} = A_{q_1, q_2}^{q_1', q_2', q_3'} = \frac{\lambda_{q_1, q_2}^{q_1', q_2', q_3'} v^3}{(Nm)^{3/2} s^{1/2}} \,|\, q_1 q_2 q_1' q_2' q_3' \,|^{1/2}, \tag{9}$$

and

$$\begin{aligned} &\lambda_{q_1, q_2}^{q_1', q_2', q_3'} \\ &= \frac{(2s)^{1/2}}{4m^3 v^3} \prod_{\substack{q = q_1, q_2, \\ q_1', q_2', q_3'}} \left| q\omega_q \right|^{-1/2} \Big[m^2 \phi_5(q_1, q_2, -q_1', -q_2') \\ &\quad - \frac{m}{6} \sum_{\{p\} = \{q\}} \Phi^{\pm}(p_1, p_2) \phi_4(p_3, p_4, p_5) \\ &+ \sum_{\{p\} = \{q\}} \Phi^{\pm}(p_1, p_2) \Phi^{\pm}(p_3, p_4) \phi_3(p_5, p_1 + p_2) \Big]. \end{aligned} \tag{10}$$

Here the summation over $\{p\} = \{q\}$ means the summation over variables $p_{1,2,3,4,5}$ taking different value from set of initial momenta $q_{1,2}$ and final momenta with the opposite sign $-q_{1,2,3}'$. In other words the sets of $\{p\}$ and $\{q\}$ coincide,

$$\{p_1, p_2, p_3, p_4, p_5\} = \{q_1, q_2, -q_1', -q_2', -q_3'\}.$$

Then the sign "$\pm$" in superscript of $\Phi^{\pm}(p_1, p_2)$ should be chosen as "$+$" if p_1 and p_2 is the both initial or final momenta and "$-$" otherwise,

$$\Phi^{\pm}(p_1, p_2) = \frac{\phi_3(p_1, p_2)}{(\omega_{p_1} \pm \omega_{p_2})^2 - \omega_{p_1 + p_2}^2}.$$

Equation (8), (9), and (10) describe the scattering of plasmons with arbitrary possible momenta. However expression for $\lambda_{q_1, q_2}^{q_1', q_2', q_3'}$ is crucially simplified in the low temperature limit. In this limit the plasmon momentum $q \sim T / s \ll 1$, and within the leading logarithmic accuracy $\lambda_{q_1, q_2}^{q_1', q_2', q_3'}$ is independent of momenta.

For example,

$$\lambda_{q_1, q_2}^{q_1', q_2', q_3'} \equiv \lambda = 55\sqrt{2} / 48 \approx 1.62,$$

in the case of the screened Coulomb interaction potential,

$$V(x) = \frac{e^2}{|x|} - \frac{e^2}{\sqrt{x^2 + 4d^2}}.$$

where $d \gg v^{-1}$ is a distance to screen and e is an elementary charge.

Relaxation of the artificial chemical potential

Now we assume that the crystal is brought out from equilibrium. The main scattering process that relaxes the crystal is the two-in-two process studied in [20]. This process conserves the number of plasmons and therefore drives the distribution function n_q of the plasmons to Fermi-like distribution

$$n_q = [e^{(\omega_q - \mu)/T} - 1]^{-1}, \tag{11}$$

where μ is artificial chemical potential that should relax to zero due to the two-to-three scattering process.

The evolution of the distribution function can be described by Boltzmann equation

$$\frac{\partial n_q}{\partial t} = \mathcal{I}[n_q], \tag{12}$$

where $\mathcal{I}[n_q]$ is the collision integral that corresponds to the two-to-three scattering process,

$$\begin{aligned} \mathcal{I}[\mathrm{n}_q] = &\sum_{q_1 > q_2} \sum_{q_2' > q_3'} W_{q_1, q_2}^{q, q_2', q_3'} n_{q_1, q_2}^{q, q_2', q_3'} \\ &- \sum_{q_2} \sum_{q_1' > q_2' > q_3'} W_{q, q_2}^{q_1', q_2', q_3'} n_{q, q_2}^{q_1', q_2', q_3'}, \end{aligned}$$

$$n_{q_1, q_2}^{q_1', q_2', q_3'} = n_{q_1} n_{q_2} \overline{n}_{q_1'} \overline{n}_{q_2'} \overline{n}_{q_3'} - \overline{n}_{q_1} \overline{n}_{q_2} n_{q_1'} n_{q_2'} n_{q_3'},$$

with $\overline{n}_q = 1 + n_q$.

In order to simplify Eq. (12) we summarize it over q,

$$\frac{\partial}{\partial t} \sum_q n_q = \frac{1}{12} \sum_{\substack{q_1, q_2 \\ q_1', q_2', q_3'}} W_{q_1, q_2}^{q_1', q_2', q_3'} n_{q_1, q_2}^{q_1', q_2', q_3'},$$

and substitute Eq. (11) in it. Finally we get

$$\frac{\partial}{\partial t} \frac{T}{|\mu|} = \tau_0^{-1} \equiv \frac{\pi}{386} \frac{s}{T} \frac{1}{N} \sum_{\substack{q_1, q_2 \\ q_1', q_2', q_3'}} \frac{W_{q_1, q_2}^{q_1', q_2', q_3'}}{\prod_{\substack{q = q_1, q_2 \\ q_1', q_2', q_3'}} \sinh \frac{\omega_q}{2T}}. \tag{13}$$

Here we assume that the crystal is near equilibrium, so chemical potential is small enough, $|\mu| \ll T$, and it is negative to prevent the distribution function from singularity.

In order to calculate the characteristic time τ_0 that determine the relaxation of the artificial chemical potential, we should examine the kinematics of the two-in-three scattering process.

Kinematic constraints

Here we study the kinematics of the two-to-three scattering process and determine the combination of momenta that contributes substantially into the collision integral and τ_0. Now we assume that $q_1 > 0$ (case of $q_1 < 0$ can be studied analogously). The momenta and energy conservation laws give

$$\begin{aligned} & q_1' + q_2' + q_3' = q_1 + q_2, \\ & |q_1'|(1-\alpha q_1'^2) + |q_2'|(1-\alpha q_2'^2) + |q_3'|(1-\alpha q_3'^2) \\ & \quad = |q_1|(1-\alpha q_1^2) + |q_2|(1-\alpha q_2^2). \end{aligned} \quad (14)$$

The first equation sets $\delta_{Q_i,Q_f} = \delta_{q_3', q_1+q_2-q_1'-q_2'}$. In the case when all momenta is positive $q_{1,2}, q_{1,2,3}' > 0$ the nonlinearity plays the key role because the linear terms in Eq. (14) cancel each other and, excluding q_3', we get the quadratic equation for q_2',

$$\begin{aligned} & (q_1 + q_2 - q_1')q_2'^2 - (q_1 + q_2 - q_1')^2 q_2' \\ & \quad + (q_1 - q_1')(q_2 - q_1')(q_1 + q_2) = 0. \end{aligned} \quad (15)$$

Then the energy δ-function transforms into

$$\delta(\Omega_i - \Omega_f) = \frac{\delta(q_2' - q_+) + \delta(q_2' - q_-)}{3s\alpha(q_+^2 - q_-^2)}, \quad (16)$$

where $q_\pm$ are the roots of the quadratic equation (15).

In all other cases when one or several momenta are negative linear terms in Eq. (14) do not cancel each other and do not produce such denominator as in Eq. (16). For example, assume that $q_2' < 0$ and $q_{1,2}, q_{1,3}' > 0$. Then the energy conservation gives

$$\begin{aligned} & \delta(\Omega_i - \Omega_f) \\ & \quad = \frac{1}{s}\delta[q_2' + 3\alpha(q_1 + q_2)(q_1' - q_1)(q_1' - q_2)/2]. \end{aligned}$$

Comparing the last equation with Eq. (16) one can conclude that the contribution in τ_0, Eq. (13), is much smaller to factor $\alpha(q_+^2 - q_-^2) \sim (T/s)^2 \ll 1$ in the denominator in Eq. (16) when momenta are of different signs. Then in the further calculation we assume all momenta to be of the same sign.

Calculation of characteristic time

Now we can calculate the characteristic time τ_0. For that purpose we apply the scattering rate in the form of Eqs. (8) and (9) into Eq. (13) and integrate only over momenta of the same sign,

$$\tau_0^{-1} = \lambda \mathcal{I} \kappa^3 \alpha^{-1} s (T/2\pi s)^5.$$

where $\mathcal{I}$ is a dimensionless integral originated from the sum over momenta in Eq. (13),

$$\mathcal{I} = \frac{8}{9} \iiint\limits_{\substack{x_{1,2,3} > 0 \\ x_\pm > 0}} \frac{dx_1 dx_2 dx_3 (x_+^2 - x_-^2)^{-1}}{\zeta(x_1)\zeta(x_2)\zeta(x_3)\zeta(x_+)\zeta(x_-)} \approx 1.814, \quad (17)$$

with $\zeta(x) = x^{-1}\sinh x$, and $x_\pm$ are roots of Eq. (15) with q changed to x,

$$x_\pm = \frac{x_1 + x_2 - x_3}{2}\Big[1 \pm \sqrt{\frac{4(x_1^3 + x_2^3 - x_3^3)}{3(x_1 + x_2 - x_3)^3} - \frac{1}{3}}\Big].$$

It should be noted that integration in Eq. (17) performed over domain where $x_{1,2,3} > 0, x_\pm > 0$.

Conclusions

In the present paper we study the scattering of the plasmons in the one-dimensional Wigner crystal. The leading process involves two plasmons in the both initial and final states and, therefore, conserves the number of the plasmons. This process drives the crystal to the non-exact equilibrium that can possess the artificial chemical potential. This chemical potential should be relaxed by the process that not conserving the plasmon number. The main process of such a kind involves two plasmons in the initial state and three in the final, or vice versa. We determine the scattering rate of this process, derive equation of relaxation of the artificial chemical potential, and calculate the characteristic time of the relaxation.

1. D.C. Mattis. The Many-Body Problem: An Encyclopedia of Exactly Solved Models in One Dimension, World Scientific Publishing (1993), 984 p.
2. B. Sutherland. Beautiful models: 70 years of exactly solved quantum many-body problems, World Scientific Publishing (2004), 400 p.
3. T. Kinoshita, T. Wenger, D. Weiss. Nature, 440, 900 (2006).
4. S. Tomonaga. Prog. Theor. Phys., 5, 544 (1950).
5. J.M. Luttinger. J. Math. Phys., 4, 1154 (1963).
6. V.V. Deshpande et al. Nature, 464, 209 (2010).
7. L. Venkataraman, Y.S. Hong, P. Kim, Phys. Rev. Lett., 96, 076601 (2006).
8. O.M. Auslaender et al. Science, 308, 88 (2005).
9. Y.-F. Chen et al. Phys. Rev. Lett., 102, 036804 (2009).
10. G. Barak et al. Nat. Phys., 6, 489 (2010).
11. G. Granger, J.P. Eisenstein, J.L. Reno. Phys. Rev. Lett., 102, 086803 (2009).
12. C. Altimiras et al. Nat. Phys., 6, 34 (2010).
13. K.J. Thomas et al. Phys. Rev. Lett., 77, 135 (1996); Phys. Rev., B58, 4846 (1998).
14. A. Kristensen et al. Phys. Rev., B62, 10950 (2000).
15. S.M. Cronenwett et al. Phys. Rev. Lett., 88, 226805 (2002).
16. D.J. Reilly et al. Phys. Rev., B63, 121311(R) (2001).
17. R. Crook et al. Science, 312, 1359 (2006).
18. O. Chiatti et al. Phys. Rev. Lett., 97, 056601 (2006).
19. N. Wakeham et al. Nat. Commun., 2, 396 (2011).
20. J. Lin, K.A. Matveev, and M. Pustilnik. Phys. Rev. Lett., 110, 016401 (2013).
21. H.J. Schulz. Phys. Rev. Lett., 71, 1864 (1993).
22. K.A. Matveev. Phys. Rev., B70, 245319 (2004).

Вісник ХНУ, № 1135, серія «Фізика», вип. 21, 2014. с. 10-15

PACS: 73.63.Fg Nanotubes;
73.21.Cd Superlattices;
71.45.d Collective effects;
73.20.Mf Collective excitations (including plasmons and other charge - density excitations).
УДК: 538.11

Transparency windows for plasma waves on the surface of the nanotube with a superlattice

A.M. Ermolaev, G.I. Rashba

Kharkiv National University named after V.N. Karazin
Svobody sq., 4, Kharkov, 61022, Ukraine
alexander.m.ermolaev@univer.kharkov.ua
georgiy.i.rashba@univer.kharkov.ua

Within the framework of the model electron energy spectrum on the nanotube surface with a superlattice in a magnetic field, an exact expression for the polarization operator of a degenerate electron gas was obtained. The shape and size of the plasma waves Landau damping regions on the tube throughout the Brillouin zone were calculated. The influence on these areas of the position of Fermi level in the miniband was considered. The conditions for the resonance absorption of plasmon on the tube by electrons were found. The limiting transition towards the nanotube without superlattice was performed.

Keywords: nanotube, superlattice, magnetic field, plasma waves, Landau damping.

На основе модельного спектра энергии электронов на поверхности нанотрубки со сверхрешеткой в магнитном поле получено точное выражение для поляризационного оператора вырожденного электронного газа. Рассчитаны форма и размеры областей затухания Ландау плазменных волн на трубке во всей зоне Бриллюэна. Рассмотрено влияние на эти области положения уровня Ферми в минизоне. Найдены условия резонансного поглощения плазмонов на трубке электронами. Выполнен предельный переход к нанотрубке без сверхрешетки.

Ключевые слова: нанотрубка, сверхрешетка, магнитное поле, плазменные волны, затухание Ландау.

На основі модельного спектру енергії електронів на поверхні нанотрубки з надграткою у магнітному полі отримано точний вираз для поляризаційного оператора виродженого електронного газу. Розраховані форма і розміри областей згасання Ландау плазмових хвиль на трубці у всій зоні Бриллюена. Розглянуто вплив на ці області положення рівня Фермі у мінізоні. Знайдені умови резонансного поглинання плазмонів на трубці електронами. Виконаний граничний перехід до нанотрубки без надгратки.

Ключові слова: нанотрубка, надгратка, магнітне поле, плазмові хвилі, згасання Ландау.

Introduction

After the emergence of the idea of Keldysh [1] on the establishment of an additional crystal periodic potential and its realization in layered semiconductor structures [2,3] have passed fifty years. However, interest in this system, called the superlattices (SL), continues unabated. The number of articles, reviews and monographs on semiconductor superlattice is steadily increasing [4-15]. The suggested by Keldysh perspective to control band spectrum of a solid proved tempting. The technical applications of SL is very broad . In recent years the physics of solid state enriched set of effects and technical applications due to study of SL.

In Refs. [5,6] the de Haas-van Alphen effect in layered conductors with additional periodic potential which perpendicular to the layers changes.

In Ref. [11] the electromagnetic waves in the SL in a magnetic field were considered. The spectrum of low-frequency oscillations of the field in conditions of the quantum Hall effect was obtained. This effect is observed experimentally in SL GaAs / (AlGa) in magnetic field which perpendicular to the axis of the superlattice. The undamped helicons in SL were predicted. They do not damped because the dissipative components of the conductivity tensor under certain values of the magnetic field strength equals zero. Besides, under the frequencies of fields which less than the electron cyclotron frequency, there is no Landau damping. Thanks to the non-dissipative motion of electrons in the SL the spectrum and polarization of electromagnetic waves in it are of an unusual character.

In Ref. [12] it is shown that in the SL in a magnetic field it is possible metal-insulator transition due to the dependence of the density of states of electrons on the magnetic field. This article calculates the magnetic field values at which the dissipative components of the conductivity tensor of the electron gas vanish. The dependence of the photoconductivity of SL on the magnetic field was considered. In Ref. [13] the thermodynamic functions of the SL in the magnetic field for the degenerate and nondegenerate electron gas were calculated. A new method of adiabatic cooling of the sample was suggested.

In Refs. [2-15] the one-dimensional superlattice with additional periodic potential depending on one coordinate were considered. The new surge of interest in CP associated with the discovery of carbon [16] and semiconductor [17] nanotubes. There was a need to consider the SL on the surface of the tube. The SL with cylindrical symmetry may be radial and longitudinal. The radial SL is a set of coaxial cylinders. The longitudinal SL is similar to the system of coaxial rings strung on the axis of the cylinder. Such SL can exist on a tube filled with fullerenes or metal atoms [18-20].

Landau damping of plasma waves in the degenerate and nondegenerate electron gas on the surface of the nanotubes in a longitudinal magnetic field in the absence of the superlattice is considered in the paper [21]. The authors of this paper calculated the longitudinal dielectric function of the electron gas on the tube. Restricting ourselves investigation taken into account only the intraband transitions of electrons, they found the Aharonov-Bohm oscillations of the dielectric constant.

In Refs. [22,23] the long-wave plasma oscillations on the tube with a superlattice were considered. In these articles, the transparency windows for plasma waves is considered only for certain values of the wave vector and the frequency of the waves. Here, within the established in the article [22] model, we present the results of calculating the position and shape of the region of Landau damping plasma waves in the whole plane wavenumber-frequency.

The polarization operator of the electron gas

The energy of the electron with the effective mass m_* on the surface of a cylindrical nanotube in a magnetic field parallel to its axis, is calculated by Kulik taking into account the quantization of radial motion of electrons in a tube of small thickness [24]:

$$\varepsilon_{lk} = \varepsilon_0 (l+\eta)^2 + \frac{\hbar^2 k^2}{2m_*}, \qquad (1)$$

where $\hbar l$ and $\hbar k$ – the projection of the angular momentum and momentum of electron on the tube axis, $\varepsilon_0 = \hbar^2 / 2m_* a^2$ – rotational quantum, a – the radius of the tube, $\eta = \Phi / \Phi_0$ – the ratio of the magnetic flux Φ through the cross section of the tube to the flux quantum $\Phi_0 = 2\pi c\hbar / e$ [24]. The equation (1) describes a set of one-dimensional adjoining subbands whose boundaries $\varepsilon_l = \varepsilon_0 (l+\eta)^2$ coincide with the quantized energy levels of the circular motion of the electrons on the tube in the magnetic field. The electron density of states has a root singularity at the boundary of the subzone. The simplest way to take into account the superlattice on the tube is to replace the energy of the longitudinal motion of the electron in the formula (1) to the expression

$$\varepsilon_k = \Delta(1-\cos kd). \qquad (2)$$

This expression is borrowed from the theory of the strong coupling of electrons with the lattice, and is often used in the theory of superlattices and layered crystals [15,25,26]. As a result of such a substitution the electron spectrum on the tube becomes

$$\varepsilon_{lk} = \varepsilon_0 (l+\eta)^2 + \Delta(1-\cos kd), \qquad (3)$$

where d – period of superlattices, 2Δ – band width in the energy spectrum of the longitudinal motion of the electron. This band corresponds to the values of the wave number k in the first Brillouin zone $-\pi/d \le k \le \pi/d$. The spectrum (3) describes the set of allowed energy region of electron inside the intervals $\varepsilon_l \le \varepsilon \le 2\Delta$, separated by gaps. By analogy with traditional superlattice these bands are called minibands. The electron density of states has a root singularity at the miniband boundaries [27].

In the random phase approximation the damping decrement of plasma waves with angular momentum $\hbar m$ and the wave number q on the tube is equal to [22]

$$\gamma_m(q) = \frac{\operatorname{Im} P_m(q,\omega)}{\frac{\partial}{\partial\omega} \operatorname{Re} P_m(q,\omega)} \bigg|_{\omega=\omega_m(q)}, \qquad (4)$$

where $P_m(q,\omega)$ – the polarization operator of electron gas, $\omega_m(q)$ – plasmon spectrum. The polarization operator is equals

$$P_m(q,\omega) = \frac{1}{\pi a L} \sum_{lk} \frac{f\left(\varepsilon_{(l+m)(k+q)}\right) - f\left(\varepsilon_{lk}\right)}{\varepsilon_{(l+m)(k+q)} - \varepsilon_{lk} - \hbar\omega - i0}, \qquad (5)$$

where $f(\varepsilon)$ – Fermi function, L – the length of the tube.

The dispersion equation for the spectrum and damping of plasma waves has the form

$$1-\upsilon_m(q)P_m(q,\omega)=0, \tag{6}$$

where

$$\upsilon_m(q)=4\pi e^2 a \mathrm{I}_m(qa)\mathrm{K}_m(qa) \tag{7}$$

– cylindrical harmonic of electron Coulomb potential on the tube, I_m and K_m – modified Bessel functions, e – the electron charge.

If the electron gas is degenerate, the integration with respect k in the formula (5) is limited to an interval $[-k_l, k_l]$, where

$$k_l=\frac{1}{d}\arccos\left(\frac{\varepsilon_l+\Delta-\mu_0}{\Delta}\right) \tag{8}$$

– the maximum wave number of electrons in a partially filled miniband with the number l, μ_0 – the Fermi energy. The resulting integration over the k the l-miniband contribution to the real part of the polarization operator is defined by parameters

$$c_\pm=\frac{\hbar(\omega-\Omega_\pm)}{2\Delta\sin\frac{qd}{2}}. \tag{9}$$

Here

$$\hbar\Omega_\pm(l,m)=\varepsilon_0 m\left[2(l+\eta)\pm m\right], \tag{10}$$

Ω_+ – the frequency of direct transitions of electrons $l\to l+m$ between the miniband of the spectrum (3).

If $c_\pm^2<1$, from the formula (5) we obtain

$$\begin{aligned}\operatorname{Re}P_{lm}(q,\omega)&=-\frac{1}{4\pi^2 ad\Delta\sin\frac{qd}{2}}\\
&\left\{\frac{1}{\sqrt{1-c_+^2}}\left[\ln\left|\frac{c_+\mathrm{tg}\frac{1}{2}\left(x_l+\frac{qd}{2}\right)-\left(1-\sqrt{1-c_+^2}\right)}{c_+\mathrm{tg}\frac{1}{2}\left(x_l+\frac{qd}{2}\right)-\left(1+\sqrt{1-c_+^2}\right)}\right|-\right.\right.\\
&\left.-\ln\left|\frac{c_+\mathrm{tg}\frac{1}{2}\left(-x_l+\frac{qd}{2}\right)-\left(1-\sqrt{1-c_+^2}\right)}{c_+\mathrm{tg}\frac{1}{2}\left(-x_l+\frac{qd}{2}\right)-\left(1+\sqrt{1-c_+^2}\right)}\right|\right]-\\
&-\frac{1}{\sqrt{1-c_-^2}}\left[\ln\left|\frac{c_-\mathrm{tg}\frac{1}{2}\left(x_l-\frac{qd}{2}\right)-\left(1-\sqrt{1-c_-^2}\right)}{c_-\mathrm{tg}\frac{1}{2}\left(x_l-\frac{qd}{2}\right)-\left(1+\sqrt{1-c_-^2}\right)}\right|-\right.\\
&\left.\left.-\ln\left|\frac{c_-\mathrm{tg}\frac{1}{2}\left(-x_l-\frac{qd}{2}\right)-\left(1-\sqrt{1-c_-^2}\right)}{c_-\mathrm{tg}\frac{1}{2}\left(-x_l-\frac{qd}{2}\right)-\left(1+\sqrt{1-c_-^2}\right)}\right|\right]\right\},\end{aligned} \tag{11}$$

where $x_l=k_l d$. When the electrons are completely filled the l-miniband, in the formula (11) $x_l=\pi$.

In case of $c_\pm^2>1$ we find

$$\begin{aligned}\operatorname{Re}P_{lm}(q,\omega)&=+\frac{1}{2\pi^2 ad\Delta\sin\frac{qd}{2}}\\
&\left\{\frac{1}{\sqrt{c_+^2-1}}\left[\mathrm{arctg}\frac{c_+\mathrm{tg}\left(x_l+\frac{qd}{2}\right)-1}{\sqrt{c_+^2-1}}+\right.\right.\\
&\left.\mathrm{arctg}\frac{c_+\mathrm{tg}\left(x_l-\frac{qd}{2}\right)+1}{\sqrt{c_+^2-1}}\right]-\\
&-\frac{1}{\sqrt{c_-^2-1}}\left[\mathrm{arctg}\frac{c_-\mathrm{tg}\left(x_l+\frac{qd}{2}\right)-1}{\sqrt{c_-^2-1}}+\right.\\
&\left.\left.+\mathrm{arctg}\frac{c_-\mathrm{tg}\left(x_l-\frac{qd}{2}\right)+1}{\sqrt{c_-^2-1}}\right]\right\}.\end{aligned} \tag{12}$$

If we restrict our consideration only the intraband transitions ($m=0$, $\Omega_\pm=0$, $c_+=c_-=c=\hbar\omega\Big/2\Delta\sin\frac{qd}{2}$), the formulas (11) and (12) is simplified.

Transition in the formulas (11) and (12) towards to the nanotube without superlattice is performed according to the rule

$$d\to 0,\ \Delta\to\infty,\ d^2\Delta\to\hbar^2\Big/m_*. \tag{13}$$

In this case, the spectrum (3) becomes (1) and formula (11) takes the form

$$\begin{aligned}\operatorname{Re}P_{lm}(q,\omega)&=-\frac{m_*}{2\pi^2\hbar^2 qa}\times\\
&\times\left[\ln\left|\frac{\omega-(\Omega_++q\upsilon_l+\omega_q)}{\omega-(\Omega_+-q\upsilon_l+\omega_q)}\right|-\right.\\
&\left.-\ln\left|\frac{\omega-(\Omega_-+q\upsilon_l-\omega_q)}{\omega-(\Omega_--q\upsilon_l-\omega_q)}\right|\right],\end{aligned} \tag{14}$$

where

$$\upsilon_l = \sqrt{\frac{2}{m_*}}\sqrt{\mu_0 - \varepsilon_l}$$

-maximal velocity of the electrons in the l-th subzone without superlattice, $\omega_q = \hbar q^2 / 2m_*$.

In the absence of interband transitions ($m = 0$) from the formula (5) we obtain the contribution of the l-miniband into the imaginary part of the polarization operator:

$$\operatorname{Im} P_{l0}(q,\omega) = -\frac{1}{4\pi a d\Delta\left|\sin\frac{qd}{2}\right|\sqrt{1-c^2}}, \tag{15}$$

where
$$q < 2k_l,\ 0 < \omega < 2\frac{\Delta}{\hbar}\sin\frac{qd}{2}\sin\left(x_l + \frac{qd}{2}\right).$$

If $q > 2k_l$, the function $\operatorname{Im} P_{l0}$ is still equal to (15), however $\omega_- < \omega < \omega_+$, where

$$\omega_\pm = 2\frac{\Delta}{\hbar}\sin\frac{qd}{2}\sin\left(\pm x_l + \frac{qd}{2}\right). \tag{16}$$

Fig. 1 shows graphs of functions (15) in these cases.

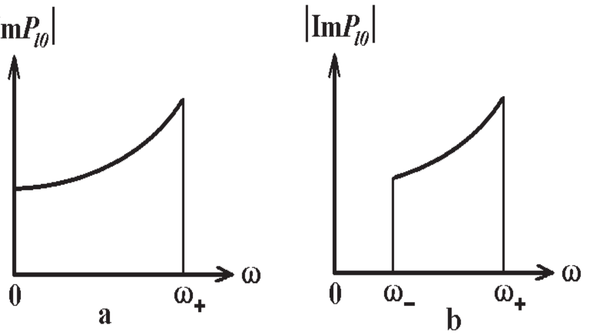

Fig. 1. The dependence of the imaginary part of polarization operator (15) as the functions of the frequency at $q < 2k_l$ (a), $q > 2k_l$ (b).

The values of the jump in the points $\omega_\pm$ are

$$\frac{1}{4\pi a d\Delta\left|\sin\frac{qd}{2}\cos\left(\pm x_l + \frac{qd}{2}\right)\right|}.$$

Taking into account the interband transitions ($m \neq 0$) instead of formula (15) in the vicinity of the frequencies $\Omega_\pm$ we get

$$\operatorname{Im} P_{lm}^{\pm}(q,\omega) = -\frac{1}{4\pi a d\Delta\left|\sin\frac{qd}{2}\right|\sqrt{1-c_\pm^2}}, \tag{17}$$

as in the formulas (16) terms $\Omega_\pm$ appear.

In the absence of spatial dispersion from the formula (5) at any temperature we obtain

$$\operatorname{Im} P_m(\omega) = \frac{\pi}{\hbar}\sum_l n_l\left[\delta(\omega - \Omega_-) - \delta(\omega - \Omega_+)\right], \tag{18}$$

where n_l – the surface density of electrons in the l-th miniband. In this case, the imaginary part of the polarization operator has sharp jump at frequencies of direct electron transitions between minibands.

Transparency windows

From formula (4) it is seen that for a obtaining of transparency windows for plasma waves in a degenerate electron gas on the surface of the nanotubes it is sufficient to consider the regions on a plane $q - \omega$, in which $\operatorname{Im} P = 0$. The same regions can be found from the laws of conservation of angular momentum projection and electron momentum projection on the axis of the tube, and from the law of conservation of energy under the electron-plasmon absorption. These conservation laws are:

$$\varepsilon_{lk} + \hbar\omega - \varepsilon_{(l+m)(k+q)} = 0. \tag{19}$$

From formula (5) we have seen that the left-hand side of equation (19) is the argument of the delta function, including into the imaginary part of the polarization operator. In addition, when an quantum electron transfer $(l,k) \to (l+m, k+q)$ is occurs, involving the absorption of a plasmon, the Pauli principle must be performed: $\varepsilon_{lk} < \mu_0 < \varepsilon_{(l+m)(k+q)}$. Consequently, after the substitution $k = \pm k_l$ in the equation (19), we obtain the boundaries of collisionless damping of plasma waves on the tube with a superlattice in a magnetic field:

$$\omega_\pm(q) = \Omega_\pm + 2\frac{\Delta}{\hbar}\sin\frac{qd}{2}\sin\left(\pm x_l + \frac{qd}{2}\right). \tag{20}$$

These equations contains the value $x_l = k_l d$ which determines the position of the Fermi level μ_0 in the l-th miniband. From the formula (8) it follows that under $x_l = 0$ Fermi energy is located at the “bottom” of the miniband ($\mu_0 = \varepsilon_l$). With the growth of the x_l Fermi energy and the electron density increases. When $x_l = \pi/2$ the level μ_0 is located in the center of the miniband ($\mu_0 = \varepsilon_l + \Delta$) and reaches her "ceiling" on the boundary of the Brillouin zone ($x_l = \pi,\ \mu_0 = \varepsilon_l + 2\Delta$). Thus, when $0 < x_l < \pi/2$ the Fermi level is located in the lower half of the miniband, while $\pi/2 < x_l < \pi$ – at the top.

When $q \to 0$, the difference $\omega_+ - \omega_-$ in the vicinity of each frequency $\Omega_\pm$ decreases, the Landau damping region is narrowed in accordance with the behavior of the polarization operator (18) in the absence of spatial dispersion. This narrowing is occurs at the boundary of the Brillouin zone where the second term on the right-hand side of (20) is equal to

$$\omega_\pm - \Omega_\pm = 2\frac{\Delta}{\hbar}\cos x_l . \tag{21}$$

The shape and dimensions of the regions of Landau damping in the vicinity of the frequencies $\Omega_\pm$ are determined by the position of the Fermi level in the miniband. When μ_0 increases from the "bottom" of the l-th miniband to its "ceiling" the expression (21) in the vicinity of the frequencies $\Omega_\pm$ decreases from $2\Delta/\hbar$ to $-2\Delta/\hbar$.

Figure 2 schematically shows Landau damping region between the curves (20) for various locations of the Fermi energy in the miniband in the vicinity of the frequency Ω_+. Outside these regions until the curves

$$\omega_{\min} = \Omega_+ - 2\frac{\Delta}{\hbar}\sin\frac{qd}{2},\quad \omega_{\max} = \Omega_+ + 2\frac{\Delta}{\hbar}\sin\frac{qd}{2} \tag{22}$$

located transparency window for plasma waves. The curves of (22) – solution of the equation $|c_+| = 1$. When $\hbar\Omega_+ < 2\Delta$, the graph of the curve $\omega_{\min}(q)$ (22) intersects the axis q at the point

$$q_0 = \frac{2}{d}\arcsin\frac{\hbar\Omega_+}{2\Delta}.$$

This point tends to the boundary of the Brillouin zone, when $\hbar\Omega_+ \to 2\Delta$. If $\hbar\Omega_+$ greater than the width of the miniband 2Δ, there is no intersection, i.e. $\omega_-(q) > 0$ located in the Brillouin zone.

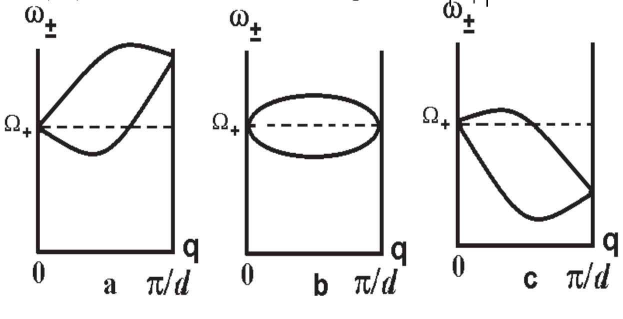

Fig. 2. Areas of Landau damping between the curves (20) at $\cos x_l > 0$ (a), $\cos x_l = 0$ (b) and $\cos x_l < 0$ (c).

The areas of Landau damping in the vicinity of the frequency Ω_- are similar to those shown in Fig. 2. Note, that when $\eta > 1/2$ the boundaries of the miniband are satisfy of inequalities $\varepsilon_{-1} < \varepsilon_0 < \varepsilon_{-2} < \ldots$ In this case, the frequency of the direct transition of electrons $-1 \to -2$ with $m = -1$ is equal $\Omega_+ = \varepsilon_0(3 - 2\eta)/\hbar$. In the vicinity of this frequency there exists a branch of the plasmon spectrum with negative helicity.

In the absence of interband transitions ($\Omega_\pm = 0$) Landau damping regions are bounded by the curve (20) and the axis q .

In formulas (20) perform the limit (13) towards to the nanotube without superlattice. We take into account (8) and

$$\sin x_l = \frac{1}{\Delta}\left[(\mu_0 - \varepsilon_l)(\varepsilon_l + 2\Delta - \mu_0)\right]^{1/2}.$$

Since $qd \ll 1$, from the formulas (20), taking into account the terms of the order q^2 we find

$$\omega_\pm = \Omega_\pm \pm \frac{1}{\hbar} qd\left[(\mu_0 - \varepsilon_l)(\varepsilon_l + 2\Delta - \mu_0)\right]^{1/2} + \frac{1}{2\hbar} q^2 d^2 (\varepsilon_l + \Delta - \mu_0).$$

Passing here to the limit (13), we obtain a parabola

$$\omega_\pm = \Omega_\pm \pm q\upsilon_l \pm \omega_q ,$$

appearing in the formula (14). The maximum speed of the electrons υ_l in the l-th miniband plays the role of the Fermi velocity υ_F of electrons in three-dimensional and two-dimensional electron gas.

The condition of resonant absorption of plasma waves on the tube with a superlattice when $m = 0$ has the form

$$\omega = 2\frac{\Delta}{\hbar}\sin\frac{qd}{2}\sin\left(k_l + \frac{q}{2}\right)d . \tag{23}$$

In the extreme case $qd \ll 1,\ q \ll k_l,\ k_l d < 1$, it takes the usual form in the theory of waves: $\omega/q = \upsilon_l$ – the phase velocity of the wave, propagating along the tube is equal to the longitudinal velocity of the electrons.

Conclusions

Study of propagation of plasma waves along the tube are very topical problem because it allows to determine the waveguide characteristics of the tube. In addition, it is possible to obtain additional information about the dynamic characteristics of the conduction electrons on the curved surface. The presence of an additional parameter – the curvature of the structure – enriches the picture of wave phenomena, increasing the number of ways to control the properties of the system. In particular, the rotational quantum contains the characteristic of circular motion of electrons on the tube – transverse effective mass. It may differ from the longitudinal mass. Superlattice adds new features to the picture of wave propagation. It is associated with additional parameters – the period and amplitude of the modulating potential. Characteristics of the tube – form and sizes of windows transparency of waves and their spectrum and damping – are sensitive to these parameters. This allows their to determine, by analyzing the properties of waves.

The paper used a simple model spectrum of electrons, simulating the superlattice on the tube. This allowed within the model adopted in the random phase approximation to obtain an exact expression for the polarization operator of the electron gas. As a result, the shape and size of windows transparency for plasma waves were determined in the entire Brillouin zone. They were obtained by analysis of the imaginary part of the polarization operator and with the help of conservation laws. The results can be used in the study of plasma waves in semiconductor superlattices on a base of $\mathrm{Al}_x\mathrm{Ga}_{1-x}\mathrm{As}/\mathrm{GaAs}$, $\mathrm{InGaAs}/\mathrm{GaAs}$, $\mathrm{InAs}/\mathrm{GaAs}$, $\mathrm{GeSi}/\mathrm{Si}$ and in carbon nanotubes in a metal conduction mode.

1. L.V. Keldysh. Fizika Tverd. Tela, 4, 2265 (1962).
2. L. Esaki, R. Tsu. IBM J. Res. Develop., 14, 61 (1970).
3. J.I. Alferov, Yu.V. Jilyaev, Yu.V. Shmartsev. Fizika Tehn. Poluprovod., 5, 196 (1971).
4. A.Ja. Shick. Fizika Tehn. Poluprovod., 8, 1841 (1974).
5. V.M. Gvozdikov. Fizika Tverd. Tela, 26, 2574 (1984).
6. V.M. Gvozdikov. Fizika Tverd. Tela, 28, 320 (1986).
7. A. Tselis, J. Quinn. Phys. Rev. B, 29, 2021 (1984).
8. A. Tselis, J. Quinn. Phys. Rev. B, 29, 3318 (1984).
9. A.P. Silin. Uspehi Fiz. Nauk, 147, 485 (1985).
10. M. Herman. Semiconductor Superlattices, Akademie-Verlag, Berlin (1986), 240 p.
11. L. Wendler, M.I. Kaganov. JETP letters, 44, 345 (1986).
12. V.N. Lutskiy, M.I. Kaganov, A.Ja. Shick. JETP, 92, 721 (1987).
13. M.I. Kaganov, V.N. Lutskiy, D.V. Posvyanskiy. Fizika Nizk. Temp., 15, 846 (1989).
14. W.-M. Que, G. Kirczenov. Phys. Rev. B, 36, 6596 (1987).
15. F.G. Bass, A.A. Bulgakov, A.P. Tetervov. High-frequency properties of the semiconductor superlattice, Nauka, Moscow (1989), 288 pp.
16. S. Iijima. Nature (London), 354, 56 (1991).
17. L.I. Magarill, A.V. Chaplik, M.V. Entin. Uspehi Fiz. Nauk, 175, 995 (2005).
18. N.A. Poklonskiy, E.F. Kislyakov, G.G. Fedoruk, S.A. Vyrko. Fizika Tverd. Tela, 42, 1911 (2000).
19. J. Lee, H. Kim, S.-J. Kahng, G. Kim, Y.-W. Son, J. Ihm, H. Kato, Z.W. Wang, T. Okazaki, H. Shinohara and Y. Kuk. Nature, 415, 1005 (2002).
20. H.-J. Shin, S. Clair, Y. Kim and M. Kawai. Nat. Nanotech., 4, 567 (2009).
21. Yu. I. Sezonov and Yu.V. Perepelkina. Russ. Journ. Phys. Chemistry B, 3, 247 (2009).
22. A.M. Ermolaev, G.I. Rashba, M.A. Solyanik. Fizika Nizk. Temp., 38, 653 (2012).
23. A.M. Ermolaev and G.I. Rashba. Solid State Commun., 192, 79 (2014).
24. I.O. Kulik. JETP letters, 11, 407 (1970).
25. O.P. Volosnikova, D.V. Zavyalov, S.V. Kruchkov. Proceedings of the XVII International Workshop “Radiational Solid state physics” 645, Sevastopol’, 7 (2007).
26. E.A. Pashitskiy, Yu.M. Malozovskiy, A.V. Semenov. Ukr. Fizich. Journ., 36, 889 (1991).
27. A.M. Ermolaev, G.I. Rashba, M.A. Solyanik. Fizika Nizk. Temp., 37, 1033 (2011).

Вісник ХНУ, № 1135, серія «Фізика», вип. 21, 2014. с. 16-20

УДК 537.867, 537.9, 538.945.
PACS: 74.78.Fk, 74.50.+r, 74.72.-h.

Transmittance of electromagnetic waves through finite-length layered superconductors in presence of external static magnetic field

T.N. Rokhmanova, Z.A. Maizelis

V.N. Karazin Kharkov National University,
Svobody Sq. 4, 61022, Kharkov. Ukraine
A.Ya. Usikov Institute for Radiophysics and Electronics,
National Academy of Sciences of Ukraine,
Proskura st. 12, 61085 Kharkov, Ukraine.

We study the transmission of electromagnetic waves in the presence of external DC magnetic field through a sample of layered superconductor of finite thickness. We show that the external DC magnetic field can be a useful tool to adjust the transmittance of the sample and to vary it over a wide range. Moreover, the right choice of the external DC field provides the total transparency of the sample for the wide range of frequencies.

Keywords: layered superconductors, magnetic field, transmittance.

Изучено прохождение электромагнитных волн в присутствии внешнего постоянного магнитного поля сквозь образец слоистого сверхпроводника конечной толщины. Показано, что внешнее постоянное магнитное поле может быть полезным инструментом для управления коэффициентом пропускания образца и варьирования его в широком диапазоне. Более того, правильный выбор внешнего магнитного поля может обеспечить полную прозрачность образца для широкого диапазона частот.

Ключевые слова: слоистый сверхпроводник, магнитное поле, коэффициент прохождения.

Досліджено проходження електромагнітних хвиль в присутності зовнішнього постійного магнітного поля крізь зразок шаруватого надпровідника скінченної товщини. Показано, що зовнішнє постійне магнітне поле може бути корисним інструментом для управління коефіцієнтом пропускання зразка і варіювання його в широкому діапазоні. Більш того, правильний вибір зовнішнього магнітного поля може забезпечити повну прозорість зразка у широкому діапазоні частот.

Ключові слова: шаруватий надпровідник, магнітне поле, коефіцієнт проходження.

Introduction

High-temperature layered superconductors are interesting materials from different perspectives [1]. The experimental studies for c-axis conductivity in $Bi_2Sr_2CaCu_2O_{8+\delta}$ (see, e.g., Refs. [2,3]) proved that layered superconductors can be represented as the periodic structures where thin superconducting layers (with thicknesses s of about 0.2 nm) are coupled through thicker dielectric layers (with thicknesses d of about 1.5 nm and a dielectric constant $\varepsilon \sim 16$) via the intrinsic Josephson effect. The anisotropy of the structure causes propagation of the specific electromagnetic excitations, the Josephson plasma waves (JPWs) (see, e.g., Refs. [1,4] and references therein). The frequencies of JPWs are in terahertz range, which makes layered superconductors promising in applications for THz devices (see, e.g., Ref. [5]).

The electrodynamic equations for layered superconductors are nonlinear. The nonlinearity originates from the nonlinear relation $J \propto \sin\varphi$ between the Josephson interlayer current J and the gauge-invariant interlayer phase difference φ of the order parameter. This can lead to a number of non-trivial nonlinear effects accompanying the propagation of JPWs, e.g., slowing down of light [6], self-focusing of terahertz pulses [6,7], excitation of nonlinear waveguide modes [8], as well as self-induced transparency of the slabs of layered superconductors and hysteretic jumps in the dependence of the slab transparency on the wave amplitude [9,10]. The noticeable change in the transparency of the cuprate superconductor when increasing the wave amplitude was recently observed in the experiment Ref. [11], where the excitation of Josephson plasma solitons led to effective decrease of the Josephson resonance frequency.

The external DC magnetic field can be used to control propagation the electromagnetic wave in different media. For example, in the works [12,13] the external DC magnetic field allows to adjust the parameters of the excited surface Josephson plasma waves propagating across the junctions in layered superconductors. In the present work, we concentrate our attention on the transmission of the waves of transverse magnetic (TM) polarization through a sample of layered superconductor in the presence of the external DC magnetic field. We show that the DC magnetic field can be a useful tool to control the transmissivity of the sample of layered superconductor.

Geometry of the problem

We study the transmission of the electromagnetic waves through a sample of layered superconductor of finite thickness D (see Fig. (1)). The coordinate system is chosen in such a way that the crystallographic **ab**-plane of the layered superconductor coincides with the xy-plane, and the **c**-axis is along the z-axis.

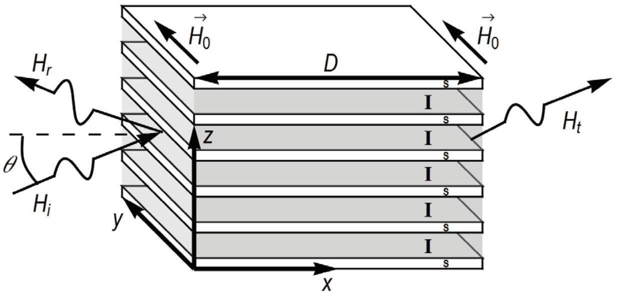

Fig.1. Schematic geometry for the reflection and transmission of waves through the sample of layered superconductor. Here S and I stand for superconducting and insulator layers, respectively, D is the thickness of the sample. The sample is infinite along y and z directions.

The waves are irradiated at an angle θ in xz-plane and have TM-polarization:

$$\vec{E} = \{E_x, 0, E_z\}, \vec{H} = \{0, H_y, 0\}. \qquad (1)$$

The external DC magnetic field $\vec{H}_0$ is directed along y-axis in the vacuum regions. We study the relatively small magnetic fields when Josephson vortices do not wholly penetrate inside of the sample.

Fields in the vacuum regions

The electromagnetic field in the vacuum regions to the right and to the left from the sample (see Fig. (1)) is superposition of the DC magnetic field and the field of the incident, reflected and transmitted waves. Using Maxwell equations one can derive following tangential components of the incident and reflected fields in the left region:

$$\begin{aligned} H_y^{\text{left}} &= H_i e^{i(k_x x + k_z z - \omega t)} + H_r e^{i(-k_x x + k_z z - \omega t)}, \\ E_z^{\text{left}} &= -\frac{k_x}{k}\left(H_i e^{i(k_x x + k_z z - \omega t)} - H_r e^{i(-k_x x + k_z z - \omega t)} \right), \end{aligned} \qquad (2)$$

where H_i and H_r are amplitudes of incident and reflected waves, respectively, $k_x = k\cos\theta$, $k_z = k\sin\theta$ are components of the wave vector, $k = \omega / c$ is its module, θ is the incident angle, c is the speed of light.

The tangential components of the transmitted field in the left region are:

$$\begin{aligned} H_y^{\text{right}} &= H_t e^{i(k_x(x-D) + k_z z - \omega t)}, \\ E_z^{\text{right}} &= -\frac{k_x}{k} H_t e^{i(k_x(x-D) + k_z z - \omega t)}, \end{aligned} \qquad (3)$$

where D is the thickness of the sample (see Fig. (1)), H_t is the amplitude of transmitted wave.

The field in the layered superconductor

The electromagnetic field in the layered superconductor is defined by the distribution $\varphi(\vec{r}, t)$ of interlayer gauge-invariant phase difference of the order parameter. This phase difference is governed by a set of coupled sine-Gordon equations [1, 14-18]. In the continual limit and in the main order with respect to the small parameter λ_{ab} / λ_c (for $\mathrm{Bi_2Sr_2CaCu_2O_{8+\delta}}$ λ_{ab} / λ_c is about 1/200), the coupled sine-Gordon equations reduce to the following equation:

$$\sin\varphi + \frac{1}{\omega_J^2}\frac{\partial^2\varphi}{\partial t^2} - \lambda_c^2 \frac{\partial^2\varphi}{\partial x^2} = 0. \qquad (4)$$

Here λ_{ab} and $\lambda_c = c / \omega_J \varepsilon^{1/2}$ are the London penetration depths across and along the layers, respectively, $\omega_J = (8\pi e d J_c / \hbar\varepsilon)^{1/2}$ is the Josephson plasma frequency, J_c is the maximal Josephson current density, and e is the elementary charge, d and ε are the thickness and dielectric conductivity of insulator layers, respectively. We do not take into account the relaxation terms since they are small at low temperatures and do not play an essential role in the phenomena considered here.

The gauge-invariant phase difference of the order parameter $\varphi(\vec{r}, t)$ defines components of the field in the layered superconductor (see e.g., Ref. [1]):

$$\begin{aligned} E_z^s &= \mathcal{H}_0 \frac{1}{\omega_J \sqrt{\varepsilon}} \frac{\partial\varphi}{\partial t}, \\ \frac{\partial H_y^s}{\partial x} &= \frac{\mathcal{H}_0}{\lambda_c}\left[\sin\varphi + \frac{1}{\omega_J^2}\frac{\partial^2\varphi}{\partial t^2} \right]. \end{aligned} \qquad (5)$$

The component E_z of the electric field causes the breakdown of electro-neutrality of the superconducting layers and results in an additional, so-called capacitive, interlayer coupling. In our case $k_z \sim k_x \sim k$, when incident angle is not close to $\pi / 2$, and capacitive coupling can be safely neglected because of the smallness of the parameter $\alpha = R_D^2 \varepsilon / sd$. Here R_D is the Debye length for a charge in a superconductor.

Penetration of external DC magnetic field into the sample

At first we describe how the external DC magnetic field penetrates into the sample of layered superconductor. The DC field exponentially decreases inside the sample. Here we assume that the sample is sufficiently large, $D \gg \lambda_c$, then we neglect interaction between ``tails'' of the field from the right and left boundaries. Using Eq. (4) we can derive expressions for the phase difference in the vicinity of the left and right boundaries:

$$\begin{aligned} \varphi_0^{left}(\xi) &= -4\arctan(e^{-\xi-\xi_0}), \\ \varphi_0^{rigth}(\xi) &= 4\arctan[e^{\xi-(\delta-\xi_0)}], \end{aligned} \tag{6}$$

where we introduce dimensionless coordinate $\xi = x/\lambda_c$ and normalized thickness of the sample $\delta = D/\lambda_c$. The constant ξ_0 is determined by the magnitude H_0 of external DC field:

$$\xi_0 = \operatorname{arccosh}\frac{1}{h_0}, \quad h_0 = H_0 \frac{\pi d \lambda_c}{\Phi_0}, \tag{7}$$

where $\Phi_0 = \pi c \hbar / e$ is the magnetic flux quantum. The field h_0 is normalized in such a way that Josephson vortices penetrate the superconductor when $h_0 > 1$. So, in this work we study relatively small fields $0 < h_0 < 1$, and the DC field exponentially decreases into the sample at a character distance much less than the thickness of the sample D.

Penetration of electromagnetic field of the wave into the sample

Now we describe the distribution of the fields when the incident electromagnetic wave is penetrating into the sample in the presence of external DC magnetic field. We consider the amplitude of incident wave to be much smaller than the amplitude of the DC magnetic field. In this case the gauge-invariant phase difference can be presented as a sum of three components:

$$\varphi(\xi, z, t) = \varphi_0^{left}(\xi) + \varphi_0^{right}(\xi) + \varphi_v(\xi, z, t), \tag{8}$$

where first two terms are given by the equations (6). The last term is the small addition, which oscillates with the frequency of the incident wave.

We expand Eq. (4) over a small parameter φ_v and seek it in the form:

$$\varphi_v(\xi, z, t) = a(\xi) e^{i(k_z z - \omega t)}. \tag{9}$$

Then Eq. (4) reduces to:

$$\begin{aligned} &\left[\frac{2}{\cosh^2(\xi+\xi_0)} + \frac{2}{\cosh^2(\delta+\xi_0-\xi)} + \tilde{\Omega}^2\right] a(\xi) \\ &= -\frac{\partial^2 a(\xi)}{\partial \xi^2}, \end{aligned} \tag{10}$$

where Ω is the normalized frequency:

$$\Omega = \frac{\omega}{\omega_J}, \qquad \tilde{\Omega} = \sqrt{\Omega^2 - 1}. \tag{11}$$

It should be emphasized that the first and second summands in the square brackets in Eq. (10) are independent from each other and essential only in the vicinity of the left and right boundary, respectively. Then the solution of the Eq. (10) can be found analytically:

$$\begin{aligned} a(\xi) &= C_1 e^{i\tilde{\Omega}\xi}[p^2 a_1(\xi) + a_2(\xi) - p\Omega] \\ &+ C_2 e^{-i\tilde{\Omega}\xi}[a_1(\xi) + p^2 a_2(\xi) + p\Omega], \end{aligned} \tag{12}$$

where

$$\begin{aligned} a_1(\xi) &= \tanh(\xi_0 + \xi) - 1, \\ a_2(\xi) &= \tanh(\xi_0 + \delta - \xi) - 1, \\ p &= \frac{1 + i\tilde{\Omega}}{\Omega}. \end{aligned} \tag{13}$$

Using equations (5) and (8), we can find the field in the layered superconductor. The tangential variable components of the field, normalized by the typical field $\Phi_0 / \pi d \lambda_c$, i.e. in the same way as in Eq. (7), are:

$$\begin{aligned} H_y \frac{\pi d \lambda_c}{\Phi_0} &= h_y = \frac{1}{2} a'(\xi) e^{i(k_z z - \omega t)}, \\ E_z \frac{\pi d \lambda_c}{\Phi_0} &= e_z = -\frac{i\Omega}{2\sqrt{\varepsilon}} a(\xi) e^{i(k_z z - \omega t)}. \end{aligned} \tag{14}$$

The transmission coefficient

Matching tangential components of the field in vacuum regions (2) and (3) with the field inside of the sample (14), we can find the unknown constants C_1 and C_2 in Eq. (12). Then we derive the transmission coefficient:

$$\begin{aligned} T &= \frac{|h_t|^2}{|h_i|^2} = \\ &\left(1 + \sin^2(\tilde{\Omega}\delta - \phi)\{[\frac{1}{4\Theta} + (\frac{h_0^4 \tilde{h}_0^2}{\Omega^4 \tilde{\Omega}^2} + 1)\Theta]^2 - 1\}\right)^{-1}, \end{aligned} \tag{15}$$

where

$$\begin{aligned} \tilde{h}_0 &= \sqrt{1 - h_0^2}, \quad \Theta = \frac{\Omega \tilde{\Omega} \sqrt{\varepsilon}}{2(\tilde{h}_0^2 + \tilde{\Omega}^2)} \cos\theta, \\ \phi &= \frac{\pi}{2} - \arctan\left(\frac{1 - \tilde{\Omega}^2}{2\tilde{\Omega}} + \frac{\Omega^4 \tilde{h}_0}{2\tilde{\Omega} h_0^2} P\right), \\ P &= \left[\frac{\Omega^2 \varepsilon \cos^2\theta}{\Omega^2 + (\tilde{h}_0^2 - \Omega^2)\varepsilon \cos^2\theta} - \frac{\tilde{h}_0 + \tilde{\Omega}^2}{\tilde{h}_0 + 1}\right]^{-1}. \end{aligned} \tag{16}$$

As was mentioned, the DC field h_0 varies from 0 to 1. One can reduce the equation (15) for these two cases. When there is no external field, $h_0 = 0$, we can simplify the equation (15) to the following form:

$$\begin{aligned} T(h_0 = 0) &= \left[1+\sin^2(\tilde{\Omega}\delta)\left(\frac{1}{4\Theta_0}-\Theta_0\right)^2\right]^{-1}, \\ \Theta_0 &= \frac{\tilde{\Omega}}{\Omega}\frac{\sqrt{\varepsilon}}{2}\cos\theta, \end{aligned} \tag{17}$$

When $\cos\theta = \Omega/(\tilde{\Omega}\sqrt{\varepsilon})$, the multiplier of sine is equal to zero and the full transmission occurs regardless the thickness of the sample. Note, that in the absence of DC field the phase ϕ in argument of the sine, Eq. (16), is either zero or π, $\sin\phi_0 = 0$. The deviation of phase ϕ from this value is the main effect from applying DC magnetic field.

If the value of the DC magnetic field is almost critical, $h_0 = 1$, the transmittance takes the form:

$$\begin{aligned} T(h_0 = 1) &= \left[1+\sin^2(\tilde{\Omega}\delta-\phi_1)\left(\frac{1}{4\Theta_1}-\Theta_1\right)^2\right]^{-1}, \\ \phi_1 &= 2\arctan\tilde{\Omega}, \quad \Theta_1 = \frac{\Omega}{\tilde{\Omega}}\frac{\sqrt{\varepsilon}}{2}\cos\theta, \end{aligned} \tag{18}$$

When $\cos\theta = \tilde{\Omega}/(\Omega\sqrt{\varepsilon})$, the transmittance is equal to 1. Thus, we see that for $h_0 = 0$ one can attain full transparency of the sample by choosing the angle for frequencies $\Omega > (1-\varepsilon^{-1})^{-1/2}$, while for $h_0 = 1$ the full transparency can be achieved for any prescribed frequency $\Omega > 1$.

Analysis of results

The dependence of the transmission coefficient on the thickness δ in equation (15) is only via $\sin(\tilde{\Omega}\delta - \phi)$. When the sine multiplier is equal to zero, the sample is transparent. In the absence of external DC magnetic field (see Eq. (17)) the sample is fully transparent, when the thickness is the integer number of the half-wavelengths,

$$\delta = \pi k/\tilde{\Omega}, \quad k = 1, 2... \tag{19}$$

If we turn on the DC field (see Eq. (15) or (18)), the sine acquires a new DC depending term ϕ in the argument. The DC magnetic field shifts the maximum only, while the periodicity of the function $T(\delta)$ remains the same. This shift is shown in the Fig. 2 by the arrow.

The variation of transmittance can be significantly increased by changing the DC field. To demonstrate this, we plot Fig. 3. The upper and lower curves represent the

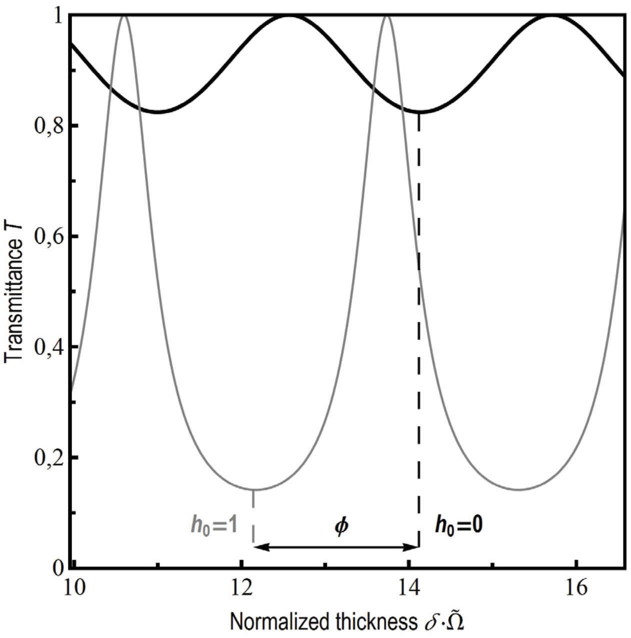

Fig. 2. Transmittance T versus normalized thickness δ ($\delta = D/\lambda_c$) in the absence of DC magnetic filed (thick black curve, h_0=0) and in the field h_0=1 (thin gray curve). The arrow shows shift of minima with applying of the DC magnetic field. Other parameters: Ω=1.2, $\theta = \pi/4$, $\lambda_c = 4\cdot10^{-3}$ cm, $\lambda_{ab} = 2000$ Å, $\omega_J/2\pi = 0.3$ THz, ε=16.

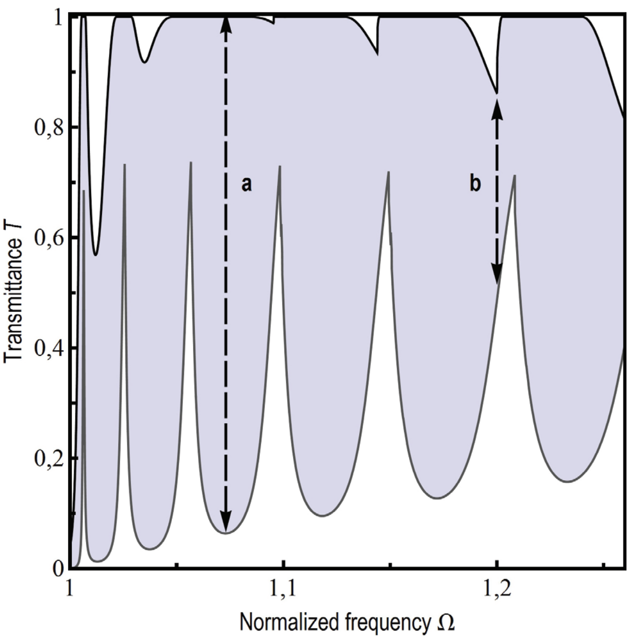

Fig. 3. Transmission T versus normalized frequency Ω. The gray region shows the variation of transmittance when changing the external DC magnetic field, the upper black and bottom gray curves show the maximum and minimum possible transmittance, respectively. Other parameters: $\theta = \pi/4$, δ=30, $\lambda_c = 4\cdot10^{-3}$ cm, $\lambda_{ab} = 2000$ Å, $\omega_J/2\pi = 0.3$ THz, ε=16.

transmittance maximized and minimized over the DC field amplitude as a function of frequency Ω. The gray intermediate region between the upper and lower curves shows the range of transmittance variation.

As one can see from Fig. 3, the range of transmittance variation depends significantly on the choice of the frequency. For example, we can compare the ranges marked by the a and b dashed lines (see Fig. 3). For the frequency corresponding to the line a, one can vary the transmittance nearly from zero to one, while the range is much smaller for the line b and one even cannot attain the full transmission. So the choice of the wave frequency defines the range of transmittance variation. In order to obtain the wide range, one should use relatively small frequencies, but not very close to the Josephson plasma frequency ω_j (see Fig. 3).

Conclusions

In this paper, we have studied theoretically the transmission of transverse magnetic waves through a finite sample of layered superconductor in the presence of external DC magnetic field. The dependence of the transmittance on the thickness of the sample is periodical. The DC field effectively changes the thickness and shifts the maxima of transmittance, but does not affect the periodicity. Also we show that the choice of the wave frequency defines the range of transmittance variation when changing the DC field. Thus, with the right choice of parameters the transmittance can be adjusted by the external DC magnetic field in a wide range.

1. S. Savel'ev, V.A. Yampol'skii, A.L. Rakhmanov, and F. Nori, Rep. Prog. Phys. 73, 026501 (2010).
2. R. Kleiner, F. Steinmeyer, G. Kunkel, and P. Müller, 68, 2394 (1992).
3. R. Kleiner and P. Müller, 49, 1327 (1994).
4. X. Hu and S.-Z. Lin, Supercond. Sci. Technol. 23, 053001 (2010).
5. L. Ozyuzer, A. E. Koshelev, C. Kurter, N. Gopalsami, Q. Li, M. Tachiki, K. Kadowaki, T. Yamamoto, H. Minami, H. Yamaguchi, T. Tachiki, K. E. Gray, W.-K. Kwok, U. Welp, Science, 318, 1291 (2007).
6. S. Savel'ev, A.L. Rakhmanov, V.A. Yampol'skii, and F. Nori, Nature Phys. 2, 521 (2006).
7. V.A. Yampol'skii, S. Savel'ev, A.L. Rakhmanov, and F. Nori, Phys. Rev. B 78, 024511 (2008).
8. S. Savel'ev, V.A. Yampol'skii, A.L. Rakhmanov, and F. Nori, Phys. Rev. B 75, 184503 (2007).
9. S.S. Apostolov, Z.A. Maizelis, M.A. Sorokina, V.A. Yampol'skii, and F. Nori, Phys. Rev. B 82, 144521 (2010).
10. T. N. Rokhmanova, S.S. Apostolov, Z.A. Maizelis, V.A. Yampol'skii, and F. Nori, Phys. Rev. B 88, 014506 (2013).
11. A. Dienst, E. Casandruc, D. Fausti, L. Zhang, M. Eckstein, M. Hoffmann, V. Khanna, N. Dean, M. Gensch, S. Winnerl, W. Seidel, S. Pyon, T. Takayama, H. Takagi and A. Cavalleri, Nature Mat. 12, 535 (2013).
12. V. A. Yampol'skii, D. R. Gulevich, Sergey Savel'ev, Phys. Rev. B. 78, 054502 (2008).
13. D. V. Kadygrob, V .A. Golick, V. A. Yampol'skii, T. M. Slipchenko, D. R. Gulevich, and Sergey Savel'ev, Phys. Rev. B. 80, 184512 (2009).
14. S. Sakai, P. Bodin, and N.F. Pedersen, J. Appl. Phys. 73, 2411 (1993).
15. S.N. Artemenko and S.V. Remizov, JETP Lett. 66, 811 (1997).
16. S.N. Artemenko and S.V. Remizov, Physica C 362, 200 (2001).
17. Ch. Helm, J. Keller, Ch. Peris, and A. Sergeev, Physica C 362, 43 (2001).
18. Ju.H. Kim and J. Pokharel, Physica C 384, 425 (2003).

Вісник ХНУ, № 1135, серія «Фізика», вип. 21, 2014. с. 21-24

УДК 538.945+537.312.62

Effect of transverse magnetic field on the excess conductivity of monodomain $YBa_2Cu_3O_{7-\delta}$ single crystals

K.A. Kotvitskaya[1,2], K.V. Tiutierieva[1], S.V. Savich[1], V.V.Sklyar[1], R.V. Vovk[1,2]

[1]Physics Department, V. Karazin Kharkiv National University,
Svobody Sq. 4, 61077 Kharkiv, Ukraine
[2]Ukrainian State Academy of Railway Transport,
Feyerbaha Sq. 7, 61050 Kharkiv, Ukraine

In present work the influence of a transverse on the temperature dependence of the excess conductivity in the temperature interval of the transition to the superconducting state in untwinned $YBa_2Cu_3O_{7-\delta}$ single crystals with optimal oxygen content are investigated. Causes of low-temperature “tails” (paracoherent transitions) in the resistive transitions in superconducting state are analyzed in the framework of the implementation of the various regimes of the phase state of vortex matter.

Keywords: excess conductivity, $YBa_2Cu_3O_{7-\delta}$ single crystals, oxygen deficiency, pinning, 2D-3D crossover, intrinsic pinning.

В роботі досліджено вплив поперечного магнітного поля на температурні залежності надлишкової провідності в області переходів у надпровідний стан роздвійникованих монокристалів $YBa_2Cu_3O_{7-\delta}$ з оптимальним вмістом кисню. Причини виникнення низькотемпературних «хвостів» (паракогерентних переходів) на резистивних переходах в надпровідний стан аналізуються в рамках моделі реалізації різних режимів фазового стану вихрової матерії.

Ключові слова: надлишкова провідність, монокристали $YBa_2Cu_3O_{7-\delta}$, дефіцит кисню, пінінг, 2D-3D кросовер, власний пінінг.

В работе исследовано влияние поперечного магнитного поля на температурные зависимости избыточной проводимости в области переходов в сверхпроводящее состояние раздвойникованных монокристаллов $YBa_2Cu_3O_{7-\delta}$ с оптимальным содержанием кислорода. Причины появления низкотемпературных «хвостов» (паракогерентных переходов) на резистивных переходах в сверхпроводящее состояние анализируются в рамках модели реализации различных режимов фазового состояния вихревой материи.

Ключевые слова: избыточная проводимость, монокристаллы $YBa_2Cu_3O_{7-\delta}$, дефицит кислорода, пиннинг, 2D-3D кроссовер, собственный пиннинг.

Creation of new functional materials with high current-carrying capacity continues to remain one of actual applied and fundamental problems of physics of high-temperature superconductivity (HTSC). The major role thus is played optimization of defective ensemble [1]. A small coherence length ξ [2] and a large penetration depth λ result in effective pinning in HTSC on small-scale defects, including oxygen vacancies [3] and the introduction of impurities [4]. The impact of such defects on the phase state of the vortex matter is often difficult to explain due to the presence in the HTSC intergranural boundaries, twin boundaries (TB), clusters of inclusions and other defects which are powerful pinning centers. The presence «intrinsic» pinning due to the layered structure of HTSC compounds is also significantly affected [3].

In the present study we investigate the magnetic conductivity in untwined $YBa_2Cu_3O_{7-\delta}$ single crystals under different values of magnetic field H in the ab-plane (H,ab). Using as samples untwined single crystals we eliminate the influence of intergranural boundaries and TB allowing the selected geometry of the experiment to control the changes of the contribution of intrinsic pinning. In this case, the measurement of the resistivity transitions to the superconducting state, allows the investigation of the impact of the point defects to the phase state and to the dynamics of vortex matter. This is achieved by analyzing the fluctuation to the conductivity that was observed in HTSC compounds at temperatures near to the critical temperature ($T\approx T_c$) [3-5].

The aim of this work is to study the effect of a constant magnetic field on the intrinsic pinning and the excess conductivity of single-domain single crystals of YBaCuO with optimal oxygen content.

Experimental methods

The $YBa_2Cu_3O_{7-\delta}$ single crystals were grown in a gold crucible with the solution-melting method, with the methodology described previously [3]. The $YBa_2Cu_3O_{7-\delta}$ oxygen saturating regime leads to the tetra-ortho structural transition that in its turn results to the crystal twinning in order to minimize its elastic energy. To obtain untwined samples, we used a special cell at 420° C and pressure 30-40 GPa, in accordance to the procedure [6]. To obtain homogeneous oxygen content, the crystal was annealed again in an oxygen flow at a temperature of 420°C for seven days.

To form electric contacts the standard four-contact scheme was used. In this, silver paste was applied onto the crystal surface and the connection of silver conductors (with diameter 0.05mm).Thereafter, they were annealed at a temperature of 200°C in an oxygen atmosphere for three hours. This methodology results in contacts with resistance than 1 Ohm and allows measurements with a current of 10 mA in the *ab*-plane. All the measurements were performed in a temperature drift mode using the method for two opposite directions of the transport current. This effectively eliminates the impact of the parasitic signal. A platinum thermoresistor was used to monitor the temperature, whereas the voltage was measured across the sample and the reference resistor with V2-38 nano-voltmeters. Data from the voltmeters interface is automatically transferred to computer. The critical temperature (Tc) was defined as the temperature corresponding to the main maximum in the $d\rho_{ab}(T)/dT$ dependence in the superconductive transition.

The magnetic field at 15 kOe was created by an electromagnet, which could vary the orientation of the field relative to the crystal. The accuracy of the field orientation relative to the sample was better than 0.2°. A sample was mounted in the measuring cell so that the vector field H was always perpendicular to the vector of the transport current ***j***.

For investigations of the resistive transitions in superconducting (SC) state we used the Kouvel- Fischer method [7]. This is based on the analysis of the quantity $\chi = \frac{-d(\ln\Delta\sigma)}{dT}$, where $\Delta\sigma = \sigma - \sigma_0$ is the excess conductivity, which arises in the conducting subsystem due to the fluctuation pairing of carriers at $T>T_c$ [8] and determined by the phase state of vortex matter at $T<T_c$ [4,5]. Here $\sigma=\rho-1$ is the experimentally measured value of conductivity, and $\sigma_0=\rho_0-1=(A+BT)-1$ is a term, determined by extrapolating the high-temperature linear segment up to the area of the SC transition. Assuming that $\Delta\sigma$ diverges as $\Delta\sigma\sim(T-T_c)-\beta$ at $T\approx T_c$, from the derivative $\chi = \frac{-d(\ln\Delta\sigma)}{dT}$ it follows that $\chi-1=\beta-1(T-T_c)$, where β is an indicator that depends on the dimension and the phase state of the fluctuation and vortex subsystems [4,5,8]. Thus, the identification of linear temperature dependence $\chi-1(T)$ at the same time allows the determination of important dimensional parameters and characteristic temperatures of dynamic phase transitions in the SC carrier's subsystem.

Results and discussion

Figure 1 shows the temperature dependences of resistivity in the basal ab-plane $\rho_{ab}(T)$, measured under H=0 (curve 1) and H = 3,2; 6,1; 9,3; 12,4; 15,05, respectively. As can be seen from the figure, the temperature is lowered from 300 K, $\rho_{ab}(T)$ decreases almost linearly up to a certain characteristic temperature $T^*\approx 180$ K. Below this temperature begins systematic deviation of experimental points down from the linear dependence, indicating that the appearance of excess conductivity $\Delta\sigma$, as discussed above. According to modern concepts such behavior depending $\rho_{ab}(T)$ at temperatures $T >> T_c$ conditioned by the manifestation of the so-called "pseudogap anomalies" (PG), which is discussed in more detail in [9].It should also be noted that the application of a magnetic field and change the magnetic field at temperatures $T> 1.15\ T_c$, within experimental error, have not effect on the behavior of the curves $\rho_{ab}(T)$, both leading to a significant broadening of the superconducting transition itself, in comparison with the sharp ($\Delta T_c\approx 0.3$ K) transition, observed at H = 0.

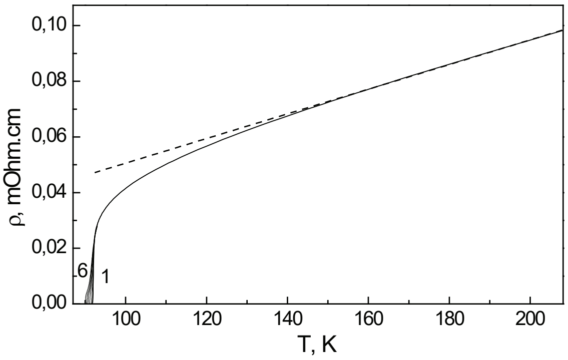

Fig. 1. Temperature dependences of resistivity in the basal ab-plane $\rho_{ab}(T)$ for the $YBa_2Cu_3O_{7-\delta}$ single crystal for H=0 (curve 1) and for H = 3,2; 6,1; 9,3; 12,4; 15,05 KOe (curves 2-6 respectively). The dotted lines in the figure shows a linear extrapolation of the plots in the low temperature region.

In this case, it is clear that on the tail of the superconducting transition is observed sharp "kink", which also appears in the form of sharp low-temperature peak in the temperature dependence of the derivative $d\rho_{ab}(T)/dT$ (Fig. 2).

As can be seen from Fig. 2, the peak is present for all values of H, while its height increases with increasing values of H. According to [3,4], the appearance of such features in the temperature dependences $\rho_{ab}(T)$ and $d\rho_{ab}(T)/dT$ shows the implementation in the first order phase transition corresponding to melting of the vortex lattice. Figure 3 shows the resistivity transitions to the SC state in coordinates $\left[\frac{-d(\ln\Delta\sigma)}{dT}\right]^{-1} - T$ In all curves in the

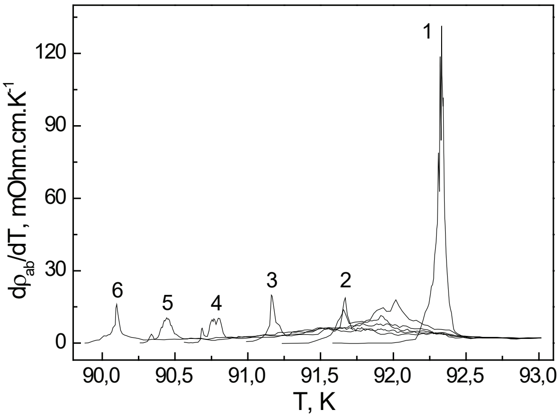

Fig. 2. Resistivity transitions to the superconducting state for the $YBa_2Cu_3O_{7-\delta}$ single crystal in $d\rho_{ab}/dT - T$ coordinates . The numbering of the curves is consistent to Fig. 1.

high-temperature area of the SC transition we observe a linear area with slope ≈0.5, which according [8] indicates the realization of a three-dimensional (3D) regime of fluctuation carriers' existence in the system. In this, the section corresponding to 3D regime is essentially unstable in the magnetic field, which is consistent with the results obtained by [3-5]. When increasing the temperature from Tc upwards, an increase of the absolute value of β occurs, this suggests the realization of a 3D-2D crossover in the system [3,4,8].

The application of magnetic field and the increase of the H, leads to a significant transformation of the form of the SC-transition occurs, which is expressed in the appearance of an additional low-temperature peak, so-called «para-coherent transition». At the same time, the shift of the transition to lower temperatures accompanied by a significant increase in simultaneous amplitude and width of the peak with increasing H. Similar behavior may be due to a decrease with an increase in the proportion H own intrinsic pinning, and thus increasing the role of bulk pinning. This, in turn, can contribute to the transition from the ordered phase in the phase grating of the vortex so-called "vortex" or "Bragg" glass due to the accommodation of a chaotic vortex pinning potential. This chaotic pinning potential violates the long-range order of vortex lattice, thereby suppressing the first –order phase transition and results to formation of glassy state of vortices. In the resistive transitions appear "tails", whose amplitude is less than the resistance of viscous flow ρff. These are probably due to a partial pinning of the vortex liquid. In our case, the role of this potential can play oxygen vacancies [9].

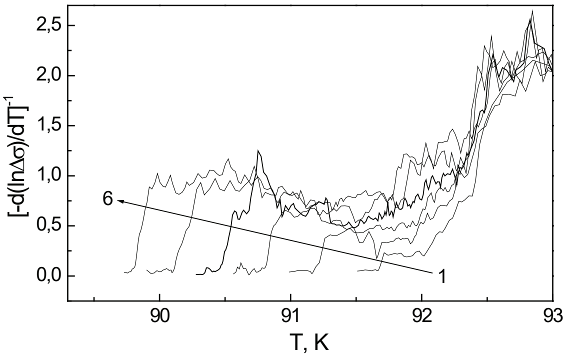

Fig. 3. Resistivity transitions to the superconducting state for the $YBa_2Cu_3O_{7-\delta}$ single crystal in $\left[\frac{-d(\ln\Delta\sigma)}{dT}\right]^{-1} - T$ coordinates. The numbering of the curves is consistent to Fig. 1. The dash lines correspond to the extrapolation of the areas corresponding to various 3D FC regimes.

Conclusions

In summary, the application of a constant magnetic field to $YBa_2Cu_3O_{7-\delta}$ single crystals leads to additional of the additional para-coherent transition in the excess conductivity temperature dependences in the basic *ab*-plane in the area of the resistive transition to the superconducting state.

The increase in the magnetic field leads to a simultaneous increase in the amplitude and width of the peak, which corresponds to this transition, and its displacement to lower temperatures. This may be due to a decrease with increasing H contribution of its own vortex pinning subsystem and the role of bulk pinning due to the presence in the structure of the experimental sample of oxygen vacancies. As a result, at temperatures below the critical T <T_c, the phase transition manifests dynamic vortex liquid form - vortex "Bragg" glass.

1. A.I. Chroneos, I.L. Goulatis and R.V. Vovk Atomic Scale Models for $RBa_2Cu_3O_{6.5}$ and $R_{1-x}Pr_xBa_2Cu_3O_{6.5}$ Compounds (R= Y and Lanthanides) // Acta Chim. Slov. – 2007. – Vol.54. – P. 179-184.
2. A.V. Bondarenko, A.A. Zavgorodniy, D.A. Lotnik, M.A. Obolenskii, R.V. Vovk Creep and depinning of vortices in nontwinned $YBa_2Cu_3O_{6.87}$ single crystal // Fizika Nizkikh Temperatur.- 2008.- Vol.34.- P. 645-652.
3. R.V. Vovk et. al Effect of small oxygen deficiency on the para-coherent transition and 2D-3D crossover in untwinned $YBa_2Cu_3O_{7-\delta}$ single crystals // Journal of Alloys and Compounds. – 2011. – Vol.509. – P.4553–4556.
4. А.А. Завгородний, Р.В. Вовк, М.А.Оболенский, А.В.Самойлов Магнитосопротивление и 2D-3D кроссовер в легированных алюминием монокристалах $YBa_2Cu_{3-z}Al_zO_{7-\delta}$ с системой однонаправленных двойниковых границ // ФНТ.- 2010. – Т.36, №1. - С.143-147.

5. R.M. Costa, I.C. Riegel, A.R. Jurelo, J.L.Jr. Pimentel Coherence transition in polycrystalline $Y_{0.95}Tb_{0.05}Ba_2Cu_3O_{7-\delta}$ superconductors // Journal of Magnetism and Magnetic Materials. - 2008. - Vol.320. –P. e493-e495.
6. J. Giapintzakis, D.M. Ginzberg, P.D. Han A method for obtaining single domain superconducting $YBa_2Cu_3O_{7-x}$ single crystals // J. Low Temp. Phys. -1989. -Vol.77, №1/2. - P.155-161.
7. J.S. Kouvel, M.E. Fischer Detailed Magnetic Behavior of Nickel Near its Curie Point // Phys. Rev. – 1964. -Vol.136. –P. A1626–A1632.
8. Л.Г. Асламазов, А.И. Ларкин Влияние флуктуаций на свойства сверхпроводников при температурах выше критической // ФТТ. - 1968. -Т.10, №4. -С.1104-1111.
9. Р.В. Вовк, М.А. Оболенский, А.А. Завгородний, А.В. Бондаренко, И.Л. Гулатис, Н.Н. Чеботаев Влияние перераспределения лабильного кислорода на псевдощелевое состояние в бездвойниковых монокристаллах $YBa_2Cu_3O_{7-x}$ // ФНТ. - 2007. - Т.33, №8. -С.931-934.

Вісник ХНУ, № 1135, серія «Фізика», вип. 21, 2014. с. 25-26

УДК 537.61; 538.955
PACS: 78.20.Ls, 75.10.Lp, 71.23.An

Constant of Verde of aluminium-rare-earth garnets

E.S. Orel

O.M. Beketov National University of Urban Economy in Kharkiv,
Ukraine, 61002, Kharkov, Revolyutsii street, 12

The model of local optical dipoles [1] for an explanation of the nature of dependence of a constant of Verde of aluminium-rare-earth granates from the magnetic moment of an ion of rare-earth element $m_B gJ$ (m_B-magneton of Bohr, g and J – the factor of Lande and the angular moment of a 4f-shells, accordingly) is considered. Research has shown that Faraday rotation in the aluminium-rare-earth garnets $R_3Al_5O_{12}$ (R=Tb, Dy, Ho, Er, Tm, Yb) [4] is caused, as well as electric polarizability RIG [3], the local magnetic fields created by 4f-shellss of rare-earth elements (type interaction «spin-another's an orbit») and operating, in essence, within nuclear radius of rare-earth elements.

Keywords: 4f-shellss, local optical dipoles, a constant of Verde, a magnetic susceptibility.

Рассмотрена модель локальных оптических диполей [1] для объяснения природы зависимости константы Верде алюмо-редкоземельных гранатов от магнитного момента иона редкоземельного элемента $m_B gJ$ ($m_В$ –магнетон Бора, g и J – фактор Ланде и угловой момент 4f-оболочки, соответственно). Исследование показало, что фарадеевское вращение в алюмо-редкоземельных гранатах $R_3Al_5O_{12}$ (R=Tb, Dy, Ho, Er, Tm, Yb) [4] обусловлено, как и электрическая поляризуемость RIG [3], локальными магнитными полями, создаваемыми 4f-оболочками редкоземельных элементов (взаимодействие типа «спин-чужая орбита») и действующими, по существу, в пределах атомного радиуса редкоземельных элементов.

Ключевые слова: 4f-оболочки, локальные оптические диполи, константа Верде, магнитная восприимчивость.

Розглянута модель локальних оптичних диполів [1] для пояснення природи залежності константи Верде алюмо-рідкоземельних гранатів від магнітного моменту іона рідкоземельного елементу $m_B gJ$ ($m_В$ -магнетон Бору, g і J - фактор Ланде і кутовий момент 4f-оболонки, відповідно). Дослідження показало, що фарадеєвське обертання в алюмо- рідкоземельних гранатах $R_3Al_5O_{12}$ (R=Tb, Dy, Ho, Er, Tm, Yb)[4] обумовлено, як і електрична поляризуємість RIG [3], локальними магнітними полями, що створюються 4f-оболонками рідкоземельних елементів (взаємодія типу «спін-чужа орбіта») і діючими, по суті, в межах атомного радіусу рідкоземельних елементів.

Ключові слова: 4f-оболонки, локальні оптичні диполі, константа Верде, магнітна сприйнятливість.

Introduction

Rare-earth elements (REE) are the fundamental constituent of many compounds used in construction materials of modern electronics, in particular in magnetooptics (MO) devices. In this connection there is of interest finding out of mechanisms of forming of MO of properties of REE.

In the real work we develop the model of local optical dipoles [1], used for explaining to of nature dependence of electric polarizability of rare-earth ferrits-garnets (RIG) [2] from the magnetic moment of ion of REE $m_B gJ$ (m_B - magneton of Bohr, g and J is a factor of Lande and angular moment of 4*f*- shells, accordingly) [3]. Research showed that a Faraday rotation is in the aluminium-rare-earth garnets $R_3Al_5O_{12}$ (R=Tb, Dy, Ho, Er, Tm, Yb) [4] it contingently, as well as electric polarizability of RIG [3], by the local magnetic fields created by the 4*f*- shellss of REE (type interaction «spin-another's an orbit») and operating, essentially, within the limits of atomic radius of REE.

Model and experiment

In our model (in fundamental part consilient with a model [3]) expression for the constant of Verde $V(\nu,T)$ at $H\to 0$, looks like :

$$V(\nu,T) = a(T)g(J+1)\times \times(b-gJ)\frac{\nu^2 E_{if}}{\left(E_{if}^2-\nu^2\right)^2}\,, \qquad (1)$$

where ν - energy of photon; E_{if} - energy of resonant optical transition; *T*- temperature; *a*(*T*) - function, proportional to magnetic receptivity and containing rate fixing constants different, as follows from an experiment, for Tb and Dy, from one side, and for Ho, Er, Tm and Yb, with other (Fig. 1.).

Taking into account the rate fixing constants of REE expression for the constant of Verde *V* (1) as a function of energy of photon of *E* looks like

$$V_R\left(E\right) = a_R\frac{E^2 E_{ifR}}{\left(E_{ifR}{}^2-E^2\right)^2}\,. \qquad (2)$$

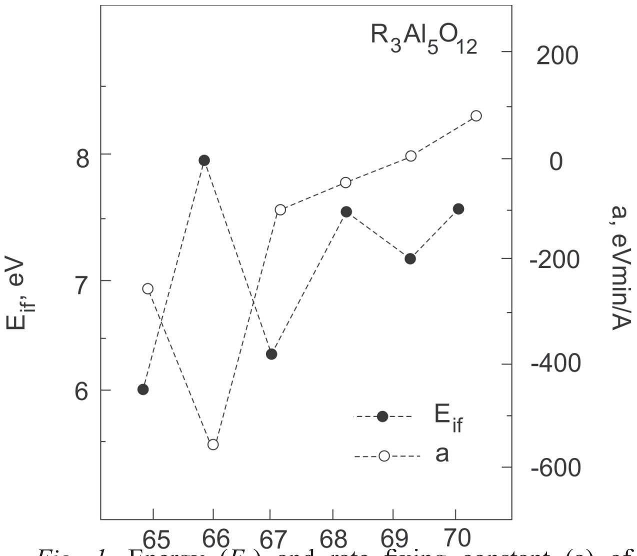

Fig. 1. Energy (E_{if}) and rate fixing constant (a) of resonant optical transition are in the aluminium-rare-earth garnets, got within the framework of the real model with the use of data [4].

On Fig. 2. dependence of constant of Verde is shown on energy of photon.

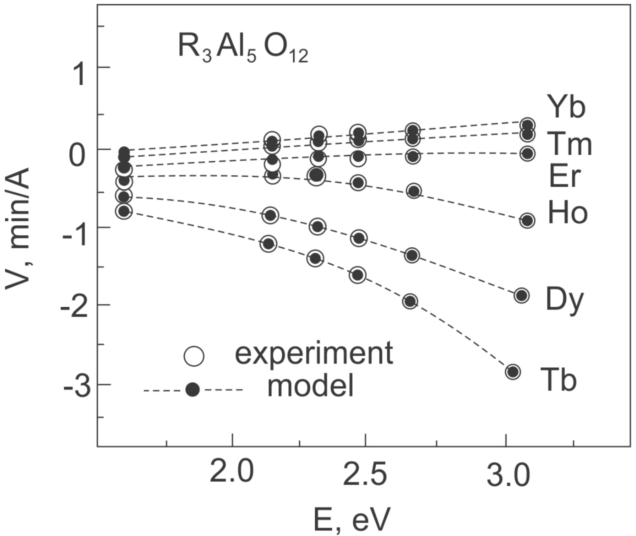

Fig. 2. Constant of Verde *V* of the aluminium-rare-earth garnets of $R_3Al_5O_{12}$, as a function of energy of photon of E; experimental values - from data [4], model is adjustment for the model developed in this work.

Constant of Verde, as function of atomic number of rare-earth element of Z got with the use of fitting parameters of b=7.6, $a(T)$=2.4 eVmin/A for Tb and Dy, and $a(T)$=0.6 eVmin /A for Ho, Er, Tm and Yb, at ν=3.06 eV and T=300 K:

$$V(3.06\ \text{eV}, 300K) =$$

$$= 2.4g(J+1)(7.6-gJ)\frac{3.06^2 E_{if}}{(E_{if}{}^2 - 3.06^2)^2} \qquad (3)$$

for Tb и Dy, and

$$V(3.06\ \text{eV},\ 300K) =$$

$$= 0.6g(J+1)(7.6-gJ)\frac{3.06^2 E_{if}}{(E_{if}{}^2 - 3.06^2)^2} \qquad (4)$$

for Ho, Er, Tm and Yb.

On Fig. 3. dependence of constant of Verde is presented on the atomic number of rare-earth element from which evidently, that a model provides adjustment of the experimentally looked after size of constant of Verde V rare-earth garnets [4].

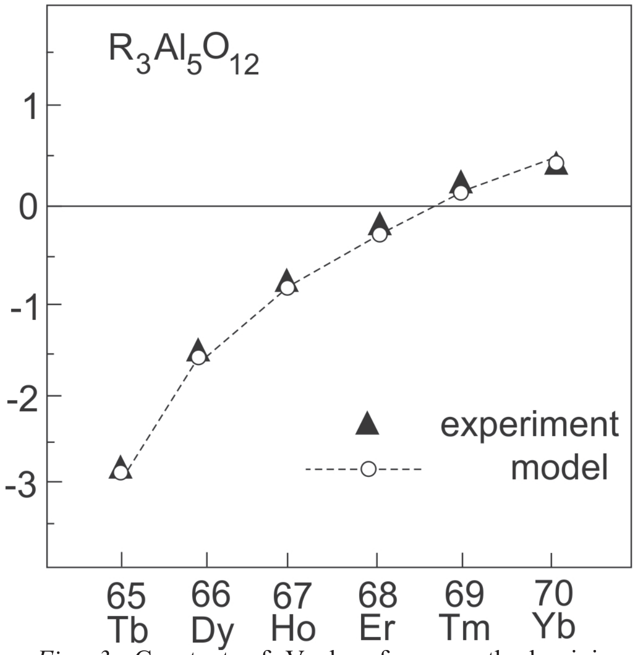

Fig. 3. Constant of Verde of rare-earth-aluminium garnets of $R_3Al_5O_{12}$, as function of atomic number of rare-earth element; model values are got in the this work, experimental - from data [4].

Conclusions

Research showed that a Faraday rotation is in the rare-earth grenades of $R_3Al_5O_{12}$ (R=Tb, Dy, Ho, Er, Tm, Yb) [4] it contingently, as well as electric polarizability of RIG [3], by the local magnetic fields created by the 4*f*- shells of rare-earth elements (type interaction «spin-another's an orbit») and operating, essentially, within the limits of atomic radius of rare-earth elements. Comparison of experimental data [4] with the model values (2-4) got in the real work allows to draw conclusion, that the use of model of local optical dipoles can profit at the study of magnetooptics properties of rare-earth garnets.

1. A. B. Beznosov and E. S. Orel. Fiz. Nizk. Temp., 27, 5, 508 (2001).
2. E. S. Orel. Visnyk KNU, 1076, series " Physics ", 19, 26 (2013).
3. A. B. Beznosov, A.I. Galuza, E. S. Orel. "New magnetic materials of microelectronics", MSU, Moscow, (2002), p.673.
4. Physical values. Edited by N.S. Grigoriev, E.Z. Meylihov. Energoatomizdat, Moscow, (1991), 1232 p.
5. A. B. Beznosov and E. S. Orel. Fiz. Nizk. Temp., 30, 9, 958 (2004).
6. A. B. Beznosov and E. S. Orel. Fiz. Nizk. Temp., 30, 10, 1053 (2004)

Вісник ХНУ, № 1135, серія «Фізика», вип. 21, 2014. с. 27-32

PACS 74.80.Fn
УДК 539.292

Elastic point contact spectroscopy of electron-phonon interaction in superconductive lead

A.V.Khotkevich[1,2], V.V.Khotkevych[3], O.S.Krasnyi[2]

[1] *B.I. Verkin Institute for Low Temperature Physics and Engineering*
[2] *V.N. Karazin National University*
[3] *Rutherford Appleton Laboratory, Harwell, UK*
khotkevich@ilt.kharkov.ua

A method for experimental determination of the spectral function of electron-phonon interaction (SF EPI) in superconductors with strong coupling has been developed. The method is based on analysis of non-linear current-voltage characteristics of point heterocontacts superconductor-normal metal. The nonlinearities arise in the elastic component of the current through the hetero-contact due to dependence on energy of the complex function of the energy gap in superconductor, and they have a similar nature as ones observed in superconducting tunnel contacts. For the purpose of present study the lead as a typical superconductor with strong EPI was chosen. In order to obtain the SE EPI the Eliashberg equation was solved numerically following the McMillan-Rowell method. Our solution is in good agreement with the results of elastic tunnel spectroscopy of superconductors as well as with the data provided by the inelastic point contact spectroscopy in the normal state.

Keywords: superconductivity, electron-phonon interaction, point-contact spectroscopy, lead.

Развит метод экспериментального определения спектральной функции электрон-фононного взаимодействия (СФ ЭФВ) для сверхпроводников с сильной связью. Данный метод основан на анализе нелинейностей вольт-амперной характеристики точечного гетероконтакта сверхпроводник-нормальный металл, которые возникают в упругой компоненте тока через гетероконтакт вследствие зависимости комплексной функции энергетической щели сверхпроводника от энергии квазичастиц и имеют общую природу с наблюдаемыми для сверхпроводящих туннельных контактов. Объектом исследования выбран свинец как типичный сверхпроводник с сильным ЭФВ. Полученная путем численного решения уравнений Элиашберга по методу Макмиллана-Роуэлла СФ ЭФВ согласуется с результатами упругой туннельной спектроскопии сверхпроводников и неупругой микроконтактной спектроскопии в нормальном состоянии.

Ключевые слова: сверхпроводимость, электрон-фононное взаимодействие, микроконтактная спектроскопия, свинец.

Розвинено метод експериментального визначення спектральної функції електрон-фононної взаємодії (СФ ЕФВ) для надпровідників із сильним зв'язком. Даний метод заснований на аналізі нелінійностей вольт-амперної характеристики точкового гетероконтакту надпровідник-нормальний метал, які виникають у пружній компоненті струму через гетероконтакт внаслідок залежності комплексної функції енергетичної щілини надпровідника від енергії квазічастинок і мають спільну природу із такими, що спостерігаються для надпровідних тунельних контактів. Об'єктом дослідження обрано свинець як типовий надпровідник з сильною ЕФВ. Отримана шляхом чисельного розв'язання рівнянь Еліашберга за методом Макмілана-Роуела СФ ЕФВ узгоджується з результатами пружною тунельної спектроскопії надпровідників і непружної мікроконтактної спектроскопії у нормальному стані.

Ключові слова: надпровідність, електрон-фононна взаємодія, мікроконтактна спектроскопія, свинець.

Formulation of the problem

Method of inelastic point contact spectroscopy of the electron-phonon interaction (EPI) in metals [1,2] that was proposed in [3] and later was theoretically substantiated in [4] is based on analysis of small nonlinearity of the point contact current-voltage characteristic (IVC) caused by generation of the nonequilibrium phonons within the contact. The method makes it possible to determine the spectral function of the EPI (SF EPI) that is regarded to be the most detailed characteristic of the electron-phonon system. In the case of the superconducting point contacts (S-c-S) and the point heterocontacts superconductor-normal metal (S-c-N) the theory of the inelastic point contact spectroscopy EPI in superconductors with weak EPI [5,6] had demonstrated its validity throughout the cycle of works [7] where for the first time manifestations of the EPI-related effects were observed experimentally in the characteristics of superconducting point contacts. At the same time the experimental studies [7,8] revealed several discrepancies with predictions of the theory [5,6] that were not without a reason attributed to the strong EPI in [8] the superconductor (Pb) used in the mentioned experiments. Later on the theory of conductivity of the S-c-N contacts containing a strong-EPI superconductor [9] provided a proof that the elastic component of the current through the contact is a nonlinear one and that the nonlinearities were caused by dependence of the function of the energy gap on the energy in a very similar way to the elastic tunnel spectroscopy of the EPI in superconductors [10,11].

The normalized differential conductivity of the S-c-N point contact in the clean limit (i.e. the “Knudsen limit” that is called sometimes the ballistic current regime) equals in accordance to [9]

$$G(\omega)=\frac{\sigma_S}{\sigma_N}=1+\left|\frac{\Delta(\omega)}{\omega+\sqrt{\omega^2-\Delta^2(\omega)}}\right|^2, \text{ eV= ħω} \quad (1)$$

and it differs from the normalized conductivity of a tunnel contact [10,11]

$$N(\omega)=\frac{\sigma_S}{\sigma_N}=\mathrm{Re}\frac{\omega}{\sqrt{\omega^2-\Delta^2(\omega)}}, \quad \text{eV = ħω} \quad (2)$$

which is the tunnel density of states. In (1,2) σ_S, σ_N are the contact differential conductivities for the superconducting and the normal state respectively of the superconducting electrode that is made of a metal under investigation, ħω is the energy of quasiparticles, e is the elementary charge, and V is the biasing voltage applied to the contact.

In the context of the method of elastic tunnel spectroscopy the normalized differential conductivity is employed for reconstruction of the SF EPI by means of numerical solution of the Eliashberg equations of the phonon model of superconductivity.

The mentioned above considerations provide a ground for formulation of the goal of the current research. Namely the basic idea of it is in the use of the point contact experimental data instead of the data associated with the tunnel effect for reconstruction of the EPI function by solving the Eliashberg equations.

Method of reconstruction of the EPI function

Calculations of the SF EPI g(ω) are based on numerical solution of the system of two integral Eliashberg equations at T = 0 for an isotropic superconductor [12,13]:

$$\Delta(\omega)=\frac{1}{Z(\omega)}\int_{\Delta_0}^{\omega_c}\mathrm{Re}\left\{\frac{\Delta(\omega')}{\left[\omega'^2-\Delta^2(\omega')\right]^{1/2}}\right\}* \quad (3)$$
$$*\left[K^+(\omega,\omega')-\mu^*\right]d\omega',$$

$$\left[1-Z(\omega)\right]\omega=\frac{1}{Z(\omega)}\int_{\Delta_0}^{\omega_c}\mathrm{Re}\left\{\frac{\omega'}{\left[\omega'^2-\Delta^2(\omega')\right]^{1/2}}\right\}*$$
$$*K^-(\omega,\omega')d\omega',$$

where the cores are

$$K^\pm(\omega,\omega')=\int_0^\infty g(\omega'')\left(\frac{1}{\omega''+\omega'+\omega+iO^+}\pm\right.$$
$$\left.\pm\frac{1}{\omega''+\omega'-\omega-iO^+}\right)d\omega''.$$

Here Δ(ω) is the complex function of the energy gap, Z(ω) is the complex renormalization function, μ^* is the coulomb pseudopotential, and ω_c is the cut-off frequency. The latter is usually taken as $\omega_c \approx 5\omega_{max}$, where ω_{max} is the highest frequency of the single-phonon part the EPI spectrum.

We used the McMillan-Rowell method [10,14] for our search of the solution of the equations (3). This iteration method includes two nested cycles called the outer and the inner iteration loops. The input parameters for the inner loop are the experimentally determined half-width of the energy gap Δ_0, the seed value for the coulomb pseudopotential μ^*, and a reasonable zero-approximation $g^{(0)}(\omega)$ for the g(ω) function (see for example [12]). These parameters are set to the Eliashberg equations, and the solution for the function Δ(ω) that is a complex one is corrected in accordance with the following condition $\Delta(\Delta_0) = \Delta_0$. After that the value μ^* is used again along with the $g^{(0)}(\omega)$ for getting the next approximation for the Δ(ω), and so on. The iteration process in the internal loop is stopped when the difference between the last Δ(ω) and next to the last one riches experimentally sound limit. The function Δ(ω) obtained in the inner loop is employed for the use in the outer loop for calculations of the normalized conductivity of a contact that is along with the experimentally measured normalised conductivity serves in turn for further correction of the initial zero approximation $g^{(0)}(\omega)$ for the EPI function. The latter procedure is based on the minimization by means of the variation method of the functional derivative $\partial[\sigma_S(\omega)/\sigma_N(\omega)]/\partial g(\omega)$ [14]. The EPI function $g^{(1)}(\omega)$ of the first approximation produced in the outer iteration loop then feeds the inner loop for further adjustment of the Δ(ω). The function $g^{(2)}(\omega)$ is then found in the same way, and the process lasts until the limit of experimental accuracy for the contact conductivity is reached. The corrections of the g(ω) are made within the interval ω_1 to ω_{max}, where $\hbar\omega_1 = \Delta_0 + \delta$. In practice $\delta \approx$ 1-2 meV. For the region $0 < \omega < \omega_1$

the approximation ~ ω^2 is in effect.

Measurement technique and experimental data

Lead was chosen for this study as a superconductor with one of the greatest values of the EPI constant $\lambda = 1.55$. It should be noted that the mercury only among the other metallic elements demonstrates the greater $\lambda = 1.6$ [10]. That is why results on the tunnel effect in lead are traditionally used in development of computer programs for reconstruction the SF EPI g(ω) by the McMillan-Rowell method [10,14] or by the competitive D'yachenko method [11,15] (see the references in [16]). The tabulated tunnel data are available from [1,17] (in [1] a table of the function g(ω) [18] computed by D'yachenko method is given), and can be employed for tests.

In our experiments the point contacts were connected in the 4-wire scheme way to the measurement setup operating in the current-source mode for both the biasing and the modulation signals. The dependencies

$$V_1(V) = \frac{i}{\sqrt{2}} \frac{dV}{dI}(V),$$

and

$$V_2(V) = \frac{i^2}{4\sqrt{2}} \frac{d^2V}{dI^2}(V)$$

were measured. Here V_1 and V_2 are detected effective voltages corresponding to the first and the second harmonic of the modulation current with the amplitude i. These dependencies are proportional to the first and to the second derivatives of the IVC as the functions of the applied voltage bias V. For the conventional normal state point contacts such the dependencies are called the point contact spectra, and they routinely serve for reconstruction of the point contact EPI functions $g_{pc}(\omega)$ [1,19].

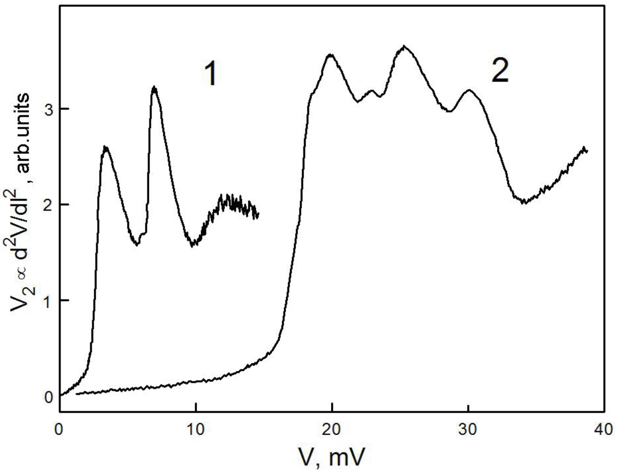

Fig.1. Inelastic EPI point contact spectra of lead (1) and ruthenium (2) captured at T = 1.5 K for the point contacts at the normal state. The superconductivity of lead is supressed by external constant magnetic field.

The sliding-type point contacts [1] were produced in the course of the experiment. The superconducting sample electrodes were spark-cut from the bulk polycrystalline high-purity C-000 lead. For making the normal counter-electrodes that needed for fabrication of the heterocontacts we used high-quality single crystals of Ru ($\rho_{300K}/\rho_{4.2K} \approx 2500$). While making the Pb/Ru contacts the geometrical axis of the contact was oriented along the $[10\bar{1}0]$ direction in the Ru-electrodes to ensure provision of the most "hard" EPI spectrum in Ru [7] that does not overlap with the EPI spectrum of Pb (Fig.1).

Prior to mounting to the mechanical cell for point contact fabrication [20] and putting into He-atmosphere of the cryostat the surface of the electrodes was exposed to electro-chemical etching. All the measurements were carried out at the temperature T = 1.5 K. For that temperature the energy gap 2Δ in the superconducting lead perfectly matches the value $2\Delta_0$ at T = 0. In the case of necessity in order to create the normal-state point contacts the superconductivity in the lead electrode was suppressed by the external constant magnetic field. The magnitude of the resistance of the point contact in the normal state R_0 was defined as R at $V \rightarrow 0$ using the initial linear region of the IVC. The typical values for the resistance in the normal state were about several Ohm.

Being one of the key input parameters for the task of solution of the Eliashberg equation (3) solution the value Δ_0 was determined experimentally by localizing the subharmonics of the gap at the IVC derivatives of the homocontacts Pb/Pb (Fig.2).

Subharmonics of the gap seen at the IVCs of the point contacts S-c-S are caused by the multiple processes of Andreev reflection (see for instance [2,10]), and manifest themselves as peculiarities at the derivatives of the IVC located at the voltages $V = 2\Delta/en$, where n = 1,

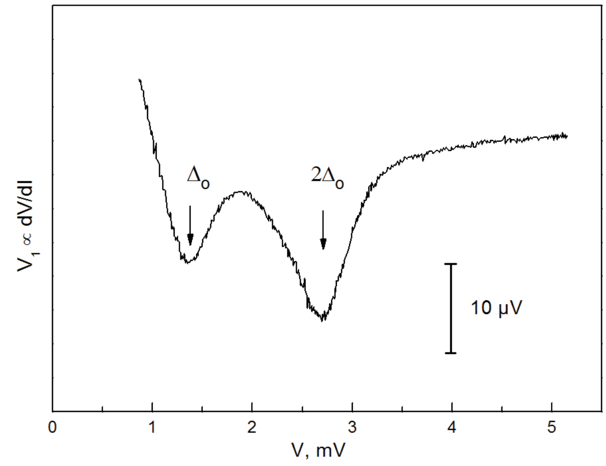

Fig.2. The subharmonic $2\Delta/n$ (n = 1, 2, …) gap structure at the first derivative of the IVC of the superconductive lead point contact at T = 1.5 K. R_0 = 5.8 Ohm.

2, 3, … . Such the peculiarities correspond to minima at the dependencies of the differential resistance $R(V) = dV/dI(V)$ vs voltage. We found the value $\Delta_0 = 1.35$ meV for the superconducting lead. This figure precisely matches the one that was obtained earlier in the experiment on the tunnel contacts made of the lead taken from the same piece of metal [21].

It should be underlined that measurement of the energy gap using the subharmonic gap structure at the IVS derivatives is a direct experimental method. While the Blonder-Tinkham-Klapwijk method (BTK) [22] that is called Andreev spectroscopy requires cumbersome numerical calculations for retrieving the value of the Δ the accuracy of the direct experimental sub-harmonics based method is limited only by the precision of the voltmeter used for measurements of the voltage applied to the contact.

In the course of preparations for the numerical calculations employing the McMillan-Rowell method the dependencies $V_2(V)$ for the point heterocontacts Pb/Pu were measured for the case of the superconducting and the normal state of the Pb-electrode.

Results of the numeric calculations and discussion

The problem of determination of the SF EPI from the Eliashberg equations on the basis of point contact experimental data can be split into few tasks. The solution of them in context of the present work is described below.

In accordance to the theory [9] the differential conductivity of the S-c-N contact (1) exhibits maxima, and the differential resistance accordingly shows minima in the vicinity of the characteristic phonon frequencies that are shifted by the value of Δ_0 to higher energies in comparison to the phonon density of states (PDOS) $F(\omega)$ and the SF EPI. Therefore at the second derivatives $d^2V/dI^2(V)$ certain characteristic peculiarities in the form of the derivatives of a functional minimum should be seen. Lead has the face-centred cubic crystalline structure with one atom per the unit cell. Its PDOS is comparatively simple with its two-peak $F(\omega)$ structure. One of the peaks corresponds to the transversal acoustic oscillations and the other peak is due to the longitudinal ones. In order to make a comparison with the experimental results the first and the second derivatives of the S-c-N point contact IVC were calculated using the relationship (1) and the tables [17] of the real and imaginary parts of the $\Delta(\omega)$ for Pb. The computations revealed minima of the contacts' differential resistance in the vicinity of the T- and L-maximum of the $F(\omega)$ and the EPI spectrum in lead. The amplitude of the calculated minima makes up few percent of the R_0 (Fig.3).

The numerically derived second derivative of the IVC (1 at the Fig.4) clearly demonstrates a non-monotonic structure as a result of the non-trivial form of the $\Delta(\omega)$ and reproduces all the thin details of the experimental curve 3 at the Fig.4. At the same time a BCS-based calculation

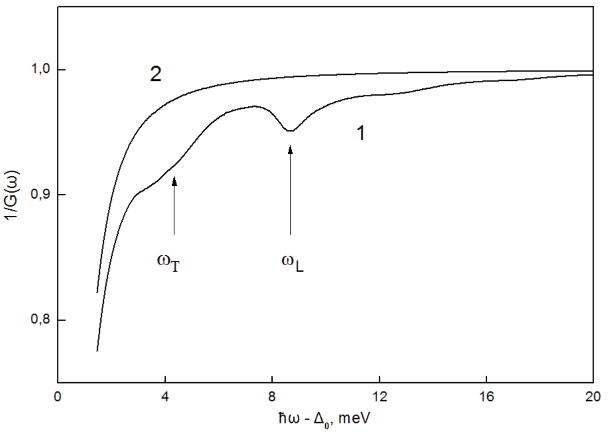

Fig.3. The calculated from the relationship (1) normalized differential resistance $R \equiv 1/G$ of the S-c-N point contact:

1 – with the use of the function $\Delta(\omega)$ for Pb [17];

2 – in accordance to the BCS model $\Delta(\omega) = \Delta_0 = \text{const}$.

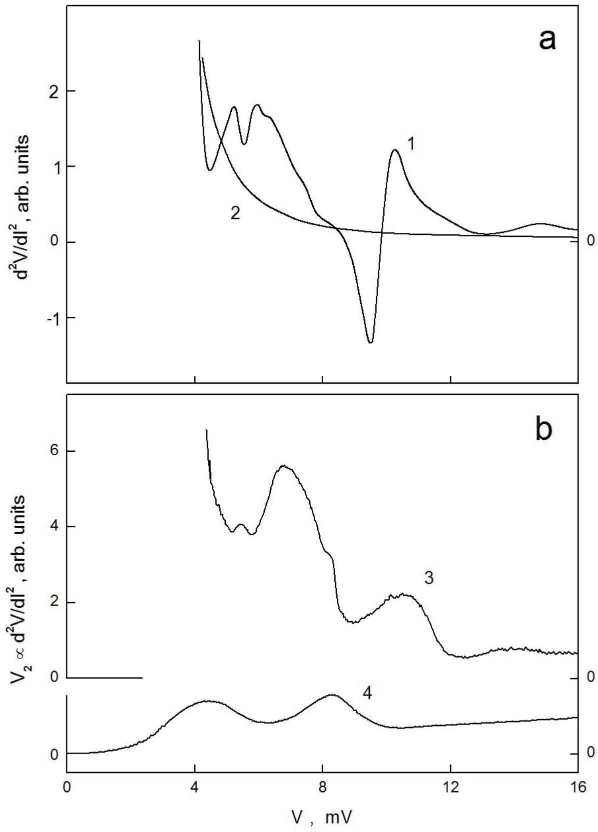

Fig.4. Comparison of the calculated (panel a) and experimental (panel b) IVC second derivatives:

1 – numerical calculations for the S-c-N contact following relationship (1) with the use of the function $\Delta(\omega)$ for Pb [17]; 2 – the same calculation in the BCS model $\Delta(\omega) = \Delta_0 = \text{const}$. 3, 4 – graphs $V_2(V)$ μ $d^2V/dI^2(V)$, captured at T = 1.5 K for the heterocontact Pb/Ru in the case of the superconducting (1) and the normal (2) state of thee lead electrode (the y-scale for 1, 2 is the same). $R_0 = 6.5$ Ohm.

produces featureless smooth dependencies $1/G(\omega) \propto dV/dI(V)$ and $d^2V/dI^2(V)$ (see the curve 2 at Fig.3 and 2 at Fig.4).

The well-known Nernst-Lindemann model when the PDOS is shaped by two characteristic phonon frequencies only provides a sound choice for the zero-approximation of the $g^{(0)}(\omega)$ in our case. In accordance with this model we assume presence of only two maxima of the T- and the L-type that in turn means complete degeneration of the oscillatory T-branches. The maxima are modelled by isosceles triangles of equal height. Every of the tree branches of the phonon spectrum contributes equally to the $g^{(0)}(\omega)$, and therefore for observation of the normalization criterion the area associated with the T-maximum is two times greater than the area of the L-maximum. In our modelling of the zero-approximation EPI function $g^{(0)}(\omega)$ we set locations for the T- and L- maxima as 4.4 and 8.5 meV respectively while the maximal EPI spectrum frequency was taken 10 meV. The latter value can be estimated as $\omega_{max} \approx 2< \omega^2 >^{1/2}$, where the mean square phonon frequency $< \omega^2 >$ is calculated using the relationship [23] for the Debye temperature $\Theta_D = \frac{3}{2} < \omega^2 >^{1/2}$ which is derived from the theory of the momentums of frequency distributions.

In order to achieve better accuracy of the final product which is the EPI function we obtain the input dependence of the normalized differential resistance vs voltage by numerical integration of the measured second derivative of the IVC. Such a trick is often used in the course of handling the data of tunnel experiments [10]. The magnitude of the conductivity is normalized to the conductivity of the same point contact in the normal state when the superconductivity in the sample is destroyed by the external constant magnetic field. Prior to the normalization the inelastic contribution is removed from the superconducting state data. For that purpose we use the values $V_2(V)$ μ $d^2V/dI^2(V)$ for the contact in the normal state (4 at Fig.4) with the obvious substitution of the argument V to $V + \Delta_0$ [6,24].

To avoid the divergence in the transcendental equations (3) in the course of the calculations we produced expansions of the integrand into series in small parameter Δ^2/ω^2 as recommended in [25]. Following [26] the correction of the coulomb pseudopotential μ^* has not been made. At every step the value $\mu^* = 0.13$ [10] was adopted.

The resultant complex function $\Delta^{(2)}(\omega)$ has already been not far from the tabulated one [17]. Visibly good agreement of the $g(\omega)$ takes place if we compare it with the known functions for the film tunnel contacts [10,17] as well as with the results of the inelastic point contact spectroscopy in the normal state. At the Fig.5 the calculated EPI function $g(\omega)$ is presented along with the EPI point contact function $g_{pc}(\omega)$.

The latter function is derived from the point contact spectrum $V_2(V)$ of homocontact Pb/Pb in the normal state (1 at Fig.1) as an output product of the modern version of the program [19]. At the Fig.5 the EPI functions are displayed for comparison in relative units (being normalized to theirs maximal values). However the absolute values of the $g(\omega)$ function can be easily recovered following [25,27] by means of adjustment to the known transition temperature $T_c = 7.19$ K in lead (for instance by employing the McMillan formula).

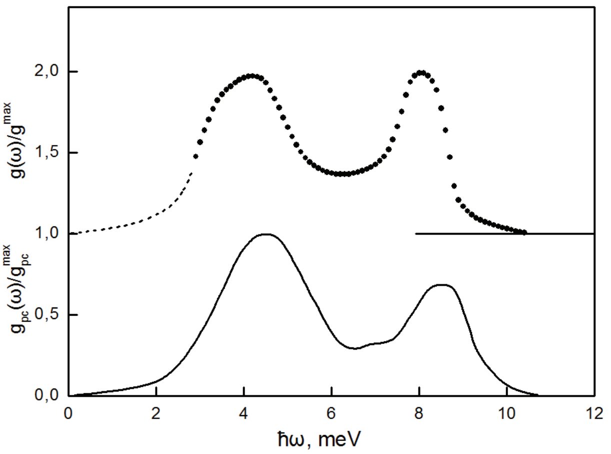

Fig.5. The spectral EPI functions in lead: the thermodynamic EPI function $g(\omega)$ derived by McMillan-Rowell method from the Pb/normal-metal point contact data, and the point contact EPI function $g_{pc}(\omega)$ reconstructed using Pb point contact spectrum in the normal state. For the $g(\omega)$ the beginning of the coordinate axis is shifted by 1 upwards.

The matching of the $g(\omega)$ function to its tunnel analogue clearly depends on the number of iterations in every cycle of the algorithm of solution of the Eliashberg equations. However the different relative intensities of the $g(\omega)$ and $g_{pc}(\omega)$ maxima at the Fig.5 are explained by presence of the form-factor for the $g_{pc}(\omega)$ [1] under the integral, and also by the temperature and instrumental smearing [7] of the sharper L-maximum at 8.5 meV in the EPI point contact spectrum in lead (1 at Fig.1) which was used as a starting position in the process of reconstruction of the $g_{pc}(\omega)$.

Conclusion

The primary results of the current work can be presented in the form of short statements.

1. For the first time the method of elastic point contact spectroscopy has been employed as a practically suitable tool for reconstruction of the spectral function of the EPI in superconductors by means of numerical solution of the system of Eliashberg equations. The proposed approach is based on use of experimental data for the conductivity of the point contact but not on the tunnel data.

2. In a short perspective the proposed approach is about to complement the arsenal of methods for investigation of new superconductors with high values of critical magnetic fields that are not always achievable in the laboratory environment.

3. The method of reconstruction of the SF EPI may be critically important in those cases when fabrication of the high-quality tunnel contacts turns out to be difficult or impossible and it becomes advantageous eliminating many problems of investigation the high-purity superconductors in the form of bulk samples or high-quality single crystals.

One of the authors (AVK) would like to express his gratitude to M. A. Belogolovskii, A. I. D'yachenko, and Yu. A. Kolesnichenko for the discussions on numerical solutions of the Eliashberg equations.

1. A.V. Khotkevich, I.K. Yanson. Atlas of Point Contact Spectra of Electron-Phonon Interactions in Metals, Kluwer Acad. Publ., Boston/Dordrecht/London (1995), p.168.
2. Yu.G. Naidyuk, I.K. Yanson. Point Contact Spectroscopy, USA, New York (2004), p.300.
3. I.K. Yanson. Sov.Phys.JETP, 39, 506 (1974).
4. I.O. Kulik, A.N. Omelyanchouk, R.I. Shekhter. Sov.J.Low Temp.Phys., 3, 740 (1977).
5. V.A. Khlus, A.N. Omelyanchouk. Sov.J.Low Temp.Phys. 9, 189, (1983).
6. V.A. Khlus. J.Low Temp.Phys., 9, 510 (1983).
7. A.V. Khotkevich. Doct.Habil.Thesis, Inst.Low Temp.&Eng., Ukraine, Kharkov (1990), p.323.
8. G.V. Kamarchuk, A.V. Khotkevich, I.K. Yanson. Sov.Phys. Solid State, 28, 254 1986).
9. A.N. Omelyanchouk, S.I. Beloborod'ko, I.O. Kulik. Sov.J.Low Temp.Phys., 14, 630 (1988).
10. E.L. Wolf. Principles of Electron Tunneling Spectroscopy. Oxford Univ.press, USA, New York (1985), p.576.
11. V.M. Svistunov, M.A. Belogolovskii. Tunneling Spectroscopy of Quasi-Particle Exitations in Metals. Nauk. Dumka, Ukraine, Kiev (1986), p.147.
12. D.J. Skalapino, J.R. Schrieffer, J.W Wilkins. Phys.Rev., 148, 1, 263 (1966).
13. J.R. Schrieffer. Theory of Superconductivity. Front.Phys.20, USA, Florida (1964), p.282.
14. W.L. McMillan, J.M. Rowell. Phys.Rev.Lett., 14, 4, 108 (1965).
15. D'yachenko A.I. PhD Thesis, Ukraine, Donetsk (1979), p.127.
16. A.V. Khotkevich. Prepr. №24-89 Inst.Low.Temp. Phys.&Eng., Kharkov (1989), p.42.
17. J.M. Rowell, W.L. McMillan, R.C. Dynes. Preprint Bell Labs, Murray Hill, USA, New Jersey (1973), p.83.
18. V.M. Svistunov, O.I. Chernyak, M.A. Belogolovskii, A.I. D'yachenko. Phil.Mag., B43, 1, 75 (1981).
19. V.V. Khotkevich, A.V. Khotkevich. Deposited paper №164-B86, VINITI, USSR, Moskow (1986), p.74.
20. N.L. Bobrov, L.F. Rybalchenko, A.V. Khotkevich, P.N. Chubov, I.K. Yanson. USSR Inv.Cert.№1631626, Bull.№8 (1991).
21. O.P. Balkashin, I.K. Yanson, A.V. Khotkevich. Sov.Phys. JETP, 45, 618 (1977).
22. G.E. Blonder, M. Tinkham, T.M. Klapwijk. Phys.Rev., B25, 7, 4515 (1982).
23. F.J. Pinski, P.B. Allen, W.H. Butler. Phys.Rev., B23, 10, 5080 (1981).
24. N.L. Bobrov, A.V. Khotkevich, G.V. Kamarchuk, P.N. Chubov. J.Low Temp.Phys., 40, 3, 251 (2014).
25. N.V. Zavaritskii. JETP Lett., 6, 155 (1967).
26. P. Morel, P.W.Anderson. Phys.Rev., 125, 4, 1263 (1963).
27. V.V. Khotkevich, A.V. Khotkevich, A.P. Zhernov, T.N. Kulagina, E.C. Falques. Izv. Kharkov Univ. Ser. Fiz. №476, 96 (2000).

Вісник ХНУ, № 1135, серія «Фізика», вип. 21, 2014. с. 33-37

PACS number(s): 66.30.Lw, 82.47.Ed, 61.43.Bn

Optimizing oxygen diffusion in cathode materials for solid oxide fuel cells

A. I. Chroneos[1'2], D. Parfitt[2]

department of Materials Science and Metallurgy, University of Cambridge,
Cambridge CB2 3QZ, United Kingdom
Department of Materials, Imperial College London,
London SW7 2AZ, United Kingdom

Recent investigations have revealed that the Ruddlesden-Popper series ($A_n+_1B_nO_{3n}+_1$) and the layered perovskite $LnBaCo_2O_5$+s (Ln = rare-earth cations) are promising as cathodes for intermediate temperature solid oxide fuel cells. For these to be economical the oxygen diffusion must be maximized. In the present investigation we propose strategies for optimizing oxygen diffusion in these materials by modifying the oxygen stoichiometry, the composition and cation disorder.

Keywords: $LnBa_{1\cdot x}Sr_xCo_2O_5$+s; Molecular dynamics; Oxygen migration; Anisotropy

Recent investigations have revealed that the Ruddlesden-Popper series ($A_n+_1B_nO_{3n}+_1$) and the layered perovskite $LnBaCo_2O_5$+s (Ln = rare-earth cations) are promising as cathodes for intermediate temperature solid oxide fuel cells. For these to be economical the oxygen diffusion must be maximized. In the present investigation we propose strategies for optimizing oxygen diffusion in these materials by modifying the oxygen stoichiometry, the composition and cation disorder.

Keywords: $LnBa_{1\cdot x}Sr_xCo_2O_5$+s; Molecular dynamics; Oxygen migration; Anisotropy

Recent investigations have revealed that the Ruddlesden-Popper series ($A_n+_1B_nO_{3n}+_1$) and the layered perovskite $LnBaCo_2O_5$+s (Ln = rare-earth cations) are promising as cathodes for intermediate temperature solid oxide fuel cells. For these to be economical the oxygen diffusion must be maximized. In the present investigation we propose strategies for optimizing oxygen diffusion in these materials by modifying the oxygen stoichiometry, the composition and cation disorder.

Keywords: $LnBa_{1\cdot x}Sr_xCo_2O_5$+s; Molecular dynamics; Oxygen migration; Anisotropy

Introduction

Solid Oxide Fuel Cell (SOFC) technology is characterized by the potential for high efficiency energy conversion in conjunction with reduced emission of green house gases compared to other more traditional power generation routes [1-16]. An active field of research is aiming at lowering the operating temperature of SOFCs to the intermediate temperature range (500-700) °C [1]. This operating temperature range will result in more economic SOFCs, however, it is necessary to maintain their performance. The key is to improve the catalytic activity of cathode materials as these can become a significant source of electric losses at lower temperatures [2,3]. The main factors affecting cathode performance is the high electronic conductivity, the surface exchange rate and the oxygen diffusion coefficient [4,5]. The development of novel cathode materials has focused on perovskite-related materials such as the first members of the Ruddlesden-Popper (RP) series (i.e. A_2BO_4) [6-8], and the layered perovskite $LnBaCo_2O_5$+s (Ln = rare-earth cations) [9-12].

Molecular dynamics (MD) simulations enable the calculation of the energetic of diffusion (i.e. activation energy of diffusion and diffusivity of ions) as well as the mechanism of diffusion of complex systems, which are difficult to investigate experimentally [17,18]. The aim of the present study is to identify how oxygen diffusion in cathode materials can be maximized by varying the oxygen stoichiometry, the composition and cation disorder. Paradigms include the first members of the RP series (A2BO4) and the archetypal double perovskite, $GdBaCo_2O_5$+s.

Methodology

Classical MD simulations were used in the Born description of the ionic crystal lattice [19]. Ions interact via simple short-range parameterised pair potentials and the long range Coulombic interactions are summed using the Ewald method [20]. The short range interactions were described using parameterised Buckingham potentials [21], which were previously established by comparison to experimental work [18,2224]. The DL POLY simulation package was used for all the calculations [25]. For the $GdBaCo_2O_5$+s, initial configurations we used 8 x 8 x 4 supercells for the high temperature phase to give a total

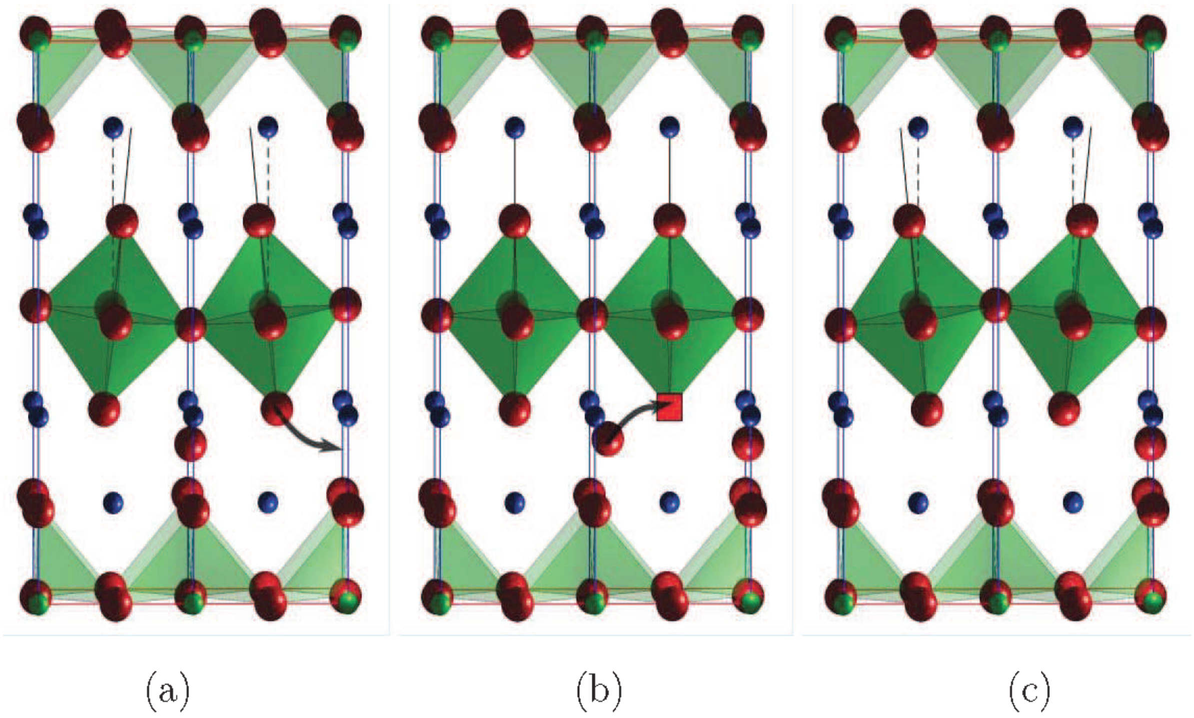
(a) (b) (c)

Fig. 1 Characteristic snapshots of the oxygen (red spheres) interstitialcy diffusion mechanism predicted by MD calculations for the diffusion of Pr2NiO4+8. Praseodymium ions are represented by blue spheres, the oxygen vacancy by a red square, nickel-oxygen polyhedral in green.

of around 5000 ions. The partial occupancy of the oxygen sites was handled by taking an appropriately sized random sample of fractionally occupied oxygen sites in each layer. To predict the oxygen diffusion mechanism, stoichiometrics of 8 = 0.5 were studied in a wide temperature range (T = 800-1400K). Initial calculations were performed for 10000 timesteps with the atoms coupled to a barostat allowing the cell parameters to change at each timestep. Thereafter, a further 10000 timesteps were performed under constant volume conditions to allow the cell to come into equilibrium at the new volume. Data collection runs were restarted from these final simulations and lasted for 10 ps to ensure adequate statistical sampling. The temperature and pressure were corrected using the Nose-Hoover Thermostat [26,27].

Results and discussion

MD simulations clarified the landscape regarding oxygen ion diffusion in the RP materials La_2NiO_{4+8}, Pr_2NiO_{4+8} and La_2CoO_{4+8}. It was calculated that oxygen migrates via a highly anisotropic interstitialcy mechanism in the a-b planes (refer to Figure 1) [8,28-30]. This is consistent with the recent ToF-SIMS results of Sayers et al. [31] for oxygen transport in $La_2NiO_4+_8$ with an activation energy of 0.54 eV again in excellent agreement with the MD results (0.51 eV, Ref. 8). Parfitt et al. [28] calculated the oxygen activation energy of $Pr_2NiO_{4+}S$ over a range of hyperstoichiometries. These results were again in excellent agreement with the experimental work of Boehm

Table 1. Activation energies of oxygen self-diffusion in $A_2BO_{4+\delta}$.

Material	E_a (eV)	Methodology	Comment	Reference
$La_2CoO_{4+\delta}$	0.73–0.80	DFT	Interstitialcy mechanism	29
$La_2CoO_{4+\delta}$	0.31	MD	Interstitialcy mechanism	29
$Pr_2NiO_{4+\delta}$	0.49–0.64	MD	Interstitialcy mechanism	28
$Pr_2NiO_{4+\delta}$	0.6	Experimental	Interstitialcy mechanism	6
$La_2NiO_{4+\delta}$	0.51	MD	Interstitialcy mechanism	8
$La_2NiO_{4+\delta}$	0.54	Experimental	Polycrystal, TOF-SIMS	31

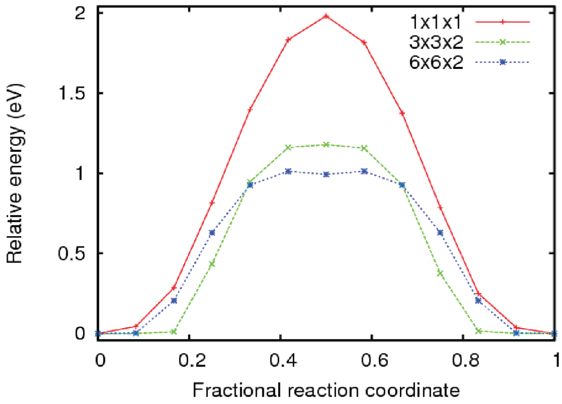

Fig. 2. Relative energies of each nudged elastic band image showing the variation of calculated transition barrier for a single oxygen interstitial as a function of supercell size. The start and end points of the pathway are at the same minimised structure for each supercell and are offset to zero energy.

et al. [6] (Table 1). The MD work of Parfitt et al. [28] highlights that the activation energy of oxygen migration is strongly dependent upon the degree of hyperstoichiometry ranging from 0.49eV (for 8 = 0.025) to 0.64 eV (for 8 = 0.20)]. The oxygen diffusivity, D, at a temperature T can be described by, D = [Oi] f exp(-Em/kBT). This links D with the concentration of oxygen interstitials, [Oi] and the energy barrier to migration, Em [28]. f is the correlation factor and kB is Boltzmann's constant [28]. The rise of [O$_i$] will result in a rapid increase of the diffusivity and this is not surprising as it is the interstitials that mediate the oxygen diffusion process in these materials [28-31]. At high enough [O$_i$] (here 8 ~ 0.02, [28]) the diffusivity levels off. This is due to the rise in the effective migration barrier due to the increased formation energy of oxygen interstitials (because of the presence of other pre-existing neighbouring interstitials). This leads to the stiffening of the lattice as the NiO6 sub-lattice is pinned as a consequence of the additional oxygen interstitials. This reduces the ease with which the NiO$_6$ octahedra tilt to accommodate the diffusion of oxygen ions (see Figure 1). We tested this by performing static and atomistic simulations in conjunction with the nudged elastic band method for La$_2$CoO$_4$+$_8$ another promising RP compound (Figure 2) [29,32].

In Figure 2 we show the results of the interstitialcy mechanism calculated for a single oxygen interstitial for varying tessellations of the original tetragonal unit cell. Defect-defect interactions are significant in these layered compounds; this is both a result of Coulomb repulsion between oxygen interstiatials and the interaction of strain fields surrounding the defects. Figure 2 demonstrates that the migration energy barrier depends quite strongly upon the concentration of oxygen interstitials. For the higher [Oi] (smaller cell, 1x1x1, Figure 2) the migration energy is about double compared to the migration energy of the larger cells (6x6x2, Figure 2).

In ordered GdBaCo$_2$O$_5$+$_8$ the activation energy was calculated to be 0.5 eV (for T = 800-1400 K). This is in excellent agreement with the determined value of 0.6 eV that was obtained by using isotopic exchange techniques in the temperature range 600K to 1000K [9,32]. Notably

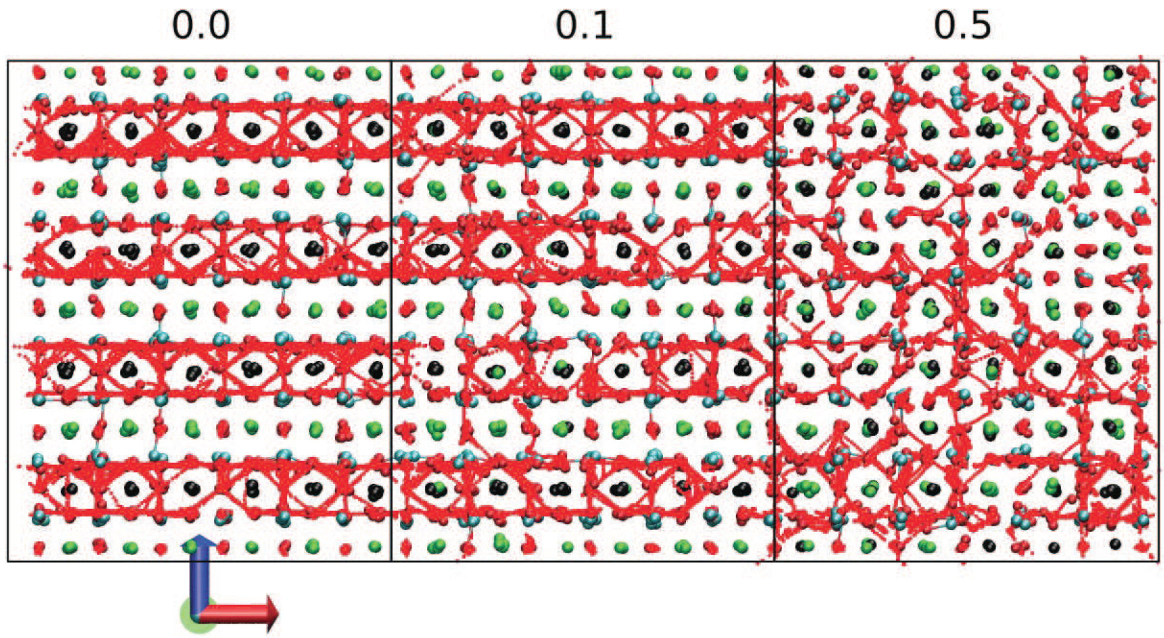

Fig.3. The impact of disorder in the Gd/Ba sublattice on the oxygen diffusion mechanism in GdBaCo$_2$O$_{55}$. For no disorder in the Gd/Ba sublattice (i.e. F = 0.0) diffusion is anisotropic and prevalent in the ab-plane, whereas as disorder increases case (i.e. from F = 0.1 to F = 0.5) diffusion is becoming more isotropic.

the high temperature tetragonal phase of $GdBaCo_2O_5+_8$ exhibits a highly anisotropic oxygen diffusion long the a-b plane [33]. This is facilitated by oxygen vacancies consistently with experimental results [9].

In $GdBaCo_2O_5+_8$ there is antisite disorder between the Gd and Ba cations. This can be quantified via a parameter F = $[Gd_{Ba}]/([Gd_{Ba}]+[Gd_{Gd}])$, which represents the probability of finding a Gd ion on a Ba site. Here [MN] represents the concentration of M ions on an N site. The fully disordered case corresponds to F = 0.5 in which there is a 50% probability of either site being occupied by a Gd or Ba ion. Conversely for the fully ordered case F = 0.

Figure 3 schematically illustrates the effect of cation disorder upon the oxygen diffusion mechanism for ordered (F = 0) and as disorder increases (i.e. from F = 0.1 to F = 0.5) $GdBaCo_2O_{5+8}$. It is evident that the formation of cation disordered defects leads to migration pathways along the c-axis and thus the increase of disorder results to the reduction of anisotropy of oxygen diffusion in $GdBaCo_2O_5+_8$. Interestingly for F = 0.5 there is a decrease in the oxygen diffusivity and the diffusion mechanism is almost isotropic. This can appear to be counterintuitive as it would be anticipated that order in the oxygen sublattice would be consistent with order in the cation sublattice as they are interknitted in each other in an oxide. This would in turn imply that cation sublattice ordered oxides would have limited oxygen diffusion. Interestingly, Norby

[34] has previously investigated these issues and calculated that there are oxides with cation order and anion disorder, which demonstrate high oxygen diffusivities. The key is that in the disordered oxides defect trapping can lower the measured diffusivity. In a recent static atomistic simulation study by Seymour et al. [35] it was calculated that there is significant defect trapping between oxygen vacancies and Ba in a Ln site antisites in $LnBaCo_2Os_+S$ (where Ln = rare-earth) double perovskites. This in turn may lower the diffusivity. As the levels of cation disorder are important, experimental conditions such as sample preparation and thermal history can be very used to tune the anisotropy of the material.

Other issues need to be also considered when selecting materials for SOFC cathodes. Notably, Kim et al. [11] propose the application of intermediate rare-earth cations such as samarium to avoid the decrease in the thermal expansion coefficient, which can be associated with the smaller rare-earth cations. Substituting barium with strontium in $GdBaCo_2O_5+_8$ leads to $GdBa_{1-x}Sr_xCo_2O_5+_8$, which has an increased oxygen content [12]. These substitutions may also affect the diffusion properties and are presently under investigation.

Conclusions

To conclude, atomic scale modelling is valble in the optimisation and design of cathode materials for SOFC. In the RP series the composition influences high oxygen diffusion, with $La_2CoO_4+_8$ having the lowest activation energy of diffusion. In these materials the increase of the oxygen hyperstoichiometry (i.e. the oxygen interstitials that mediate diffusion) also affect the energetics of oxygen transport. This effect, however, soon levels-off as the hyperstoichiometry is increased. In $GdBaCo_2O_5+_8$ and related compounds cation disorder is of critical importance not only for the energetics of diffusion but also for the diffusion mechanism. The more disordered the material the more isotropic oxygen transport will become. As a design criterion we need an ordered GdBaCo2O5+8 to optimise the oxygen diffusion. A second design criterion valid for all the materials considered here is that we need to grow crystals along the ab-plane to optimise the oxygen diffusion properties. Investigations are in progress to quantify the impact of cation disorder on the oxygen diffusivity in GdBaCo2O5+8 and to clarify further the energetics of oxygen self-diffusion in La2CoO4+8.

Computing resources were provided by the HPC facility of Imperial College London.

1. B.C.H. Steele, A. Heinzel, Nature 414 (2001) 345.
2. J. Fleig, Ann. Rev. Mater. Res. 33 (2003) 361.
3. Z. Shao, S.M. Haile, J. Ahn, P.D. Ronney, Z. Zhan, S.A. Barnett, Nature 435 (2005) 3676.
4. S.B. Adler, J.A. Lane, B.C.H. Steele, J. Electrochem. Soc. 143 (1996) 3554.
5. S.B. Adler, Solid State Ionics 111 (1998) 125.
6. E. Boehm, J.M. Bassat, P. Dordor, F. Mauvy, J.C. Grenier, Ph. Stevens, Solid State Ionics 176 (2005) 2717.
7. M. Burriel, G. Garcia, J. Santiso, J.A. Kilner, R.J. Chater, S.J. Skinner, J. Mater. Chem. 18 (2008) 416.
8. A. Chroneos, D. Parfitt, J.A. Kilner, R. W. Grimes, J. Mater. Chem. 20 (2010) 266.
9. A. Tarancon, S.J. Skinner, R.J. Chater, F. Hernandez-Ramirez, J.A. Kilner, J. Mater. Chem. 17 (2007) 3175.
10. C.J. Zhu, X.M. Liu, C.S. Yi, D. Yan, W.H. Su, J. Power Sources 185 (2008) 193.
11. J.H. Kim, A. Manthiran, J. Electrochem. Soc. 155 (2008) B385.
12. J.H. Kim, F. Prado, A. Manthiran, J. Electrochem. Soc. 155 (2008) B1023.
13. A.A. Taskin, A.N. Lavrov, Y. Ando, Appl. Phys. Lett. 86 (2005) 91910.
14. D.J. Liu, J. Almer, Appl. Phys. Lett. 94 (2009) 224106.
15. J. Hermet, G. Geneste, G. Dezanneau, Appl. Phys. Lett. 97 (2010) 174102.
16. A. Aguadero, J.A. Alonso, R. Martinez-Coronado, M.J. Martinez-Lope, M.T. Fernandez-Diaz, J. Appl. Phys. 109 (2011) 034907.
17. G.N. Mazo, S.N. Savvin, Solid State Ionics 175 (2004) 371.
18. D. Rupasov, A. Chroneos, D. Parfitt, J.A. Kilner, R.W. Grimes, S.Ya. Istomin, E.V. Antipov, Phys. Rev. B 79 (2009)

172102.

19. M. Born, J.E. Mayer, Z. Phys. 75 (1932) 1.
20. P.P. Ewald, Ann. Phys. 64 (1921) 253.
21. R.A. Buckingham, Proc. Royal Soc. London Series A, Math. Phys. Sci. 168 (1938) 264.
22. R.W. Grimes, D.J. Binks, A.B. Lidiard, Philos. Mag. A 72 (1995) 651.
23. R.W. Grimes, G. Busker, M.A. McCoy, A. Chroneos, J.A. Kilner, S. P. Chen, Ber. Bunsenges. Phys. Chem. 101 (1997) 1204.
24. M.R. Levy, C.R. Stanek, A. Chroneos, R.W. Grimes, Solid State Sci. 9 (2007) 588.
25. W. Smith, T.R. Forester, J. Mol. Graphics 14 (1996) 136.
26. S. Nose, J. Chem. Phys. 81 (1984) 511.
27. W.G. Hoover, Phys. Rev. A 31 91985) 1695.
28. D. Parfitt, A. Chroneos, J.A. Kilner, R.W. Grimes, Phys. Chem. Chem. Phys. 12 (2010) 6834.
29. A. Kushima, D. Parfitt, A. Chroneos, B. Yildiz, J.A. Kilner, R.W. Grimes, Phys. Chem. Chem. Phys. In press.
30. E.N. Naumovich, V.V. Kharton, J. Molec. Struct.: THEOCHEM 946 (2010) 57.
31. R. Sayers, R.A. De Souza, J.A. Kilner, S.J. Skinner, Solid State Ionics 181 (2010) 386.
32. C.N. Munnings, S.J. Skinner, G. Amow, P.S. Whitfield, I.J. Davidson, Solid State Ionics 176 (2005) 1895.
33. D. Parfitt, A. Chroneos, A. Tarancon, J.A. Kilner, J. Mater. Chem. In press.
34. T. Norby, J. Mater. Chem. 11 (2001) 11.
35. I. Seymour, A. Chroneos, J.A. Kilner, R.W. Grimes unpublished results.

Вісник ХНУ, № 1135, серія «Фізика», вип. 21, 2014. с. 38-41

PACS: 03.65.Sq, 03.65.Ta
УДК: 538.915, 53.01

Quantum approach by the Lindblad master equation to the autonomous oscillator in hard excitation regime

M.A. Ialovega[1], E.D. Vol[2]

[1]V.N. Karazin Kharkov National University,
61022 Kharkov, Ukraine. Email: ialoveganicolas@gmail.com
[2]B. Verkin Institute for Low Temperature Physics and Engineering NASU,
61103 Kharkov, Ukraine. Email: vol@ilt.kharkov.ua

We propose the simple quantum model of nonlinear autonomous oscillator in hard excitation regime. We originate from classical equations of motion for similar oscillator and quantize them using the Lindblad master equation for the density matrix of this system. The solution for the populations of the stationary states of such oscillator may be explicitly found in the case when nonlinearity parameters of the problem are small. It was shown that in this situation there are three distinct regimes of behavior of the model. We compare properties of this model with corresponding ones of another closely connected open system, namely quantum oscillator in soft excitation regime. We discuss a possible applications of the results obtained.

Keywords: an auto-oscillator in hard excitation regime, the Lindblad master equation, density matrix, population inversion.

В роботі вперше запропонована квантова модель осцилятора з жорстким режимом збудження. Ми виходимо з класичних рівнянь руху для такого осцилятора і знаходимо їх квантовий аналог, використовуючи відповідне рівняння Ліндблада для еволюції матриці густини квантової системи. Отримано аналітичний розв'язок в стаціонарному випадку, коли нелінійні параметри задачі малі. Знайдено чотири різних режими поведінки даної системи. Порівнюються властивості розглянутої моделі з відповідними властивостями аналогічної системи – квантового осцилятора з м'яким режимом збудження. Обговорюється можливе використання отриманих результатів.

Ключові слова: жорстке збудження, рівняння Ліндблада, матриця густини, інверсія заселеності.

В работе впервые предложена квантовая версия модели для автономного осциллятора с жестким режимом возбуждения. Мы исходим из классических уравнений движения для такого осциллятора и находим их квантовый аналог, используя соответствующее уравнение Линдблада для эволюции матрицы плотности квантовой системы. Получено аналитическое решение в стационарном случае, когда нелинейные параметры задачи малы. Найдены четыре различных режима поведения данной системы. Сравниваются свойства рассмотренной модели с соответствующими свойствами аналогичной системы – квантового осциллятора с мягким возбуждением. Обсуждается возможное применение полученных результатов.

Ключевые слова: жесткое возбуждение, уравнение Линдблада, матрица плотности, инверсия населенностей.

The main goal of the paper is to introduce and consider the quantum model of nonlinear autonomous oscillator (AO) in hard excitation regime. Our basic tool for solving this problem is the Lindblad master equation (LME) which describes the evolution of any (closed or open) Markov quantum system. Clearly, the first aspiration that arises when one starts to study the behavior of certain complex quantum open system (OS) is the desire to reduce it to some more simple standard model that permits the rigorous mathematical analysis. In the theory of open systems there are at least two similar models namely 1) AO in soft excitation and 2) AO in hard excitation regimes. The first case has been studied in [1] where to this end the semi-classical method of quantization of classical non-Hamiltonian systems was proposed. Therefore in the present paper we will focus our attention on the case of AO in hard excitation regime. Note that AO both in soft and hard excitation regimes are widely used in physics, biology and other sciences. For example, in physics, an oscillator in soft excitation regime used as the standard model of a generator of electromagnetic oscillations. As regards to AO in hard excitation this system finds various applications aside from physics as well for example in biology where similar model can be applied for the description of activity of the giant axon of a squid in sea water [2]. Now let us describe briefly the method of transition from known classical equations of motion to quantum dynamics by means of the LME. The basic idea in this way is the correspondence principle in the form proposed by P. Dirac in his prominent book [3].

It turns out that the broad interpretation of correspondence principle allows one under certain conditions to quantize (at least in the semi-classical approximation) the equations of motion not only for closed but also for open systems using the LME which realizes the quantum description of the evolution of quantum OS in the Markov approximation. This equation for the evolution of the density matrix of quantum OS $\hat\rho$ has the following general form [4]:

$$\frac{d\rho}{dt} = -\frac{i}{\hbar}[\hat H,\hat\rho] + \\ +\sum_{j=1}^{N}\{[\hat R_j\hat\rho,\hat R_j^+] + \{[\hat R_j,\hat\rho\ \hat R_j^+]\}, \tag{1}$$

where $\hat H$ is - an hermitian operator (Hamiltonian), which describes the internal dynamics of quantum OS, and a set of non-hermitian operators $\{\hat R_j,\hat R_j^+\}$ - models its interaction with the environment.

The recipe of quantization proposed in [1] consists of three successive steps (its justification and all details see in this paper). Firstly, the input dynamical equations should be presented in the special form allowing the quantization (FAQ). In the simplest case of a system with one degree of freedom with dynamical variables x and p or equivalently with complex coordinate $z = \frac{x+\dot p}{\sqrt{2}}$ the desired equation in FAQ looks as follows:

$$\frac{dz}{dt} = -\frac{i}{\hbar}\frac{dH}{dz^*} + \\ +\sum_{j=1}^{N}\{\bar R_j\frac{dR_j}{dz^*} - R_j\frac{d\bar R_j}{dz^*}\}, \tag{2}$$

This representation, in the case where it is found determines automatically the classical functions $H(z,z^*)$, $R(z,z^*)$ and $\bar R(z,z^*)$ entered in Eq. (2).

The second step is to find the quantum analogs of classical functions $\hat H$, $\hat R$. $\hat R^+$. To this end the simple rule can be proposed: one should replace in all classical variables the coordinates z and z^* by the Bose operators $\hat a$ and $\hat a^+$. After this procedure the operators $\hat H$, $\hat R$ and $\hat R^+$ thus obtained should be substituted into the LME. Now let us demonstrate in detail how the method of quantization operates in the case of AO in hard excitation regime. We will consider the simplest model of such oscillator that can be described by the following equation of motion for the complex coordinate z [5]:

$$\dot z = -i\omega z - \varepsilon_1 z + \varepsilon_2 z\,|\,z\,|^2 - cz\,|\,z\,|^4\ , \tag{3}$$

where ε_1, ε_2 and c - are the constants, describing the behavior of the oscillator. We are interested mainly in possible stationary regimes of the behavior of the oscillator as functions of these constants. One can easily verify that Eq. (3) can be represented in the FAQ. Indeed let us introduce the functions $H = \omega z^* z$, $R_1 = \sqrt{\varepsilon_1}z$, $R_2 = \sqrt{\frac{\varepsilon_2}{2}}z^{*2}$, $R_3 = \sqrt{\frac{c}{3}}z^3$. After that r.h.s. of Eq. (3) may be written down as:

$$-i\omega z - \varepsilon_1 z + \varepsilon_2 z\,|\,z\,|^2 - cz\,|\,z\,|^4 = \\ = -\frac{i}{\hbar}\frac{dH}{dz^*} + \sum_{j=1}^{N}\{\bar R_j\frac{dR_j}{dz^*} - R_j\frac{d\bar R_j}{dz^*}\}\ . \tag{4}$$

In what follows we will assume that $c = 1$ since this case is always may be achieved by choosing of appropriate time scale. According to the above mentioned recipe of quantization the LME for the AO in hard excitation regime takes the following form:

$$\frac{d\rho}{dt} = \\ -\frac{i}{\hbar}[\hat H,\hat\rho] + \sum_{j=1}^{N}\{[\hat R_j\hat\rho,\hat R_j^+] + \{[\hat R_j,\hat\rho\ \hat R_j^+]\},$$

where $\hat R_1 = \sqrt{\varepsilon_1}\hat a$, $\hat R_2 = \sqrt{\frac{\varepsilon_2}{2}}\hat a^{+2}$ (5) $\hat R_3 = \sqrt{\frac{1}{3}}\hat a^3$.

From physical reasons we expect that steady regimes of classical system (3) in quantum case correspond to stationary states of its quantum analogue described by the LME (5). We'll seek the stationary solutions of Eq. (5) in the form $\hat\rho_s = \sum_{n=0}^{\infty}|n\rangle\rho_n\langle n|$, where $|n\rangle$ - are eigenvectors of the operator $\hat n$ or in other words we assume that $\hat\rho_s$ is a certain function of operator $\hat n$. Using the standard rule of commutation: $\left[\hat a,\hat a^+\right] = 1$ after the simple algebra we obtain the following difference equation for the unknown coefficients ρ_n:

$$\varepsilon_1((n+1)\rho_{n+1} - n\rho_n) + \varepsilon_2((n-1)n\rho_{n-2} - \\ -(n+2)(n-1)\rho_n) + ((n+3)(n+2)(n+1)\rho_{n+3} - \\ -(n-2)(n-1)n\rho_n) = 0 \tag{6}$$

Let us introduce the generating function for these coefficients according the definition: $G(u) = \sum_{n=0}^{\infty}\rho_n u^n$.

Substituting this expression into the Eq. (6) we obtain the following third order differential equation for the $G(u)$:

$$(1-u^3)\frac{d^3G}{du^3} + \varepsilon_2(u^2-1)\frac{d^2(u^2G)}{du^2} + \varepsilon_1(1-u)\frac{dG}{du} = 0 \tag{7}$$

It is impossible to find out analytical solution of Eq. (7) in analytical form therefore we restrict ourselves to the case when coefficients ε_1 and ε_2 are small but their ratio can be of arbitrary value namely $\frac{\varepsilon_2}{\varepsilon_1} = \gamma$. In the lowest approximation (when both ε_1 and ε_2 tend to zero), $G(u)$ is a certain polynomial of the second order: $G(u) = \rho_0 + \rho_1 u + \rho_2 u^2$, where populations ρ_n should be found as follows. Substituting the expression for $G(u)$ in Eq. (7) and taking into account that all $\rho_i = 0$ when $i > 2$, and by virtue of normalization condition $\rho_0 + \rho_1 + \rho_2 = 1$ we obtain the closed system of equations for the nonzero coefficients ρ_n that takes the form:

$$\begin{cases} \rho_1 = 2\gamma\rho_0 \\ \rho_2 = (6\gamma + 1)\rho_1 / 2 \\ \rho_0 + \rho_1 + \rho_2 = 1 \end{cases} \tag{8}$$

The solution of Eq. (8) looks as follows:

$$\begin{cases} \rho_0 = \dfrac{1}{6\gamma^2 + 3\gamma + 1} \\ \rho_1 = \dfrac{2\gamma}{6\gamma^2 + 3\gamma + 1} \\ \rho_2 = \dfrac{6\gamma^2 + \gamma}{6\gamma^2 + 3\gamma + 1} \end{cases} \tag{9}$$

Having in hands this solution we can analyze possible regimes of behavior for AO in hard excitation regime as the function of the parameter γ. First of all let us clarify two limiting cases a) $\gamma \to 0$ and b) $\gamma \to \infty$.

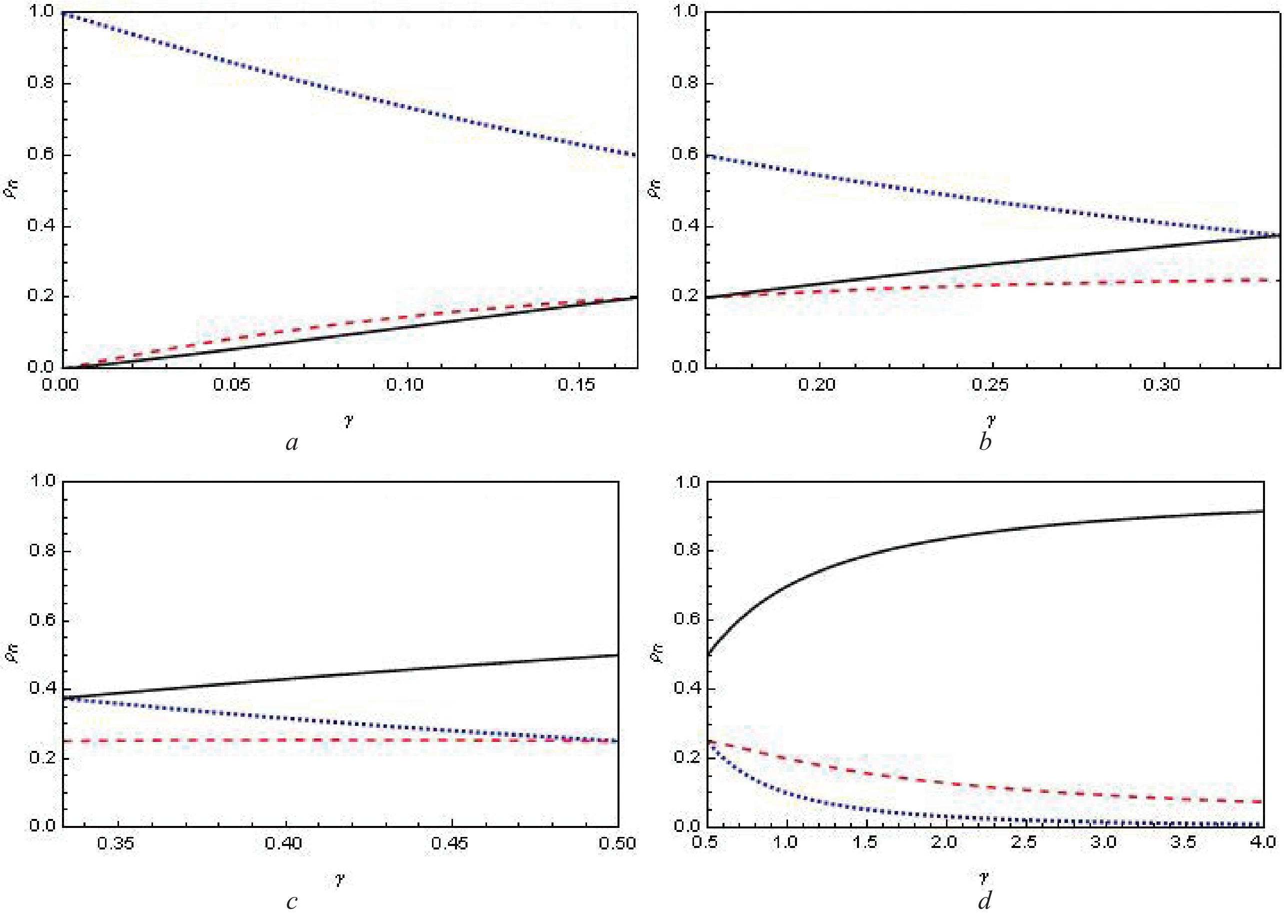

a *b*

c *d*

Fig. 1. Population levels ρ_0 (spotted curves), ρ_1 (dashed curves) and ρ_2 (solid curves) as the function of single physical constant γ. These four regimes correspond to the four ranges of γ: a) $\gamma \le \frac{1}{6}$, then $\rho_0 > \rho_1 > \rho_2$; b) $\frac{1}{6} < \gamma < \frac{1}{3}$ then $\rho_0 > \rho_2 > \rho_1$; c) $\frac{1}{3} < \gamma < \frac{1}{2}$ then $\rho_2 > \rho_0 > \rho_1$; d) $\frac{1}{2} < \gamma$ then $\rho_2 > \rho_1 > \rho_0$.

In the case a) $\rho_0 \to 1$, ρ_1, ρ_2 tend to zero. This case corresponds to the vacuum state of AO in hard excitation regime (or the state of rest in the classical case).

In the case b) $\rho_0 = \rho_1 = 0$, and $\rho_2 = 1$. It is the case of maximum possible excitation of the system in our approximation. It corresponds to the state above threshold in classical case.

Now one can specify the four distinct regimes of the AO under study depended on the parameter $\gamma = \frac{\varepsilon_2}{\varepsilon_1}$. These regimes are represented in Fig. 1.

It is interesting to compare the results obtained in the present paper with similar ones relating to AO in soft excitation regime. Remind that generation function $G(u)$ for stationary states of AO in soft excitation regime satisfies to the following second order differential equation (see Eq. (26) in Ref. [1]):

$$(1+u)\frac{d^2G}{du^2} - vu\frac{dG}{du} - vG = 0 \tag{10}$$

where v is the only nonlinear parameter of this oscillator. Its solution that satisfies all physical conditions can be expressed as

$$G(u) = \frac{F(1, v, v(1+u))}{F(1, v, 2v)}, \tag{11}$$

where $F(a,b,x)$ is the standard confluent hypergeometric function. Using the expansion of this function namely: $F(a,b,x) = 1 + \frac{a}{b}x + \frac{a(a+1)}{2!b(b+1)}x + \ldots$ one can easily see that if parameter of nonlinearity v tends to zero, corresponding generation function tends to:

$$G_0(u) = \frac{2+u}{3}. \tag{12}$$

Thus the AO in soft excitation regime with small nonlinearity reduced to the two level system with population $\frac{2}{3}$ in the lower and $\frac{1}{3}$ in the upper level respectively. We see that compared with such primitive regime the case AO in hard excitation regime reveals considerably much more rich behavior.

Conclusions:

1. The quantum model of an AO in hard excitation regime is firstly proposed in this paper.
2. Using the methods of the quantum theory of the OQS, the Lindblad equation for the density matrix of the oscillator was obtained, and it was found the four distinct regimes of the oscillator in the case when the physical parameters of the model are small.
3. It was shown that the quantum model proposed here has much more rich behavior then AO in soft excitation regime.
4. It is worth to note that the model AO in hard excitation regime considered in present paper, if it should be implemented as physical device, naturally realizes the curious case of three level quantum system in which one can achieves (by varying only single parameter) population inversion on any desired pair of levels.

1. E. D. Vol, Phys Rev. A73, 062113 (2006).
2. Glass L. Mackey M. From clocks to chaos: The rhythms of life. (Princeton University Press, 1988).
3. P. A. M. Dirac, The Principles of Quantum Mechanics, 4th ed. (Clarendon, Oxford, 1958).
4. G. Lindblad, Commun. Math. Phys. 48, 119 (1976).
5. V. I. Arnold, Geometrical Methods in the Theory of Ordinary Differential Equations, 2nd ed. (Springer, New York, 1988).

Вісник ХНУ, № 1135, серія «Фізика», вип. 21, 2014. с. 42-43

УДК 537.61; 538.955
PACS: 78.20.Ls, 75.10.Lp, 71.23.An

Magnetoelastic communication and attenuation collective excitations in model of half metal

E.S. Orel

O.M. Beketov National University of Urban Economy in Kharkiv,
Ukraine, 61002, Kharkov, Revolyutsii street, 12

It is viewed signal attenuation collective excitations in model of half metal and the effect of qualitative calculation of decay time and threshold quasimomentums of magnons is presented. Emission by magnons of phonons at zero temperature is provided at the expense of take off by a magnetic subsystem of energy from a radiant of an exterior electromagnetic field. In the field of poles of the mass functional the spin-lattice interaction main effect is signal attenuation of magnons, as should be reflected, mainly, in spectrums of magnetic uptake. The effect from a renormalization magnon energies in this spectroscopic field becomes less significant for the shape of a curve of magnetic uptake.

Keywords: phonon, magnon, spin-lattice interaction, signal attenuation of magnons, the mass functional.

Рассмотрено затухание коллективных возбуждений в модели половинного металла и представлен результат качественного расчета времени затухания и пороговых квазиимпульсов магнонов. Испускание магнонами фононов при нулевой температуре обеспечивается за счет отбора магнитной подсистемой энергии от источника внешнего электромагнитного поля. В области полюсов массового оператора основным эффектом спин-решеточного взаимодействия является затухание магнонов, что и должно отразиться, главным образом, на спектрах магнитного поглощения. Эффект же от перенормировки магнонных энергий в этой спектральной области становится менее значимым для формы кривой магнитного поглощения.

Ключевые слова: фонон, магнон, спин-решеточное взаимодействие, затухание магнонов, массовый оператор.

Розглянуто загасання колективних збуджень в моделі половинного металу і представлений результат якісного розрахунку часу загасання і порогових квазіімпульсів магнонів. Випускання магнонами фононів при нульовій температурі забезпечується за рахунок відбору магнітною підсистемою енергії від джерела зовнішнього електромагнітного поля. У області полюсів масового оператора основним ефектом спін-граткової взаємодії є загасання магнонів, що і повинне відбитися, головним чином, на спектрах магнітного поглинання. Ефект же від перенормування магнонних енергій в цій спектральній області стає менш значимим для форми кривої магнітного поглинання.

Ключові слова: фонон, магнон, спін-граткова взаємодія, загасання магнонов, масовий оператор.

Introduction

The model of half-note metals is widely used for description of row of oxides with the mixed valency, possessing a “giant magnetoresistance” effect (GMR) [1]. Magnetoelastic interaction substantially influences on forming of basic properties of these connections. However the known methods [2] calculation of parameters of damping of magnons, as a result magnon–phonon interaction appear of the little use for these systems, as an indirect exchange in them has not Heisenberg nature [1,3]. This paper presents the results of qualitative calculation of the damping time and threshold quasimomenta of magnons.

Magnon damping time

The characteristic magnon damping time is given by the expression [7]

$$\tau_{\mathbf{q}} = \frac{\hbar}{2\,\mathrm{Im}\,\varepsilon(\mathbf{q})}\ , \qquad (1)$$

where $\hbar$ is Planck’s constant, and Im ε (q) is the imaginary part of the magnon energy. Last, concordantly [5], equal

$$\mathrm{Im}\,\varepsilon_{ac(op)\xi}(\mathbf{q}) = \frac{2\left\langle s^z\right\rangle S_{ac(op)}}{\left\langle S^z + s^z\right\rangle} M''\left(\mathbf{q}, \varepsilon_{ac(op)\xi}(\mathbf{q})\right), \qquad (2)$$

where $M''\left(\mathbf{q}, \varepsilon_{ac(op)\xi}(\mathbf{q})\right)$ is imaginary part of mass operator of magnon–phonon interaction; **q** is a quasimomenta of magnons; $\left\langle S^z\right\rangle = \frac{1}{N}\sum_{\lambda}\left\langle 0\left|S^z_{\lambda}\right|0\right\rangle$, $\left\langle s^z\right\rangle = \frac{1}{N}\sum_{\mathbf{k}}\left(n_{\mathbf{k}\uparrow} - n_{\mathbf{k}\downarrow}\right)$ are mean values of local and quasilocal spins; $S_{ac} = \left\langle S^z\right\rangle$, $S_{op} = \left\langle s^z\right\rangle$.

Magnons with quasimomenta not exceeding a critical value $q_{0ac(op)}$, are not damped [3], and therefore one is interested in an estimate of (2) near the edge of the magnon band, where $q \approx q_B$. Maximal value of imaginary part of mass operator in (2) does not exceed a value

$$M''_{ac(op)\max} = \frac{0.7\pi\xi^2 \left\langle s^z \right\rangle S_{ac(op)}}{\left\langle S^z + s^z \right\rangle} N_{ac(op)\nu\max} \ , \qquad (3)$$

where $\hat{\imath} = W\frac{A_0}{a}$, $W=2zT$ is a width of magnon zone, z is a coordinating number of crystalline lattice, T is the hopping integral of electrons between nearest-neighbor sites; $A_0 = \frac{\hbar}{\sqrt{2M_a\nu_0}}$ it is the rms amplitude of zero vibrations of ions with border frequency of $\nu_0 \approx \theta_D$ [6], a is a constant of crystalline lattice; M_a is mass of atom.

A size $N_{ac(op)\nu\max}(\mathbf{q},\varepsilon)$ is a maximal value of function

$$N_{ac(op)\nu}(\mathbf{q},\varepsilon) = \frac{1}{N}\sum_{\mathbf{p}} \delta\left(\varepsilon - \varepsilon_{ac(op)+}(\mathbf{q},\mathbf{p})\right),$$

arrived at, in three-dimensional case, at the value of quasimomenta of magnon of $q_{max} \sim q_B$. The interval of nonzero values of $N_{ac(op)\nu\max}(\mathbf{q},\varepsilon)$ is equal to the sum of the widths of the magnon and phonon bands. Using the normalization

$$\int N_{ac(op)\nu\max}(\mathbf{q},\varepsilon) d\varepsilon = 1$$

we estimate $N_{ac(op)\nu}(\mathbf{q},\varepsilon)$ by the quantity $(\text{è}_C + \text{è}_D)^{-1}$ for the acoustic band and $(\text{è}'_C + \text{è}_D)^{-1}$ for the optical band, where $\text{è}' = \text{è}\frac{\left\langle S^Z \right\rangle}{\left\langle s^Z \right\rangle}$. Using (3) and and supposing $W=1.5$ eV, $S=1.5$, $A_0/a \approx 4\times10^{-3}$ (values characteristic of GMR are connections of $La_{2/3}Ca_{1/3}MnO_3$ [1]), we obtain from (1) and (2) the following estimate for the magnons with Brillouin quasimomentum q_B:

$$\mathrm{Im}\,\varepsilon_{ac}(q_B) \approx 6.8\cdot10^{-5}\theta_C, \tau_{ac} \approx 1.5\cdot10^{-10}s\ ,$$

$$\mathrm{Im}\,\varepsilon_{op}(q_B) \approx 7.5\cdot10^{-6}\theta'_C, \tau_{op} \approx 8\cdot10^{-11}s.$$

Thus, material part of mass operator determines renormalization of magnon spectrum, and imaginary is fading of magnons. Both effects depend on a temperature. Fading of magnons at a zero temperature is caused by the spontaneous emitting of phonon, at eventual - also and by their absorption.

Threshold of magnon damping

The effect at zero temperature, as follows from [3], has a threshold character: only those magnons with a quasimomentum exceeding the value

$$q_{0ac} = \frac{1}{a}\cdot\arcsin\frac{\pi\left\langle S^z + s^z \right\rangle \text{è}_{\mathrm{D}}}{2T\sin\left(\mathrm{k_F}a\right)} \qquad (4)$$

for an acoustic branch, and value

$$q_{0op} = \frac{1}{a}\cdot\arcsin\frac{\pi\left\langle s^z \right\rangle\left\langle S^z + s^z \right\rangle \text{è}_{\mathrm{D}}}{2T\left\langle S^z \right\rangle\sin\left(\mathrm{k_F}a\right)} \ - \qquad (5)$$

for the optical branch are damped (for simplicity we have given the expressions obtained for the one-dimensional case[3]).

It should be noted that existence of threshold quasimomentums of (4) and (5) has direct attitude toward the effect of Tcherenkov [8]: group speed of magnons with a quasimomentum exceeding these values more speed of sound appears in an environment, in this connection and there is a spontaneous radiation by them phonon. If speeds of magnons do not exceed speed of sound, i.e. if argument of the arcsine in (4) and (5) more unit (in the threedimensional case with allowance for the estimate of the Curie temperature, this should correspond to the inequality $\theta_D > \theta_C$) appears, the magnon–phonon coupling at a zero temperature does not result in fading of magnons.

The emission of phonons by magnons at zero temperature is made possible by the extraction of energy from the source of the external electromagnetic field by the magnetic subsystem. In area of poles of mass operator the basic effect of spin-lattice coupling is fading of magnons, what must be reflected, mainly, on the spectrums of magnetic absorption. An effect from renormalization of the magnons energies in this spectral region becomes less meaningful for the form of curve of magnetic absorption.

Conclusions

Thus, the magnon–phonon coupling at a zero temperature qualitative does not change character of spectrum of magnetic absorption at $q < q_{0ac(op)}$. It changes the form of магнонных zones only, frequencies of heterogeneous resonances fall down in this connection. At an eventual temperature, as a result of absorption of thermal phonons, all of the magnons will be damped.

1. E. Dagotto, T. Hotta, A.Moreo. Phys. Rep., v. 344, 1 (2001).
2. A. I. Akhiezer, V. G. Bar'yakhtar, and S. V. Peletminski., *Spin Waves*, North-Holland, Amsterdam (1968), Nauka, Moscow (1967).
3. A. B. Beznosov and E. S. Orel. Fiz. Nizk. Temp., 30, 9, 958 (2004).
4. V. Yu. Irkhin, M. I. Katsnelson. Eur. Phys. J, B 30, 481 (2002).
5. A. B. Beznosov and E. S. Orel. Fiz. Nizk. Temp., 30, 10, 1053 (2004).
6. S.H. Liu. Physics and Chemistry of REM, Amsterdam – New York: North Holl. Publ. Comp., (1978), v. 1, 3, p. 235.
7. A. S. Davydov, *Solid State Theory* [in Russian], Nauka, Moscow (1976).
8. L. D. Landau and E. M. Lifshitz, *Electrodynamics of Continuous Media*, Pergamon Press, Oxford (1960), Gos. Izd-vo Fiz. Mat. Lit., Moscow (1959).

Вісник ХНУ, № 1135, серія «Фізика», вип. 21, 2014. с. 44-48

PACS:81.07.Ws;75.30.Gw
УДК 537.622.6

Magnetic anisotropy of an ensemble of Ca-substituted barium hexaferrite nanoparticles

L.P.Ol’khovik , N.M.Borisova, Z.V.Golubenko, K.A.Mozul, Z.I.Sizova, E.V.Shurinova

V.N.Karazin Kharkiv National University
61022, Kharkov, Svobody, 4
giperbola79@mail.ru

We studied the parameters of the effective magnetic anisotropy of system of hexaferrite nanocrystals of composition $Ca_{0.5}Ba_{0.5}Fe_{12}O_{19}$ with an average size 35 nm at 300 K. The constant the field of effective magnetic anisotropy determined from the magnetization curves using five different methods. It was shown that the substitution of ions Ba^{2+} by ions Ca^{2+}, while maintaining the magnetic matrix, the constant K_a^{ef} reduced by more than half in comparison with unsubstituted composition powder of the same dispersion.

Keywords: barium hexaferrite, cations substation, nanocrystall, magnetic anisopropy.

Исследовались параметры эффективной магнитной анизотропии системы нанокристаллов гексаферрита $Ca_{0.5}Ba_{0.5}Fe_{12}O_{19}$ со средним размером 35 нм при 300 К. Константа и поле эффективной магнитной анизотропии определены из кривых намагничивания с помощью пяти различных методов. Показано, что в результате замещения ионов Ba^{2+} ионами Ca^{2+}, при сохранении магнитной матрицы, константа K_a^{ef} уменьшается более чем вдвое в сравнении с порошком незамещенного состава той же дисперсности.

Кючевые слова: гексаферрит бария, катионное замещение, нанокристалл, магнитная анизотропия.

Досліджувалися параметри ефективної магнітної анізотропії системи нанокристалів гексафериту складу $Ca_{0.5}Ba_{0.5}Fe_{12}O_{19}$ зі середнім розміром 35 нм при 300 К. Константа і поле ефективної магнітної анізотропії визначені з кривих намагнічування за допомогою п›яти різних методів. Показано, що в результаті заміщення іонів Ba^{2+} іонами Ca^{2+}, при збереженні магнітної матриці, константа K_a^{ef} зменшується більш ніж удвічі в порівнянні з порошком незаміщеного складу тієї ж дисперсності.

Ключові слова: гексаферит барію, катіонне заміщення, нанокристал, магнітна анізотропія.

Introduction

Barium hexaferrite $BaFe_{12}O_{19}$ is highly anisotropic ferrite. At room temperature, the constant of his magnetocrystalline anisotropy $K_1= 3.3\cdot10^6$ erg·cm^3, the anisotropy field $H_{ak} =17\cdot10^3$ Oe [1].

Magnetic parameters of small particles and their ensembles markedly differ from the magnetic parameters of macroanalogue that due to the existence of structurally defective surface layer that is comparable with the volume of the particle volume and has a “canted” magnetic structure [2]. Subsurface region makes a certain volumetric contribution to the effective magnetic anisotropy of the particles in the form of so-called “surface” anisotropy [3].

In [4] have been investigated in the temperature range (4.2 - 700 K) the anisotropic parameters of the barium ferrite nanocrystals with an average particle size of <d> = 60 nm and a thickness of <h>= 15 nm. The volume fraction of the -surface layer of the particles having a thickness of δ ~3.5 nm [5], was 45 %.

Effective magnetic anisotropy constant was determined using the law of approach to saturation magnetization [6]. At 300 K, it was to $2.5\cdot10^6$ erg·cm^{-3}, that is its value is different from the value for macroanalogue by 25 % due to the negative contribution of the “surface” anisotropy. In the same paper, using the method developed in [7], was found the distribution of particles by fields of effective magnetic anisotropy, according to which the average effective magnetic anisotropy field of the particles at 300 K is also different from H_{ak} of macroanalogue, towards reduction by 20%.

It was of interest to investigate the effect of partial substitution of Ba^{2+} ions by Ca^{2+} ions with preservation of the magnetic matrix, on the anisotropic properties of the nanodispersive particles of barium ferrite. Substitutions of this type were made for the hexaferrite macrosamples [8]. It was found that the magnetocrystalline anisotropy energy of Ca-substituted ferrite is described not only by a constant K_1, but also by constants of higher orders. In this case, the order of magnitude of K_2 is comparable with the K_1.

Method of preparation and certification of powder sample of composition $Ca_{0.5}Ba_{0.5}Fe_{12}O_{19}$

One of the primary conditions for obtaining particles of nanometer range is the creation of a high chemical homogeneity of the original ferrite mixture. This was accomplished by using the method that uses elements of the cryochemical technology.

Schematic block diagram of a method of producing ferrite particles is shown in Fig.1.

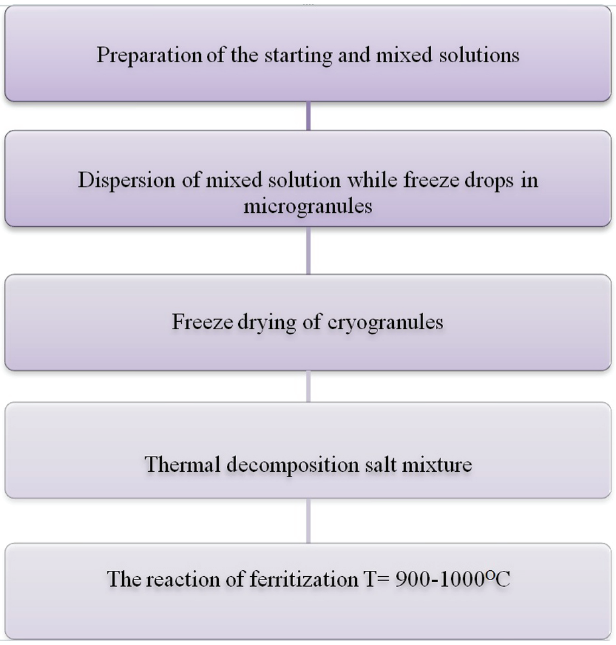

Fig.1. A block diagram of a method of obtaining nanodispersed ferrite powders using elements of cryochemical technology.

At the freezing step was conducted spraying of the solution which was a mixture of solutions of compatible salts of $Ca(CH_3COO)_2$, $Ba(NO_3)_2$, $Fe(CHOO)_3$ in a specified stoichiometric ratio, into an inert refrigerant. As refrigerant was used liquid nitrogen (~ 10 liters of nitrogen per 1 liter of solution). In the system was created a fixed pressure (0.12 - 0.2 atm), under the influence of which the working fluid is fed into the vortex chamber of injector. As a result, the jet of solution is divided into individual droplets of diameter 3-70 µm. Particles entering the liquid nitrogen are rapidly crystallized. As the inert gas injected to the installation under pressure, argon was used. Removal of the solvent from cryogranules was conducted by sublimation-drying – the process of transition of the solvent from the crystalline to the gaseous state, avoiding the liquid phase. This allowed minimizing the agglomeration of the formed particles of product on the freezing step by eliminating occurrence of the liquid phase in material.

A technological operation that preceding to the process of ferritization consists in the thermal decomposition of the salt components of the mixture. Value of thermolysis temperature of components mixture shouldn't be less than the decomposition temperature of each component. Of the above acetates the most high-temperature transition is $Ca(CH_3COO)_2 \rightarrow CaO$. In stages thermal decomposition of calcium acetate to oxide occurs in the form:

$$Ca(CH_3COO)_2 \xrightarrow[160^0 C]{} Ca_2C_2O_4 \xrightarrow[200^0 C]{}$$
$$CaCO_3 \xrightarrow[825^0 C]{} CaO$$

Considering the fact that for the macroscopic analogue of $Ca_{0,5}Ba_{0,5}Fe_{12}O_{19}$ full ferritization provides the temperature 1270 °C [9], that is much greater than for $BaFe_{12}O_{19}$ hexaferrite (1150 °C), in the case of highly dispersive particles ferritization was held at 900 °C instead of 800 °C for the base composition. This extremely low annealing temperature provided full ferritization, and helped to keep the size of the particles within the nanometer range.

X-ray phase analysis of the obtained powder showed it's a single-phase. Non-magnetic impurity content of α-Fe_2O_3 phase is insignificant, and do not exceed 6%.

To determine the size of the particles used electron microscopy. Electron microscopic studies were performed on a transmission electron microscope Selmi TEM-125 K. Fig. 2 shows a fragment of an electron-microscope image of the powder particles.

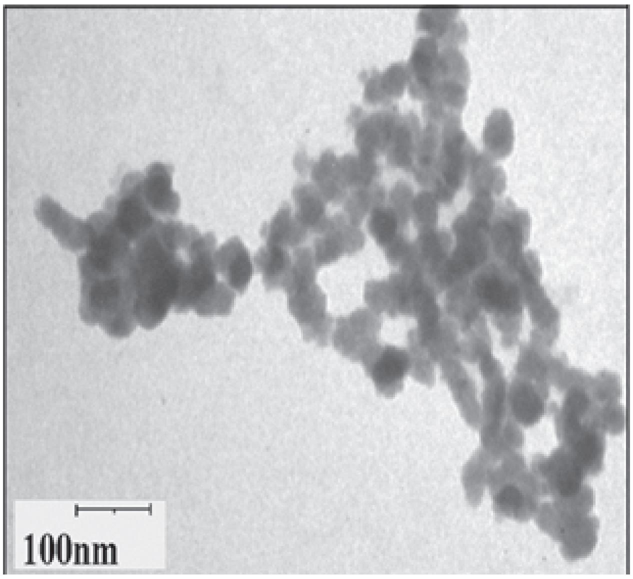

Fig.2. Electron microscopic picture of the powder particles of hexaferrite $Ca_{0.5}Ba_{0.5}Fe_{12}O_{19}$.

It can be seen that the particle size corresponds to the nanometer range. The average particle size <d> = 35 nm.

Basic magnetic measurements Results of the data processing

Magnetic measurements at T = 300 K were performed on a pendulum (the main magnetization curve) and induction (hysteresis loop) magnetometers. Fig. 3 shows the main magnetization curve and a part of the marginal hysteresis loop. The magnetization curve is observed

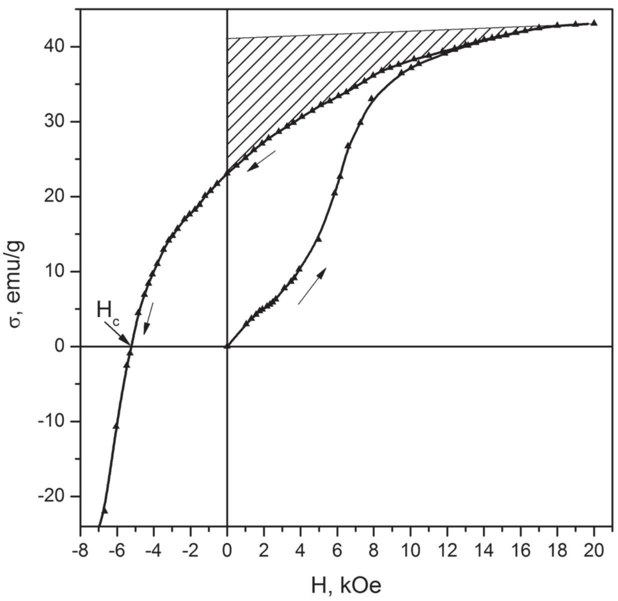

Fig.3. The dependence of the specific magnetization of the nanodispersed sample from the intensity of the magnetic field at 300 K.

typical for systems of small particles non-saturation of the magnetization in fields up to the anisotropy field of macroanalogue [10, 11]. Value of high-field magnetic susceptibility $\chi = 6\cdot10^{-4}$ emu·g^{-1}·Oe^{-1} is within values characteristic for fine ferrite systems (1-10 emu·g^{1}·Oe^{-1}) [12, 13].

The results of these measurements were the basis of determining the parameters of the effective magnetic anisotropy of the studied system of nanocrystals. For this purpose, five approaches was used: 1) a method based on the law of approach of magnetization to saturation (LAS) [6]; 2) the method of singular point on the magnetization curve (SPD) [14]; 3) "magnetization- area" method (MA) [15]; 4) a method based on the relationship between the magnetic anisotropy field and coercive force H$_c$ of the material [16] and 5) a method based on the field dependence of the remanence magnetization I$_r$ [7, 17].

The first two of these cases to determine the constant/field of magnetic anisotropy is directly use the main magnetization curve.

According to LAS, the magnetization can be written as

$$I(H)=\mathrm{I}_S\left(1-\frac{a}{H}-\frac{b}{H^2}-\dots\right), \qquad (1)$$

where: I_s- saturation magnetization, a- parameter of heterogeneity [18], $b=\frac{4}{15}\frac{K^2}{I_S^2}$, where $K=K_a^{ef}$ - constant of effective magnetic anisotropy or, in terms of the specific magnetization σ = *I*/ρ (ρ- density),

$$\sigma=\sigma_S\left(1-\frac{a}{H}-\frac{4}{15}\frac{K^2}{\rho^2\sigma_S^2}\frac{1}{H^2}-\dots\right). \qquad (2)$$

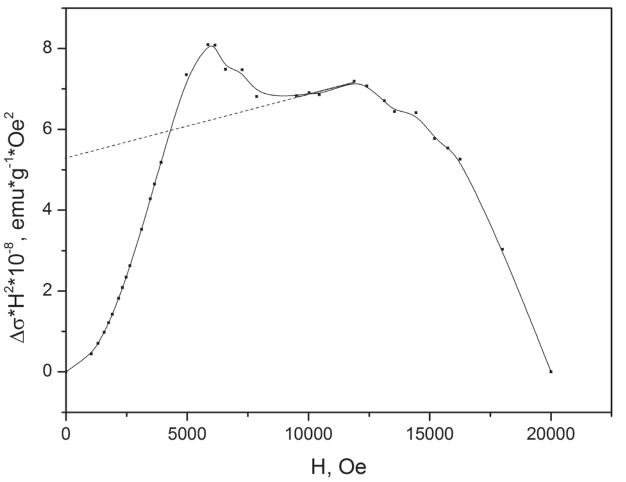

Fig.4. The magnetization curve constructed for calculationanisotropy constant with the law of approach to saturation using.

Dependence of *σ(H)* presented in the coordinates $(\sigma_S-\sigma)H^2=\Delta\sigma\cdot H^2=f(H)$ (Fig.4). Intercept on the y-axis with linear part of the dependence extrapolated to zero field,

$$l=\frac{4}{15}\frac{K^2}{\rho^2\sigma_S^2},$$

where

$$K=K_a^{ef}=1.936\rho\sqrt{\sigma_S l}\,. \qquad (3)$$

Field of the effective magnetic anisotropy of the ensemble of randomly oriented magnetically uniaxial particles can be determined by the following:

$$H_a^{ef}=\frac{2K^{ef}}{I_S}=3.872\sqrt{l/\sigma_S}\ \text{[16].} \qquad (4)$$

The method of singular point allows determining the anisotropy field of polycrystalline and powder samples by differentiating the magnetization curve. The position of the extremum on the curve of the second derivative of the magnetization on the field (Fig.5) corresponds to H_a^{ef} .

In [15] it is shown that for a system of randomly oriented magnetically uniaxial domains the area bounded by the demagnetization curve and by a straight line, that extrapolate the high-field part of the main curve to the field H=0 (Fig. 3, shaded area), that is,

$$\int_{I_r}^{I_S} H\,dI=\frac{2}{3}K \qquad (5)$$

Magnetization value obtained by extrapolation (I0) is the spontaneous magnetization. This creates the possibility to find a constant, and hence the effective magnetic anisotropy field of the studied system of single-domain magnetically uniaxial nanoparticles.

Anisotropy field of polycrystalline materials in the case of uniaxial anisotropy connected to the coercive force

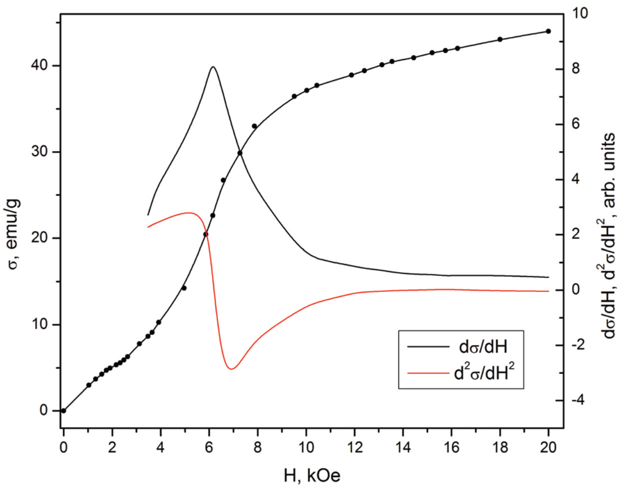

Fig.5. The field dependence of the specific magnetization and of its derivatives by field.

by correlation

$$H_C = 0.48 H_a \text{ [16].} \qquad (6)$$

Applying this formula to the powder sample with randomly oriented magnetically uniaxial particles allows finding H_a^{ef} by experimentally measured H_C.

The method developed in [7, 17], allows to obtain the distribution of the powder particles by anisotropy fields $f(H_a)$ by differentiation of field dependence of the remanence magnetization σ_r:

$$f(H_a) = \frac{dm_r(\text{H})}{dH}. \qquad (7)$$

Here $m_r = \sigma_r(H)/\sigma_r(\infty)$.

In Fig.6 is shown the $m_r(H)$ dependence and dependence of its derivative by field from the values of the field in percentage. Position of the peak on the curve $dm_r(H)/dH = f(H)$, because of its symmetrical shape, corresponds to the mean value of the anisotropy field of the particles system and, thereby, the effective magnetic anisotropy field.

Calculation results of the magnetic anisotropy parameters obtained by these methods are listed in the table.

As seen from the table, the constant K_a^{ef} for test sample of nanodispersive powder has the same order of magnitude as the magnetocrystalline anisotropy constant K_1 a of unsubstituted macroanalogue of barium ferrite [1] and a lower value, not only in comparison with macroanalogue, but also in comparison with a sample of the same degree of dispersion, for which $K_a^{ef} = 2.5 \cdot 10^6$ erg·cm⁻³ [4]. The received average value of K_a^{ef} is equal to (1.0 ± 0.2)·10⁶erg·cm⁻³. Closest to the average the value obtained by using the method of the "magnetization area" and value obtained from the experimentally measured value of the coercive force. Value $\langle H_a^{ef} \rangle = (9.4 \pm 2.0)$ kOe also less then for unsubstituted powder (16.3 kOe), due to the magnitude of the effective anisotropy constant.

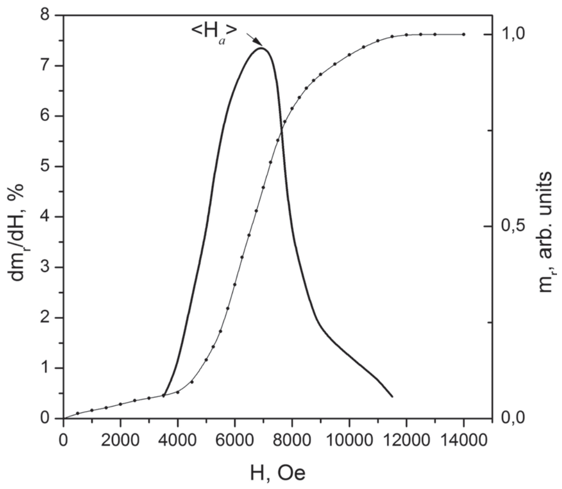

Fig.6. The dependence of the reduced remanence magnetization from the values of the field and the distribution of the powder particles by the fields of effective magnetic anisotropy.

The observed effects (at constant concentration of magnetic Fe^{3+} ions), apparently related to the structural distortions caused by difference of radius of Ca^{2+}(1.06Å) ions from Ba^{2+} ions (1.43Å) [19].

Authors are grateful to the staff of the laboratory of nanoscale powder materials, Belgorod State University (Russia) and to the staff of the laboratory of electron

Table 1

The parameters of the effective magnetic anisotropy of the nanosized ferrite of powder $Ca_{0.5}Ba_{0.5}Fe_{12}O_{19}$ obtained by different methods dmr/dH

	Method dm_r/dH	$K^{ef} \cdot 10^{-6}$, erg*cm⁻³	H_a^{ef}, kOe
1	LAS	1.5	13.8
2	SPD	0.8	7.0
3	MA	0.9	8.5
4	H_C	1.1	10.5
5		0.8	7.0

microscopy of V.N. Karazin Kharkiv National University for their participation in the synthesis and certification of samples.

1. J. Smit, H.Wijn. Ferrity, IL, M. (1962), 504 p.
2. G.S.Krinchik, A.P.Khrebtov, A.A.Askochenskii, V.E.Zubov. Pis`ma v ZHETF, **17**, 9, 466 (1973).
3. J.M.D.Coey. Phys.Rev.Lett., **27**, 1140 (1971).
4. Z.V.Golubenko, L.P.Ol'khovik, Yu.A.Popkov, Z.I.Sizova. Phys. of the Sol. State, **40**, 10, 1718 (1998).
5. A.Kamzin, B.Shtal, R.Gellert et al. FTT. **42**, V.5, 873 (2000).
6. N.S.Akulov. Z.Phys., **69**, 822 (1931).
7. H.Pfeiffer. Phys.Stat.Sol. (*a*), **118**, 295 (1990).
8. Iu.A.Mamalui, L.P.Ol`khovik. FTT, **24**, V.11, 3431 (1982).
9. S.V. Blazhevich, L.P. Ol`khovik et al. First international scientific conference «Nanostrukturnye materialy – 2008: Belarus – Russia – Ukraine», Minsk. – 2008. P. 472.
10. A.Morrish, K.Haneda. JMMM, **35**, 105 (1983).
11. K.Haneda. Can.J.Phys., **65**, 1233 (1987).
12. J.M.D.Coey. Can.J.Phys., **65**, 1210 (1987).
13. H.Kachakachi et.al. Eur.Phys.J, **B14**, 681 (2000).
14. G.Asti and S.Rinaldi. J.Apple.Phys., **45**, 8, 3600 (1974).
15. G.Hadjipanayis and D.J.Sellmyer. Phys.Rev.B, **23**, 7, 3349 (1981).
16. S.Krupichka. Fizika ferritov i rodstvennykh im magnitnykh okislov, T.2. MIR, M. (1976), 504 p.
17. H.Pfeiffer. Phys.Stat.Sol. (*a),* **139**, K129 (1993).
18. R.Grössinger. Phys.Stat.Sol. (*a*), **66**, 665 (1981).
19. Iu.Sitidze, Kh.Sato. Ferrity, MIR, M. (1964), 407 p.

Вісник ХНУ, № 1135, серія «Фізика», вип. 21, 2014. с. 49-51

УДК 536.7, 538.9

Investigation of pecularities of the structure formation for Fe-B-C system alloys in crystallization

S. B. Pilyaeva[1], N. Yu. Filonenko[2]

Oles Honchar Dnipropetrovsk National University[1]
Dnipropetrovsk State Medical Academy[2]
natph@mail.ru

Is show that in the iron-based alloys with weight content of boron from 1,8-3,5 % and with carbon content from 2-2,5 % (w.) after crystallization the morphology of specimen includes primary dendrites of $Fe_3(CB)$ phase and plate-like eutectics γ-Fe+$Fe_3(CB)$. It is revealed that in the process of Fe-B-C alloys crystallization the formation of cubic boron carbide $Fe_{23}(CB)_6$ takes place as a result of preannealing at the temperature of 1173 K. The formation of $Fe_{23}(CB)_6$ phase occurs on peritectic dissolving of Fe_2B boride, whereas eutectics $Fe_{23}(CB)_6$+γ-Fe is formed as a result of four-phase peritectic transformation $L+Fe_2B \rightarrow Fe_{23}(CB)_6$+γ-Fe.

Keywords: boride Fe_2B, eutectics , cubic boron carbide $Fe_{23}(CB)_6$ and Fe-B-C system alloy.

Показано, что в сплавах основе железа с содержанием бора 1,8-3,5 % (мас.) и углерода 2-2,5 % (мас.) после кристаллизации микроструктура состоит из первичных дендритов фазы $Fe_3(CB)$ и пластинчатой эвтектики γ-Fe+$Fe_3(CB)$. Установлено, что в процессах кристаллизации сплавов Fe-B-C образование кубического карбида $Fe_{23}(CB)_6$ происходит в результате предварительного отжига при температуре 1173 К. Выделение фазы $Fe_{23}(CB)_6$ осуществляется при перитектическом растворении борида Fe_2B, а формирование эвтектики $Fe_{23}(CB)_6$+γ-Fe происходит в результате четырехфазного перитектического превращения $L+Fe_2B \rightarrow Fe_{23}(CB)_6$+γ-Fe.

Ключевые слова: борид Fe_2B, эвтектика, кубический борокарбид $Fe_{23}(CB)_6$, система Fe-B-C.

Показано, що у сплавах на основі заліза з вмістом бору 1,8-3,5 % (мас.) та карбону 2-2,5 % (мас.) після кристалізації мікроструктура містить первинні дендрити фази $Fe_3(CB)$ та пластинчату евтектику γ-Fe+$Fe_3(CB)$. Встановлено, що процесі кристалізації сплавів Fe-B-C утворення кубічного борокарбіду $Fe_{23}(CB)_6$ відбувається в результаті відпалу при температурі 1173 К. Виділення фази $Fe_{23}(CB)_6$ здійснюється при перитектичному розчиненні борида Fe_2B, а формування евтектики $Fe_{23}(CB)_6$+γ-Fe відбувається в результаті четирьохфазного перитектичного перетворення $L+Fe_2B \rightarrow Fe_{23}(CB)_6$+γ-Fe.

Ключові слова: борид Fe_2B, евтектика, кубічний борокрбід $Fe_{23}(CB)_6$, система Fe-B-C.

Introduction

It is well known, that Fe-B-C system alloys are of practical use because of complex of such properties as refractory quality, high hardness, abrasive wear resistance, chemical stability in various aggressive environments and others [1-3]. Available information about phase transitions in Fe-Fe_2B-Fe_3C composition triangle of Fe-B-C system alloys in the process of crystallization from a liquid state goes to prove that equilibrium phases are iron solid solution, boride Fe_2B and boron cementite $Fe_3(CB)$. $Fe_{23}(CB)_6$ compound, which is isomorphic with carbide $Cr_{23}C_6$, for the first time has been described in Ref. [4] as congruently melting phase. According to Refs. [5, 6] phase $Fe_{23}(CB)_6$ exists in a solid state and is not stable at the temperatures above 1230 K. In the paper [7] it was shown that at high degree of supercooling the precipitate of this compound is possible. In Ref. [8] it is ascertained that precipitate of cubic boron carbide $Fe_{23}(CB)_6$ in the process of crystallization from a liquid state takes place after a special pretreatment, which includes thermal cycling in a solid-liquid state for at least 5-6 cycles within the temperature interval of 1123-1613 K, but mechanism of formation of cubic boron carbide $Fe_{23}(CB)_6$ in Fe-B-C alloys is not revealed.

In this paper the investigation of crystallization of alloys of Fe-Fe_2B-Fe_3C composition triangle with preannealing in solid state is carried out and mechanism of formation of cubic boron carbide $Fe_{23}(CB)_6$ is studied.

Materials and methods of investigation

For investigation there are used alloys with weight content of boron from 1,8-3,5 % and with carbon content from 2-2,5 % (w.), the rest is iron. To obtain Fe-B-C alloys we use carbonyl iron (with iron content of 99,95% (w.)), amorphous boron (with boron content of 97,5,0% (w.)) and spectroscopically pure graphite. To prevent a liquation alloys were made from previously well-stirred and pressed powder of furnace burden materials. The specimen smelting was carried out in Taman’s furnace with graphite heater, melting of specimens was performed in alundum saggers under argon atmosphere. The cooling rate of initial

a *b* *c*

Fig. 1. Microstructure of Fe-B-C alloy with boron content of 2,95 % (w.), carbon content of 2,3 % (w.): a) after smelting x400, b) after pretreatment x100, c) eutectics γ-Fe+ $Fe_{23}(CB)_6$.

specimens of alloys was 50 K/s. To determine alloy chemistry chemical and spectrographic analysis was used [10]. To study physical properties of obtained alloys durometric analysis was used (by means of microhardness tester PMT-3). The phase composition of alloys was determined by X-ray microanalysis method by means of JSM-6490 microscope, as well as by means of optical microscope "Neophot-21". X-ray phase analysis was performed by means of diffractometer DRON-3 in monochromatic Fe-Kα radiation for voltage U=35 kV and anode current I=14 mA. The types and temperatures of phase transformations were determined by differential thermal analysis method using a derivatograph. The precision of measurement is of ±5. The study of hardening process was carried out for the case of iron-carbon specimens, part of which was preannealed at the temperatures of 1123-1173 K. Degree of superheat while melting of alloys specimens is no more than 30 K above liquidus curve. Heating and cooling rate is of 30-40 K/min.

Results and discussion

Fig. 1 presents the microstructure of initial Fe-B-C system alloy.

The morphology of specimen includes primary light-coloured dendrites of $Fe_3(CB)$ phase and plate-like eutectics γ-Fe+$Fe_3(CB)$ (Fig. 1, a). According to results of X-ray structure analysis in diffractograms of alloy there are curves of cubic boron carbide $Fe_{23}(CB)_6$, but in the process of microstructure investigation this phase is not revealed (Fig. 2, b). The thermogram of such an alloy is shown in Fig. 2, a. The thermal effect, which was observed at the temperatures of 1408-1410 K, corresponds to precipitate of dendrites of boron cementite $Fe_3(CB)$. The eutectic constituent γ-Fe+$Fe_3(CB)$ is formed within the temperature interval of 1401-1385 K. At the temperature of 960 K the formation of austenite takes place.

In Fig. 1, b there is presented the microstructure of alloy, which after melting had been preannealed at the temperature of 1170 K for an hour, and then had been heated up to temperature 30 K above liquidus, and then was cooled with a rate 40 K/min. The X-ray structure analysis of this alloy shows presence of the curves, peculiar to boride Fe_2B, boron carbide $Fe_{23}(CB)_6$ and iron α-solution, in diffractograms of alloy (Fig. 3, b). Microstructure of alloy consists of primary borides Fe_2B, which are situated inside the large edged crystals of $Fe_{23}(CB)_6$ phase and finely-divided eutectics γ-Fe+$Fe_{23}(CB)_6$ with a core morphology (Fig. 1, b, c). The thermogram of this alloy is shown in Fig. 3, a.

The precipitates of primary borides take place

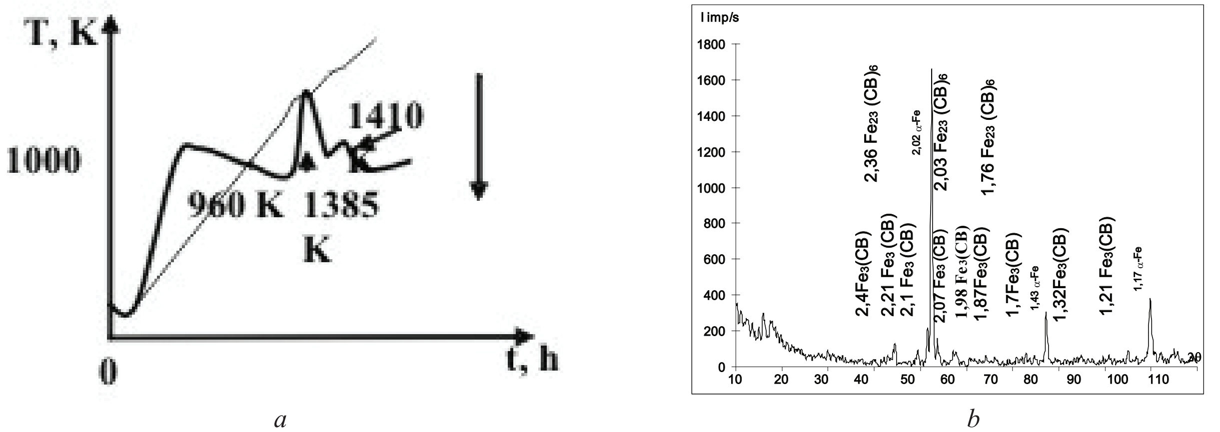

a *b*

Fig. 2. Fe-B-C system alloy with boron content of 2,95 % (w.), carbon content of 2,3 % (w.) without preannealing: a) differential thermogram, b) diffractogram

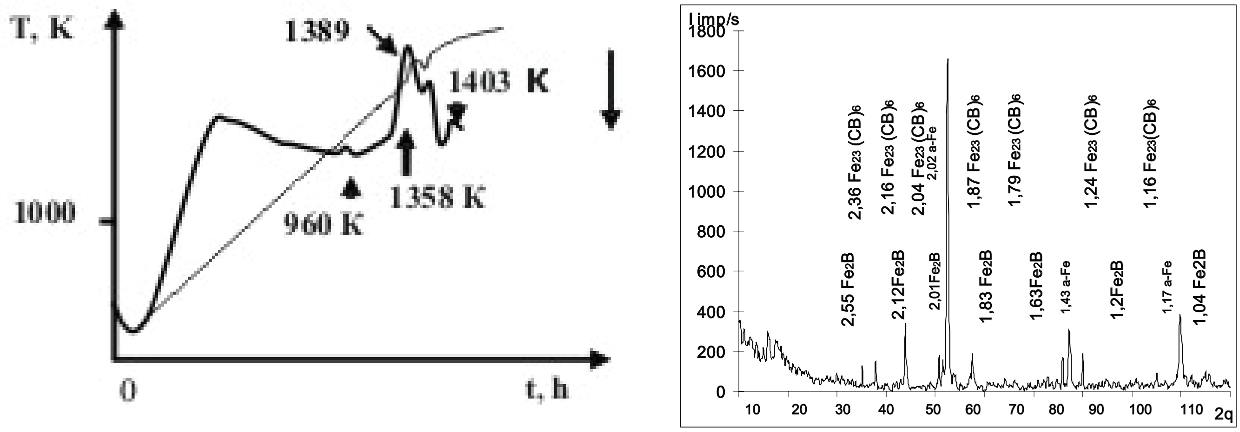

a *b*

Fig. 3. Fe-B-C system alloy with boron content of 2,95 % (w.), carbon content of 2,3 % (w.) after preannealing: a) differential thermogram, b) diffractogram.

within the temperature interval of 1403-1358 K. At the temperature of 1358 K the peritectic dissolution of Fe_2B boride and formation of boron carbide $Fe_{23}(CB)_6$, which takes place within the temperature interval of 1358-1389 K, begins. At the temperature of 1389 K the four-phase transformation $L+Fe_2B \rightarrow Fe_{23}(CB)_6+\gamma$-Fe occurs. As a result of peritectic dissolution of Fe_2B phase the eutectic constituent $Fe_{23}(CB)_6+\gamma$-Fe with fine differentiation is forming (Fig. 1, c). As ground of this one can considered the occurrence of precipitates of Fe_2B phase crystals not only inside the crystals of $Fe_{23}(CB)_6$ phase, but also in surroundings of eutectics $Fe_{23}(CB)_6+\gamma$-Fe. In alloys with boron weight content of 2,4-1,95 % and carbon content of 2-2,4 % without pretreatment in the process of melting and crystallization primary dendrites γ-Fe and plate-like eutectics γ-Fe+$Fe_3(CB)$ are formed. After preannealing in alloys with boron content of 2,4-1,95 % and carbon content of 2-2,4 % at the temperature of 1389 K the eutectic structure with a core morphology $Fe_{23}(CB)_6+\gamma$-Fe is forming. The formation of structures, which include the precipitates of $Fe_{23}(CB)_6$ phase, is associated with their previous formation in a solid state while preannealing. According to results of Ref. [9] the formation of $Fe_{23}(CB)_6$ phase in the process of annealing is described by reaction γ-Fe+ $Fe_3(CB) \rightarrow Fe_{23}(CB)_6$ and occurs on interphase boundaries of eutectics γ-Fe+ $Fe_3(CB)$. The analysis of obtained results enables to suppose, that postheating up to melting point and short-term holding at the temperature 30 K above liquidus is followed by formation of complex aggregates, close in composition to $Fe_{23}(CB)_6$ phase composition, in melt. In such a case the preparation of the rest of melt regions with boron atoms takes place. The aftercooling leads to precipitate of primary crystals of Fe_2B boride and $Fe_{23}(CB)_6$ phase as resultant of peritectic reaction $L+Fe_2B \rightarrow Fe_{23}(CB)_6$

Conclusions

1. The formation of cubic boron carbide $Fe_{23}(CB)_6$ in Fe-B-C alloy from liquid state is contingent on preheating up to temperatures of its formation in solid state and coming from existence of its stability range in solid state.
2. The formation of $Fe_{23}(CB)_6$ phase occurs on peritectic dissolving of Fe_2B boride, whereas eutectics $Fe_{23}(CB)_6+\gamma$-Fe is formed as a result of four-phase peritectic transformation $L+Fe_2B \rightarrow Fe_{23}(CB)_6+\gamma$-Fe.

1. N. P. Lyakishev, Yu. L. Pliner, S. I. Lappo. Boron-bearing steels and alloys. Moscow: Metallurgy, 1986. –191 p. (in Russian).
2. Yu. B. Kuzma, P. F. Chaban. Boron-bearing binary and ternary systems. Handbook. Moscow: Metallurgy, 1990. –320 p. (in Russian).
3. G. V. Samsonov, T. I. Serebryakova, V. A. Neronov. Borides. //Moscow: Atomizdat. 1999. – 220 p. (in Russian).
4. Stadelmaier H.H., Gregy R.A. // Metall. vol. 5. – P. 412-422, 1963.
5. Koneko J.H., Nichizawa T., Chiba, Nippon Kinzoku Gakkaishi, vol. 30. , 1966. – P. 263-272.
6. Schiirmann, Li Shao-Xiong // Giesserei-forschung, t. 37. №4, 1985. – P. 121-129.
7. Fomichev O. I. , Katkov V. F. Stability range of ternary phase τ in Fe-B-C system // Izv. Vuz. Chernaya metallurgia, №1, 1988. – P. 101-103 (in Russian).
8. Pilyaeva S. B., Bezrukavaya O. G., Butenko V. F. Pecularities of $Fe_{23}(CB)_6$ compound formation in Fe-B-C alloys // Visnyk Dnipropetrovskoho universytetu. Fizyka. Radioelectronika, Issue 4. 1998. – P. 23-26 (in Russian).
9. Spiridonova I. M. , Pilyaeva S. B. , Butenko V. F. Investigation of the phase stability in isothermal annealing // The matter of formation of metastable of alloys structure. Interuniversity collection of research papers. Dnipropetrovsk, 1984. – P. 155-162 (in Russian).
10. S. B. Tverdokhlebova, I. M. Spiridonova, A. M. Bondarenko. Spectrographic analysis of boron-bearing alloys // Zavodskaya laboratoriya. №11, 1990. – P. 46-49 (in Russian).

Вісник ХНУ, № 1135, серія «Фізика», вип. 21, 2014. с. 52-55

УДК 539.3:538.9
PACS 83.50.-v Deformation and flow
61.80.x Physical radiation effects, radiation damage

Continuous electron irradiation effect on plastic deformation of the steel T91 at different temperatures

S.V. Lebedev[1], A.P. Nazipova[1], V.I. Dubinko[2],
I.V. Khodak[2], V.A. Kushnir[2], D. Terentyev[3]

[1]V.N. KarazinKharkovNationalUniversity, Kharkov61022, Ukraine
[2]National Science Center "Kharkov Institute of Physics and Technology", Kharkov 61108, Ukraine
[3]SCK•CEN, Nuclear Materials Science Institute, Boeretang 200, Mol, 2400, Belgium

There was studied the deformation of the steel T91 exposed to electron irradiation at different temperatures. The deformation strength decreasing and the hardening ratio as function of relative elongation were defined in continuous irradiation mode. It was established the increasing of the steel plasticity as the result of the electron beam exposition.

Keywords: electron irradiation, yield stress, plastic deformation, hardening ratio, temperature dependence.

Вивчена деформація сталі Т91 під впливом електронного опромінення при різних температурах. У режимі безперервного опромінення визначено зниження рівня деформуючої напруги, коефіцієнт зміцнення як функцію відносного видовження. Встановлено зростання пластичності металу в результаті впливу електронного пучка.

Ключові слова: електронне опромінення, межа плинності, пластична деформація, коефіцієнт зміцнення, температурна залежність.

Изучена деформация стали Т91 под воздействием электронного облучения при различных температурах. В режиме непрерывного облучения определено снижение уровня деформирующего напряжения, коэффициент упрочнения как функцию относительного удлинения. Установлено возрастание пластичности металла в результате воздействия электронного пучка.

Ключевые слова: электронное облучение, предел текучести, пластическая деформация, коэффициент упрочнения, температурная зависимость.

Introduction

It's well known that plastic deformation or flow of metals and alloys, and strain hardening as well is observed in the full temperature range beginning from low (helium) values and up to pre-melting ones. This effect is induced by moving of dislocations and their interactions with structural and impurity defects of a crystal lattice. In some cases, interactions of moving dislocations with phonons, conductivity electrons and others [1] should be taken into account as well.

Dislocations while moving dissipate energy on conductivity electrons. This fact was established experimentally in changing from room-temperature sate to superconductivity [2]. Kinetics of dislocations is varied also in hard magnetic field [3], under exposition to electron and gamma irradiation [4] and to high current density electric pulses [5]. The term 'electro-plastic deformation of a material' was introduced for these effects [5].

The research purposed to investigate deformation of some hexagonal close-packed (HCP) crystals exposed to short electron beam pulses that have been done in the early 1960s allowed to demonstrate the step-down change of a deforming strength and increasing of plasticity [4].

The plastic flow of metals with FCC crystal lattice (Al, Cu) exposed to electron beam has been researched in the paper [6]. There were studied dependencies of strength loss, deformation ratio, the thickness of a sample and others [6].

However, steel has BCC crystal lattice, and the effect of its exposition to electron irradiation should be researched. The steel T91 is a constructive material of nuclear reactors. To understand its strength performances dependent on temperature and electron irradiation and to obtain data for analysis and defining of control methods of radiation-induced effect the research including the simulation of in reactor environment processes should be fulfilled.

Experimental technique

Polycrystalline samples of the steel T91 were researched. Its alloying constituents are summarized in the table 1. The samples were profile cut from sheets of 15 mm thickness after hot rolling. The rolling and the cooling was realized by following sequence: normalization at 1050°C during 15 min, water hardening down to room temperature, exposure at 770°C during 45 min and air cooling down to room temperature. Samples have active narrow region with dimensions of 1.9×0.75×30 mm between two broad regions for grips of a deformation machine.

The researched samples were divided into two sets. The first set was researched without the next processing. The second set was annealed at 650°C in argon environment during 3 hours with next cooling together with a kiln down to room temperature.

The plot of the sample loading was registered in load (P) – time (t) diagram with time resolution 0.3 sec (storage digital multimeter Sanwa PC-520M) and the load sensitivity 0.5 H. After registration the load was converted into deforming strength according to the ratio $\sigma=P(1+\varepsilon)/S$ (S is initial cross-section of a sample, ε is relative elongation of a sample). For uniform movement of the rod in the fracturing machine the relative deformation was defined as following $\varepsilon=\upsilon_{rod}\cdot t/L$ ($\upsilon_{rod}=5$ μm·sec^{-1} – velocity of a rod movement, L – initial length of the active region of a sample)with error ±0.1%.

During the deformation, the samples of steel T91 were exposed to electron irradiation according to the method explained before [7]. Consider only parameters and time structure of the electron beam. The electron beam with energy E=0.8 MeV and electron flux density through the sample $(1.9\ldots4.0)\cdot10^{16}$ m^{-2}·s^{-1}(irradiation power ~3 W) from the 'Resonance' linac [7] directed on the active region of the sample. Electrons had uniform distribution on area ~5…6 mm^2. Microbunches of electrons with duration τ_{mb}= $4\cdot10^{-11}$ sfed the beam with frequency $3\cdot10^9$ GHz in a bunch with duration $\tau_b=(1.8\ldots2)\cdot10^{-6}$ s. The bunch repetition rate $1/T_0$ was 25 Hz.

During the deformation the sample was mounted in a heater that allowed its heating in the range 313-673 K. The temperature variation of the sample due to external or by electron irradiation heating was measured using Cu-Constantan thermocouple. The accuracy of the temperature measurements ΔT was ±1 K.

To achieve the temperature below 273 K the sample was placed in a cryostat in a liquid nitrogen steam and was heating up so that the temperature may be varied in the range 193…273 K.

Experimental results

The effect of high-energy electron beam on plastic flow of Al at room temperature in the cycle-change deformation mode (with period ~50…100 s) under electron irradiation (φ≠0) or its absence (φ=0) (continuous [8] and differential irradiation mode [6]) was considered before.

There was shown in the paper [8] that electron beam effects on decreasing of deforming strength σ and increasing of a sample elongation ε. Such variations on the deforming diagram σ(ε) of the metal may indicate the genesis of less strength structural state under high energy electron flux.

Figure 1 shows curves of deformed strengthening σ(ε) (σ is deforming strength, ε is relative elongation) of the steel T91 samples under electron irradiation (2, 4 - φ≠0) and on its absence (1, 3 - φ=0).

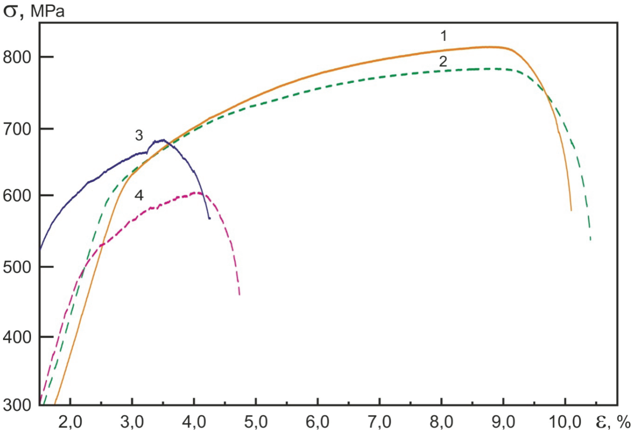

Fig. 1. Deformation curve for reactor steel T91 (EUROFER) without irradiation (1, 3) and at φ = $4.0\cdot10^{16}$ m^{-2}·s^{-1} (2); $1.9\cdot10^{16}$ m^{-2}·s^{-1} (4) at RT (1, 2) and at 553 K (3, 4).

Due to continuous mode of electron irradiation, the deforming strength value is decreased in the total range of deformations starting from yield stress and up to the sample breakdown, and the plasticity resource of the metal is increased.

Mean free path of 0.8 MeV electrons in the steel is ~2.0 mm (Fig. 2). Therefore, electrons of the irradiating beam penetrated through the steel.

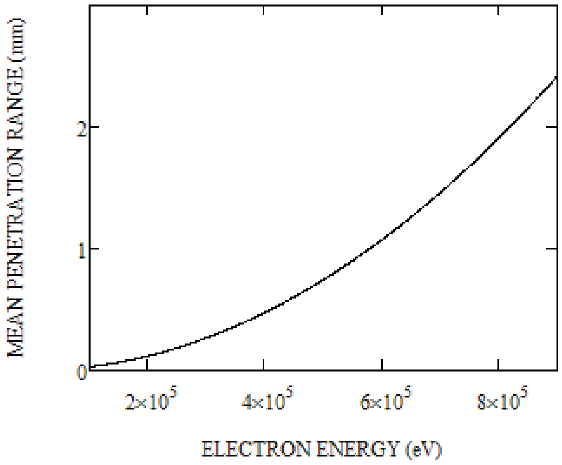

Fig. 2. Calculated mean free electron path vs irradiation energy for iron.

The steel samples were tension deformed at different temperatures: in liquid nitrogen steam, at room temperature and at increased temperature 350-600°K evaluated by external heater. Figure 3 shows the obtained dependences of yield stress (Fig. 3 a), ultimate strength (Fig. 3 b) and the plasticity resource (Fig. 3 c). With the temperature increasing all samples both annealed and non-annealed have decreased yield stress, the ultimate strength decreased in 1.5 times and the relative elongation decreased in 2.5 times.

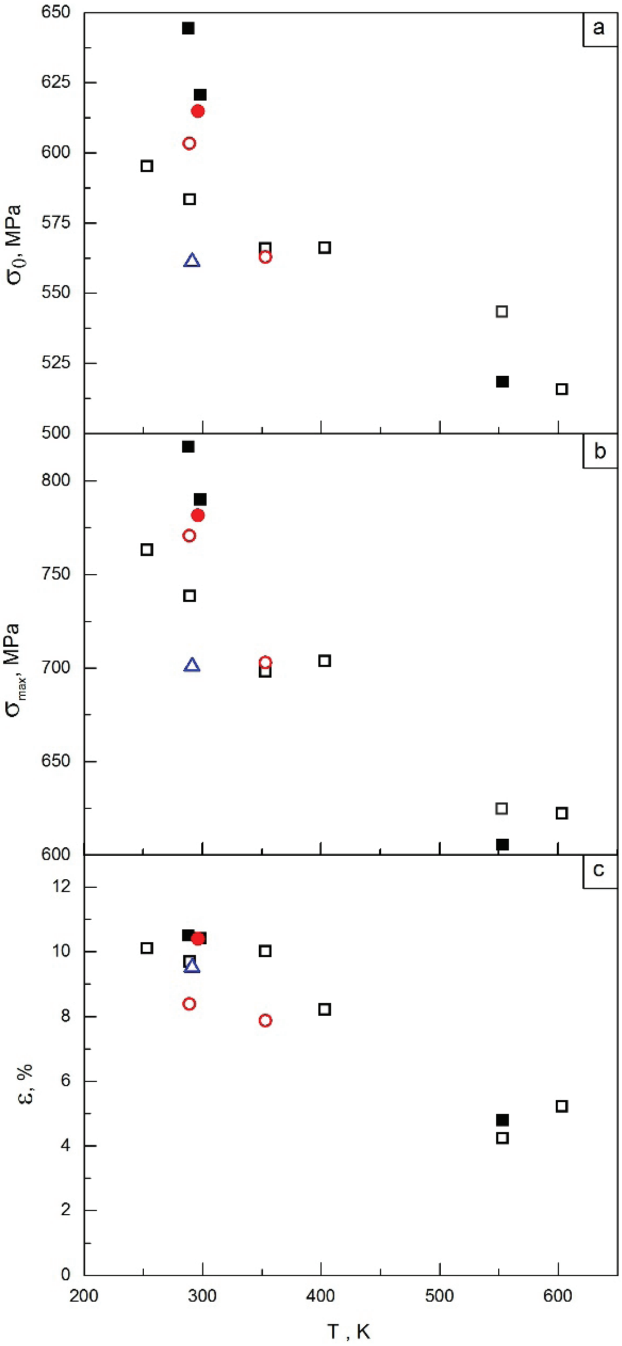

Fig. 3. Strength and plastic performances of the steel T91 samples: yield stress σ_0(a), ultimate strength σ_{max}(b) and plasticity resource ε_{pl}(c); hollow symbols – non-annealed samples, solid symbols - annealed samples.

□ - annealed samples, deformation velocity $5 \cdot 10^{-5}$cm/s;

△ - annealed sample, deformation velocity $5 \cdot 10^{-6}$cm/s;

○ - non-annealed samples, deformation velocity $5 \cdot 10^{-5}$cm/s.

Let’s treat the effect of high energy electrons on the steel T91 samples at different temperatures. As one can see from the Fig. 3 the decreasing of the yield stress, the ultimate strength and the relative elongation is observed for the temperature increasing. Comparing annealed and non-annealed sample for the temperature 553°K it is observed the decreasing of the ultimate strength (Fig. 3 b) but the increasing of the plasticity resource on 13 % (Fig. 3 c) at the same time.

The electron irradiation effect on the sample heating up was studied next. At room temperature without external heater, the sample temperature rises on 7°C under electron irradiation that is compared with environment temperature. It means that electron irradiation effects on the sample heating negligibly due to the sample thickness is smaller than the free electron path. It permits to exclude a temperature component action on dislocation movement in a crystal lattice. In the context of this fact, it should be interesting to consider the effect of both the temperature corresponding to the values the steel T91 is under in nuclear reactors and continuous mode electron irradiation of the sample during its tension deformation.

Because of nuclear reactors are featured by high temperature and irradiation it was necessary to test the steel samples both under external heating up and electron irradiation. The samples were exposed to continues electron irradiation in presence and absence of the external heater.

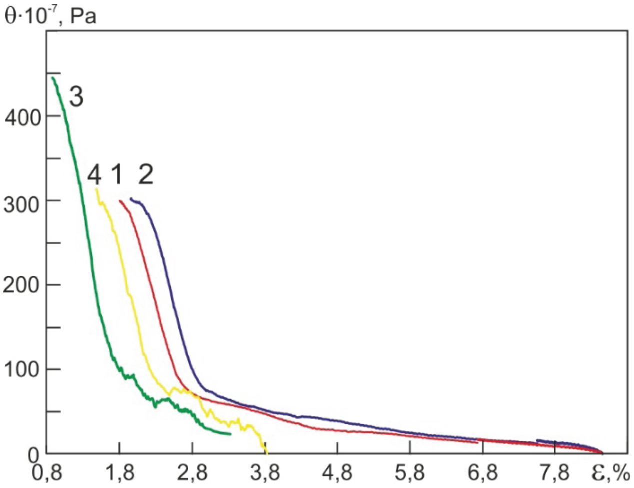

Fig. 4. Deformation strengthening ratio of the steel T91 vs relative elongation ratio in coordinates θ(ε) (1, 3–φ=0; 2, 4 –φ≠0; 1, 2 – deformation at 553 K; 3, 4 - deformation at 291 K).

As one can see from the Fig. 4 there is the difference in 1 and 2 deformation phases for equal temperatures (room and increased values) while the ratio is equal in fact in the deformation phase 3. Comparing irradiated and

Table 1.

The chemical composition of the alloy

Alloy	Mass fraction of element, %																
	C	N	Al	Si	P	S	Ti	V	Cr	Mn	Ni	Cu	As	Nb	Mo	Sn	W
T91	0.10	0.0442	0.015	0.22	0.021	0.0004	0.003	0.21	8.99	0.38	0.11	0.06	0.008	0.06	0.89	0.004	0.01

non-irradiated steel T91 samples while their deformation under exposition to high-energy electron beam there is no the difference in the deformation strengthening ratio. This means that electron irradiation does not effect on the steel deformation. The deformation the strengthening ratio is decreased on $100 \cdot 10^{-7}$ Pa in case of the temperature values similar to nuclear reactor environment. This shows both the sample softening and increasing of its plasticity under electron flux effect on crystal lattice.

Conclusion

The strength performances depending on temperature have been obtained. The yield stress, the ultimate strength and the plasticity resource is decreased for the temperature increasing.

There is the increasing of the plasticity resource and decreasing of the ultimate strength simultaneously while the samples are deformed under electron irradiation at equal temperature values. These points to the effect of electron flux on dislocation structure of the steel T91.

1. V.I. Starcev, V.Ya. Ilichev, V.V. Pustalov. Plasticity and strength of metals and alloys at low temperatures. M: “Metallurgy”, 1975, p. 328 (in Russian).
2. M.I. Kaganov, V.Ya. Kravchenko, V.D. Natsik. Electronic stopping of dislocations in metals //.UFN. 1973 v. 111, №1, p. 655-682 (in Russian).
3. V.P. Lebedev, V.S. Krylovskiy. Effect of magnetic field on the formation of defect structure during low-temperature deformation of aluminum // JETP Letters. 1982, v. P6 n. 1, p. 3-5 (in Russian).
4. O.A. Troitskii, V.I. Lihtman. The anisotropy of the action of the electron and γ-irradiation on the process of deformation of in zinc monocrystals in a fragile state // Dokl. USSR Academy of Sciences. 1963 v. 148, №2, p. 332-334 (in Russian).
5. V.I. Spitsin, O.A. Troitskii. Investigation of electron impact on the plastic deformation of metals // Metallofizika. Kiev: “Naukova Dumka”, 1974, c. 51, p. 18-45 (in Russian).
6. V.I. Dubinko, A.N. Dovbnya, V.A. Kushnir, V.V. Mitrochenko, I.V. Khodak, V.P. Lebedev, V.S. Krylovskii, S.V. Lebedev, V.F. Klepikov. Effect of high-energy electron beam irradiation on plastic deformation of metals // Problems of Atomic Science and Technology. A series of “nuclear physics research”. 2010, №3, p. 136-139 (in Russian).
7. N.I. Ayzatskii, A.N. Dovbnya, V.I. Dubinko, V.F. Zhiglo, A.I. Kosoy, V.A. Kushnir, V.V. Mitrochenko, S.A. Perezhogin, D.L. Stepin, I.V. Khodak, V.P. Lebedev, V.S. Krylovskii, S.V. Lebedev. The facility for the research of electron flux effect on deformation of metals // Problems of Atomic Science and Technology. A seriesof “nuclear physics research”. 2010, №3, p. 145-149 (in Russian).
8. V.I. Dubinko, A.N. Dovbnya, V.A. Kushnir, V.V. Mitrochenko, I.V. Khodak, V.P. Lebedev, V.S. Krylovskiy, S.V. Lebedev, V.F. Klepikov. Plastic deformation of aluminum under continuous electron irradiation // Problems of Atomic Science and Technology. A series of “nuclear physics research”. 2010, №5, p. 43-49 (in Russian).

Вісник ХНУ, № 1135, серія «Фізика», вип. 21, 2014. с. 56-60

PACS: 66.30.J-; 66.30.-h
УДК: 53.01; 538.931

Microscopic model for the Langevin equation: Force-force correlation function

G.M. Pritula*, A.V. Shkop**, D.A. Tkanov**, O.V. Usatenko*

*A. Ya. Usikov Institute for Radiophysics and Electronics, Ukrainian Academy of Science,
12 Proskura Street, 61085 Kharkov, Ukraine
**V. N. Karazin Kharkiv National University, 4 Svobody Sq/, 61077, Kharkov, Ukraine
pritula.galina@gmail.com

We look into the particle diffusion in a 1D atomic chain. We consider two different models. In the first one the lattice particles are supposed to move independently. The stochasticity of the motion in this case is achieved due to nonlinear oscillations of the lattice particles. In the second case the linear oscillations of the lattice particles are considered and the stochasticity of doping particle motion stems from the finiteness of phonon spectra. In both cases we derive the stochastic properties of the Langevin force. The found expressions for the correlation function of the Langevin force could be reduced to the white noise only at some limiting values of the lattice and thermostat parameters.

Keywords: diffusion, Langevin force, correlation function, microscopic theory.

У статті досліджується дифузія частинки в 1D ланцюжці атомів. Розглядаються дві різні моделі. У першій моделі передбачається, що частинки решітки рухаються незалежно одна від одної. Стохастичність руху в цьому випадку досягається за рахунок нелінійних коливань частинок решітки. У другому випадку розглядаються лінійні коливання частинок решітки і стохастичність руху частинки домішки пов'язана з обмеженністю фононних спектрів. В обох випадках досліджені стохастичні властивості сили Ланжевена. Знайдені вирази для кореляційної функції сили Ланжевена можуть бути зведені до білого шуму лише при деяких граничних значеннях параметрів решітки та термостата.

Ключові слова: дифузія, сила Ланжевена, кореляційна функція, мікроскопічна теорія.

В статье исследуется диффузия частицы в 1D цепочке атомов. Рассматриваются две различные модели. В первой модели предполагается, что частицы решетки движутся независимо друг от друга. Стохастичность движения в этом случае достигается за счет нелинейных колебаний частиц решетки. Во втором случае рассматриваются линейные колебания частиц решетки и стохастичность движения примесной частицы связана с конечностью фононных спектров. В обоих случаях изучены стохастические свойства силы Ланжевена. Найденные выражения для корреляционной функции силы Ланжевена могут быть сведены к белому шуму только при некоторых предельных значениях параметров решетки и термостата.

Ключевые слова: диффузия, сила Ланжевена, корреляционная функция, микроскопическая теория.

Introduction

The diffusion properties of Brownian particles continues to be of enormous interest even though a century has passed since the appearance of the famous work of Einstein on the subject [1].

A central point of Einstein's work is the insight that within the complicated many-body system, a time-scale separation exists between the particles slow center of mass and a huge number of remaining fast molecular degrees of freedom. In statistical physics the stochastic Langevin equation is often used to describe this 'slow' motion. The fast (microscopic) variables are responsible for the stochastic nature of the Langevin equation. This approach finds many applications in different branches of physics. For example, the Langevin equations are used in the statistical mechanical treatment of time-dependent phenomena in fluids [2], to describe nuclei fission and fusion [3], and in other areas of science [4].

The common model of random forces used in the Langevin approach, the so-called Langevin forces, is white noise. As a matter of fact, this phenomenological approximation imposes restrictions on the formulation of problems which could be solved by means of this model. On the other hand, the microscopic theory of statistical properties of Langevin forces highlights some new information about the stochastic nature of the Langevin model.

In this paper we look into the doping particle diffusion in a 1D chain of atoms. We consider two different models. In the first one, (Sec.2), the lattice particles are supposed to move independently. The stochasticity of the motion in this case is achieved due to nonlinear oscillations of the lattice particles.

In the second case, (Sec.3), the linear oscillations of the lattice particles are considered and the stochasticity of doping particle motion stems from the finiteness of phonon spectra. In both cases we derive the stochastic properties of the Langevin force. It is interesting to note that the found expressions for the correlation function of the Langevin force could be reduced to the white noise only at some limiting parameter values.

Model of non-linear oscillations

a. Formulation of problem

Let us consider a particle of mass m moving in a field of 1D diatomic lattice of particles of masses M, a distance between the lattice sites is l, equilibrium positions of lattice atoms in (q,Q) plane are $(kl,\pm\overline{Q})$, $k=\ldots-1,0,1,\ldots$ (see Fig. 1). Let us introduce Q_k which stands for deviation of the k-th particle from its equilibrium position. To simplify the problem we consider only anti-phase oscillations of the nearest atoms as shown in Fig. 1. q is the coordinate of the foreign diffusion particle.

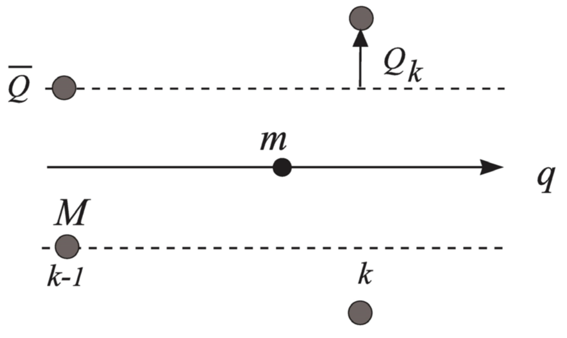

Fig. 1. The model of 1D diatomic lattice with transversal displacements.

Hamiltonian of such system in the absence of interaction between the lattice particles is given as

$$H=\frac{p^2}{2m}+\sum_k\left[\frac{P_k^2}{2M}+U(Q_k)\right]+ \\ +\sum_k U_{int}\left(q-kl,\overline{Q}+Q_k\right). \tag{1}$$

Expansion of the non-linear potential of anti-phase oscillations $U(Q_k)$ in the Taylor series up to the fourth order near the equilibrium position of the particles reads

$$U(Q)=M\left(\frac{\omega_0^2Q^2}{2}+\frac{\alpha Q^3}{3}+\frac{\beta Q^4}{4}\right). \tag{2}$$

b. Equations of motion for impurity particle

Expanding the potential of interaction between the doping particle and the lattice particles into series we obtain

$$U_{int}\approx U_{int}\big|_{Q_k=0}+\frac{\partial U_{int}}{\partial Q_k}\Big|_{Q_k=0}Q_k. \tag{3}$$

The equation of motion for the particle takes the form

$$m\ddot{q}=-\sum_k\frac{\partial U_{int}}{\partial q}\Big|_{Q_k=0}-\sum_k\frac{\partial^2U_{int}}{\partial q\partial Q_k}\Big|_{Q_k=0}Q_k. \tag{4}$$

This equation can be solved by using the solution of the equations of motion for the lattice particles:

$$\ddot{Q}_k=\omega_0^2Q_k-\alpha Q_k^2-\beta Q_k^3+f_k(q(t)), \\ f_k(q(t))=-\frac{\partial U_{int}}{\partial Q_k}\Big|_{Q_k=0}. \tag{5}$$

So we arrive at the point where we have to solve the equations of motion for the lattice particles to find a solution of the equation of motion for the doping particle.

An approximate solution of Eq. (5) can be easily found, for example, with the use of the two time scale method, see e.g. [5]. We omit this procedure and present the following solution,

$$Q_k(t)=\left(Q_{k0}+I_k(t)\right)\cos\left(\Omega_k(t-t_0)+\varphi_k\right), \\ I_k(t)=\frac{1}{\omega_0}\int_{t_0}^{t}dt'f(q(t'))\sin\left(\Omega_k(t'-t_0)+\varphi_k\right), \tag{6}$$

$$\Omega_k=\omega_0+\left(\frac{3\beta}{8\omega_0}-\frac{5\alpha^2}{12\omega_0^3}\right)|Q_{k0}|^2, \tag{7}$$

where φ_k is the initial phase of the k-th particle, Q_{k0} is its initial displacement.

Considering the last term in Eq. (4), we substitute Q_k by the corresponding expression from Eq.(6):

$$\sum_k\Phi_k(q)\left(Q_{k0}+I_k(t)\right)\cos\left(\Omega_k(t-t_0)+\varphi_k\right), \tag{8}$$

where $\Phi_k(q)=\frac{\partial^2U_{int}}{\partial q\partial Q_k}\Big|_{Q_k=0}$.

This expression contains two totally different terms. The first one is the so-called Langevin force, stochastic force applied to the q-th particle; the second one is the friction force.

c. Langevin force

Consider the Langevin force:

$$F_L(q,t)=\sum_k\Phi_k(q)Q_{k0}\cos\left(\Omega_k(t-t_0)+\varphi_k\right). \tag{9}$$

Parameters Q_{k0} and φ_k are independent random variables. The first one determines the energy of the k-th particle at the moment t_0 and the second one defines the phase of oscillations at the same moment. Also, we suppose that the system under study is in thermal equilibrium at temperature T.

Evidently, the average value of the Langevin force $\langle F_L \rangle$ equals zero. Indeed, Q_{k0} and φ_k are independent variables, so their averaging should be performed separately. The value of φ_k is distributed uniformly in the interval $0 \leqslant \varphi_k \leqslant 2\pi$. Now, the initial statement is obvious.

Pair correlation functions give a lot of information for describing a variety of physical processes. Some applications of physical system analysis based on the correlation functions can be found in [4, 6, 7]. In the present paper we consider the pair correlation function for the Langevin force, $\langle F_L(q,t) F_L(q,t') \rangle$, where the sign $\langle \ldots \rangle$ means the ensemble averaging over initial states of environment, i.e. the 1D lattice. From Eq. (9) it follows:

$$\begin{aligned} \langle F_L(t) F_L(t') \rangle = \sum_{k,k'} \big\langle \Phi_k \Phi_{k'} Q_{k0} Q_{k'0} \times \\ \times \cos(\Omega_k (t - t_0) + \varphi_k) \cos(\Omega_{k'}(t' - t_0) + \varphi_{k'}) \big\rangle. \end{aligned} \tag{10}$$

Herein and in what follows we omit the symbol q in the correlation function $\langle F_L(t) F_L(t') \rangle$. We consider oscillations of each pair of lattice particles independently, so that all terms with $k \neq k'$ in the double sum in Eq. (10) go to zero. It is clear that one of the terms in Eq. (10), proportional to $\cos\left(\Omega_k (t + t' - 2t_0) + 2\varphi_k\right)$, vanishes after averaging over φ_k. Then, we get the following result,

$$\begin{aligned} C(t) = \langle F_L(t) F_L(t') \rangle = \frac{1}{2} \sum_k \Phi_k^2 \langle Q_{k0}^2 \times \\ \times \cos\left(\omega_0 (1 + \gamma Q_{k0}^2)(t - t')\right) \rangle, \end{aligned} \tag{11}$$

where γ is defined from Eq. (7),

$$\gamma = \frac{3\beta}{8\omega_0^2} - \frac{5\alpha^2}{12\omega_0^4}, \tag{12}$$

and Q_{k0} independence of Φ_k is taken into account. Thus, Φ_k may be taken out of the sign for average. We suppose that the initial energy of the oscillators obeys the Gibbs distribution. After averaging we have

$$\begin{aligned} &\langle Q_{k0}^2 \cos\left(\omega_0 (1 + \gamma Q_{k0}^2)(t - t')\right) \rangle = \\ &= A \int_0^\infty dQ_{k0}\, Q_{k0}^2 \cos\left[\omega_0 (1 + \gamma Q_{k0}^2)(t - t')\right] \times \\ &\times \exp\left(-\frac{M \omega_0^2 Q_{k0}^2}{k_B T}\right), \end{aligned} \tag{13}$$

where is the normalization factor, $A = \sqrt{\dfrac{2\pi k_B T}{M \omega_0^2}}$.

Calculation of the integral in Eq. (13) gives

$$\begin{aligned} C(\tau) &= \langle F_L(t) F_L(0) \rangle = \\ &= C(0) \frac{\xi^{3/2}}{\left(\tau^2 + \xi^2\right)^{3/4}} \cos\left(\tau + \frac{3}{2} \arctan \frac{\tau}{\xi}\right), \end{aligned} \tag{14}$$

where $\tau = \omega_0 t$ is the dimensionless time, $\xi = \dfrac{M \omega_0^2}{k_B T \gamma}$ is the parameter describing the nonlinearity, $C(0) = \dfrac{A\sqrt{\pi}}{(4\gamma\xi)^{3/2}} \sum_k \Phi_k^2$ is the variance of the Langevin force.

A shape of correlation function $C(\tau)$ is determined by the parameter $\dfrac{\xi}{\omega_0}$. It is the characteristic time of correlation due to the non-linearity of interaction between the lattice particles. It is clearly seen from Fig. 2 that for the strong non-linearity (i.e. if $\xi \ll 1$) the correlation function becomes close to the delta-function, whereas in the case of linear oscillations the correlator is a periodic function. It can also be shown analytically that Eq. (14) is a pre-limit form of the delta function. If $\tau \to \infty$, correlations decrease to zero with growth of τ. On the other hand, assuming that τ comes close to zero, one can see that right hand side of Eq. (14) turns into $C(0) \sim \xi^{-3/2}$. The smaller ξ is, the closer correlations become to delta-functional. Sharpness of the delta function peak is also determined by the value of ξ and grows as $\xi^{-3/2}$.

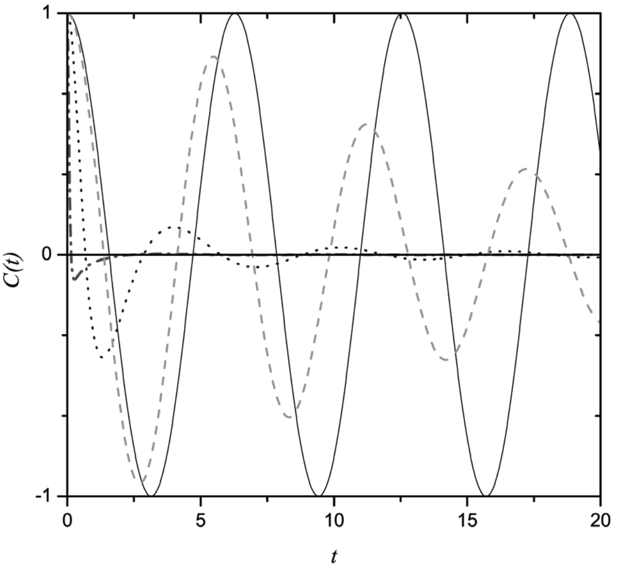

Fig. 2. The $C(t)$ dependence of the normalized correlation function of the Langevin force at different values of the parameter $\alpha = \gamma k_B T / M \omega_0^2$ ($\alpha = 0.1$, dashed line; $\alpha = 1$, dotted line; $\alpha = 10$, dash-dotted line; the case of linear oscillations corresponds to $\alpha = 0$, solid line).

We would like to mention that the correlator $C(t)$ also depends on q. It is clear that this dependence is periodic with the period l. One can see that the sharpness of the potential determines the amplitude of correlations. The more the gradient of potential along the direction of motion is, the more this motion is correlated.

In Eq. (9) all the summands are independent and normally distributed. It follows from the central limit theorem that the Langevin force distribution law is Gaussian too. The variance of its distribution is equal to the correlation function at the point $t = t'$:

$$\langle F_L^2 \rangle = \frac{\sqrt{2}\pi (k_B T)^2}{8(M\omega_0^2)^2} \sum_k \Phi_k^2. \tag{15}$$

So we can see that the root mean square value of the Langevin force grows with the temperature as T. At high temperatures the variance of the Langevin force increases and correlation function comes closer to the delta function.

Lattice model with linear longitudinal displacement of atoms

In the model considered below, we suppose the particles of the lattice interact with the nearest neighbours only and move along the axis of 1D crystal. In this case the Hamiltonian of the system differ from the one in Eq. (1) in potential energy of the lattice atoms of the k-th site. The latter now depends not only on the displacement Q_k, but also on displacements of all the other lattice sites (which now directed along the doping particle motion).

Similarly to what has been stated in previous sections, let us first determine the motion of the lattice particles taking account of the motion of a foreign particle. To simplify the problem, assume that particles interact solely with two nearest neighbours, and the potential energy of interaction is quadratic in displacement. The lattice can then be viewed as if each lattice atom is coupled with two neighbours via springs with equal force K, as shown in Fig. 3. This reduces the formulated problem to the well known one pertinent to the dynamics of the linear chain of coupled oscillators.

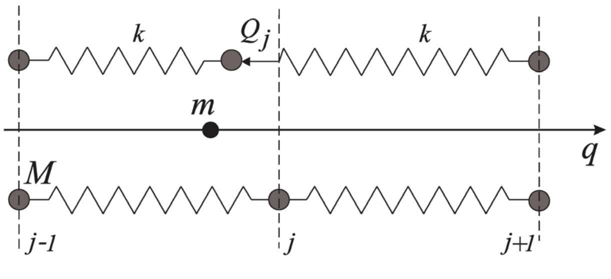

Fig. 3. Model of 1D lattice with longitudinal displacements.

Equation of motion for the -th oscillator now reads as

$$M\ddot{Q}_k = K(Q_{k-1} + Q_{k+1} - 2Q_k). \tag{16}$$

Looking for the solution of Eq. (16) in the form of the travelling wave $Q_k = A\exp\left(i(\omega t - \varkappa k)\right)$, we obtain the following dispersion equation:

$$M\omega^2 = K\left(2\sin\frac{\varkappa}{2}\right)^2. \tag{17}$$

We choose the cyclic boundary conditions, i.e. $Q_0 = Q_N$, which is equivalent to $\exp(i\varkappa N) = 1$. It means that $\varkappa$ takes on the discrete set of values:

$$\varkappa_l = \frac{2\pi l}{N} = \frac{2\pi l a}{L}, \tag{18}$$

where a is the distance between neighbouring atoms (the lattice period), L stands for a characteristic length of the crystal.

So, oscillations of each lattice particle appear to be the superposition of the obtained standing waves. Since the initial time moment and the initial coordinate are arbitrary, Eq. (16) can be rewritten as follows:

$$Q_k = \sum_{l=1}^{N-1} A_l \sin(\omega_l t + \varphi_l)\cos(\varkappa_l k). \tag{19}$$

The summation starts with $l = 1$ because we do not make allowance for the motion of the lattice as a whole. Parameters and φ_l are independent stochastic values. A_l is distributed according to the Gibbs law, and φ_l is uniformly distributed within the interval $(0, 2\pi)$.

The doping particle affects the motion of lattice particles which leads to the addition of summand in Eq. (19):

$$Q_k = \sum_{l=1}^{N-1} A_l \sin(\omega_l t + \varphi_l)\cos(\varkappa_l k) + G(t). \tag{20}$$

We do not consider an exact expression for $G(t)$, because we are interested only in the stochastic component of Q_k. The equation of motion for the doping particle is the same as Eq. (4), so the expression for the Langevin force is

$$F_L(q,t) = \sum_{k,l} \Phi_k(q) A_l \sin(\omega_l t + \varphi_l)\cos(\varkappa_l k). \tag{21}$$

One can see that the summation over k coincides with the Fourier transform. Introducing the new notation $\hat{\Phi}_\varkappa = \sum_k \Phi_k \cos(\varkappa k)$, we obtain

$$F_L(t) = \sum_l \hat{\Phi}_{\varkappa_l} A_l \sin(\omega_l t + \varphi_l). \tag{22}$$

Using the expression for the Langevin force, Eq.(22), we can derive the expression for its correlation function:

$$\langle F_L(t)F_L(t')\rangle = \langle \sum_{l,l'} \hat{\Phi}_{\varkappa_l} \hat{\Phi}_{\varkappa_{l'}} A_l A_{l'} \times \\ \times \sin(\omega_l t + \varphi_l)\sin(\omega_{l'} t' + \varphi_{l'})\rangle. \tag{23}$$

It is evident that $\langle A_l\rangle = 0$, $\langle A_l A_{l'}\rangle = 0$, $\langle A_l^2\rangle = \dfrac{k_B T}{m\omega_l^2}$.

Thus,

$$\langle F_L(t)F_L(t')\rangle = \sum_l \hat{\Phi}^2_{\varkappa_l} \frac{k_B T}{m\omega_l^2}\cos\big(\omega_l(t-t')\big). \tag{24}$$

Using Eq. (17) we can calculate the sum in Eq. (24).

So, we have obtained the expression for the correlation function of the Langevin force in the case of interacting lattice particles. To calculate correlation function (24), we can replace the sum in Eq. (24) by the integral (as in [3]). The plot of this function is presented in Fig. 4. One can then note that the correlation function becomes a delta function if the spectral density of oscillations is quadratic.

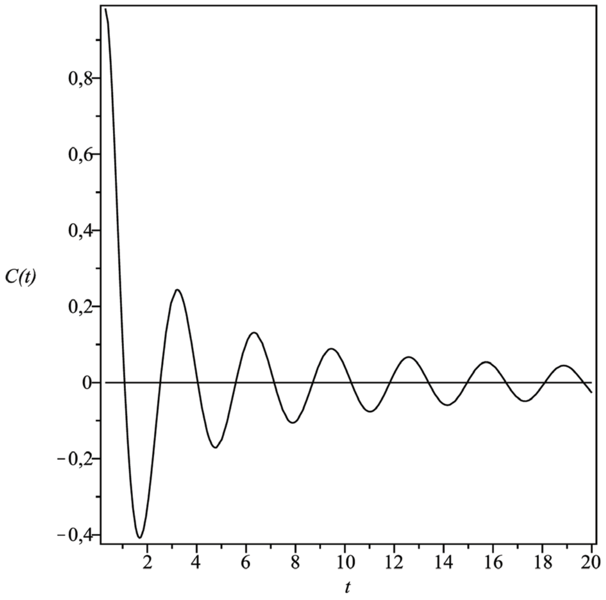

Fig. 4. The normalized correlation function of the Langevin force in approximation of linear longitudinal oscillations.

The right-hand side of Eq. (22), as in Sec.2c, is a sum of independent Gaussian distributed random values. Consequently, the Langevin force (22) is normally distributed too.

In conclusion, we should emphasize that the pair correlation function of the Langevin force plays a great role in determining the doping particle motion. So, the equations obtained are very important for the solution of the diffusion problem.

1. A. Einstein. Ann. Phys., 17, 549 (1905).
2. G. Sesé, E. Guàrdia and J. A. Padró. J. Stat. Phys., 60, 3-4, 501 (1990).
3. P. Fröbrich, I. I. Gontchar. Phys. Rep., 292, 3-4, 131 (1998).
4. William T. Coffey, Yu. P. Kalmykov, J. T. Waldron. The Langevin Equation: With Applications to Stochastic Problems in Physics, Chemistry and Electrical Engineering, v. 14, 2nd ed., World Scientific Series in Contemporary Chemical Physics, Singapore, (2004), 678 p.
5. A. M. Kosevich, A. S. Kovalev. Introduction in nonlinear physical mechanics, Naukova dumka, Kiev, (1989), 320 p.
6. R. Kubo. Statistical mechanics: an advanced course with problems and solutions, North Holland, (1990), 430 p.
7. O. V. Usatenko, S. S. Apostolov, Z. A. Mayzelis and S. S. Melnik. Random Finite-Valued Dynamical Systems: Additive Markov Approach, Cambridge Scientific Publishers, Cambridge, (2009), 171 p.

Вісник ХНУ, № 1135, серія «Фізика», вип. 21, 2014. с. 61-64

PACS 05.45.Xt, 74.50.+r, 85.25.Cp
УДК: 537.312.62

Zero-field steps in long Josephson junctions

Alexander Grib

Physics Department, Kharkiv
V. N. Karazin National University,
Svobody sq. 4, 61022, Kharkiv, Ukraine

IV-characteristics of a long Josephson junction with normal edges were calculated. Boundary conditions were modeled as shunts which consist of resistances, inductances and capacitances. IV-curves revealed self-induced resonant steps (zero-field steps) near voltages corresponding to frequencies of even-order modes of geometrical resonances (even Fiske steps). The dependence of the difference between resonant frequencies on the reciprocal length of the junction is in agreement with the theory. Conditions of the application of the model for the description of intrinsic Josephson junctions in high-temperature superconductors are discussed.

Keywords: Josephson junctions, high-temperature superconductors, transmission line, resonant modes.

Розраховано вольт-амперні характеристики довгого джозефсонівського контакту з нормальними краями. Граничні умови моделювалися як шунти, що мають електричний опір, індуктивність та ємність. На вольт-амперних характеристиках виявлено самоіндуковані резонансні сходинки (сходинки нульового поля) поблизу напруг, які відповідають частотам парних мод геометричних резонансів (парні сходинки Фіске). Залежність різниці між частотами резонансів від зворотної довжини контактів узгоджується з теорією. Обговорюються умови використання моделі для опису внутрішніх джозефсонівських контактів у високотемпературних надпровідниках.

Ключові слова: джозефсонівські контакти, високотемпературні надпровідники, довга лінія, резонансні моди.

Рассчитаны вольт-амперные характеристики длинного джозефсоновского контакта с нормальными краями. Граничные условия моделировались как шунты, которые имеют электрическое сопротивление, индуктивность и ёмкость. На вольт-амперных характеристиках найдены самоиндуцированные резонансные ступеньки (ступеньки нулевого поля) вблизи напряжений, которые отвечают частотам чётных мод геометрических резонансов (чётные ступеньки Фиске). Зависимость разницы между частотами резонансов от обратной длины контактов согласуется с теорией. Обсуждаются условия использования модели для описания внутренних джозефсоновских переходов в высокотемпературных сверхпроводниках.

Ключевые слова: джозефсоновские переходы, высокотемпературные сверхпроводники, длинная линия, резонансные моды.

Introduction

It was recently found [1-3] that intrinsic Josephson junctions in mesas of high-temperature superconductors (HTSC) revealed coherent emission at voltages corresponding to frequencies of geometrical resonances of microwaves. Self-resonant steps in IV-characteristics were observed at these resonances [1]. In experiments [1-3] mesas were biased only by the direct current. External magnetic field was not applied. The theory of resonant steps in IV-curves of junctions placed in external magnetic field (so-called Fiske steps) was developed in Refs. 4, 5. However, the appearance of self-resonant steps in the absence of external applied magnetic field (so-called zero-field steps) was also observed experimentally [6,7]. The proposed mechanisms of the vortex motion inside the junction [8] allowed explaining the appearance of zero-field steps at even resonant frequencies. The quantitative explanation of the appearance of zero-field steps referring to the general theory [4, 5] was made in Ref. 9.

In theoretical investigations the resistive shunt over the whole stack of intrinsic Josephson layers was used to model their properties [10]. Earlier we showed theoretically that coherent radiation appeared at self-resonant steps of the IV-curve of the chain of Josephson junctions placed in the transmission line [11-12]. The existence of self-resonant steps was proved experimentally [13, 14]. In the present paper we show that in the long Josephson junction zero-field steps can appear if plausible boundary conditions are fulfilled. The described below conditions can be valid in high-temperature superconductors. Superconducting properties of these systems are strongly dependent on the content of the oxygen in superconducting layers. Diffusion of the oxygen out of superconducting layers leads to the change of the critical temperature at ends [1]. Moreover, one can expect that some small parts of superconducting layers at ends of the superconductor can be in the normal state. One can model boundary conditions of an intrinsic Josephson junction in such a superconductor as shunts consisting of inductances, resistances and capacitances (so-called RLC-shunts). We used the 'lumped' model of a long Josephson junction [15] in which the junction was represented as a set of radio-technical elements. The RLC-shunt is a model of the state when the insulating barrier is placed between non-superconducting parts of layers at the ends of the tunnel junction. We calculated IV-characteristics of the junction with the mentioned boundary conditions and showed that zero-field steps appeared at voltages corresponding to even modes of geometrical resonances in the junction. We also discussed the dependence of the distance between zero-field steps on the reciprocal dimension of the system.

The model.

The geometry of the long Josephson junction is presented in Fig. 1a, and the high-frequency scheme of the junction is shown in Fig. 1b. The junction with the critical current I_{ctot} is divided into n ‘elementary junctions’ with critical currents I_{ctot}/n. ‘Elementary junctions’ in Fig. 1b are presented in the range of the resistively and capacitively shunted model [15] with the resistance R_k, capacitance C_k and the source of the Josephson current $I_{ck}\sin\varphi_k$ for the k-th junction (k = 1…n). In the following consideration we assume that for all k the condition $C_k = C$, $R_k = R$ and $I_{ck}=I_c$ is valid. ‘Elementary junctions’ are divided by the distance $\zeta = \overline{c}\sqrt{CL}$, where $\overline{c}$ is the velocity of light in the junction and L is the inductance of the ‘elementary cell’ between junctions. Then the current conservation conditions for junctions together with equations for circulating currents in loops between junctions are as follows:

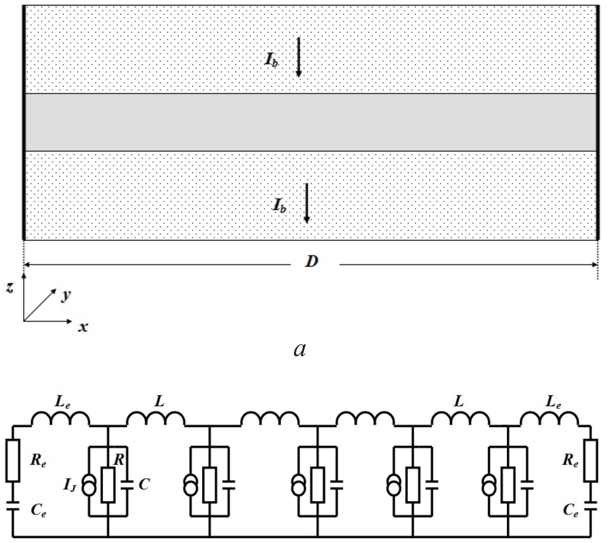

a

b

Fig. 1. (a)- the long Josephson junction. Insulator is shaded. Black solid lines at ends of the junction symbolize the $R_eL_eC_e$-shunting discussed in the paper. (b)- the electrical scheme of the junction. The shown circuit consists of 4 cells and 5 junction. The additional boundary circuit contours are also shown. In calculations the number of cells was 200-500.

$$\begin{aligned}&\frac{\Phi_0 C}{2\pi}\frac{d^2\varphi_k}{dt^2}+\frac{\Phi_0}{2\pi R}\frac{d\varphi_k}{dt}+I_c\sin\varphi_k = \\ &= I_b - I_k^R + I_{k+1}^R\end{aligned}, \quad (1a)$$

$$I_k^R = -\frac{\Phi_0}{2\pi L}\left[\varphi_{k-1}-\varphi_k\right], \quad (1b)$$

where $k = 2…n$-1, φ_k is the phase difference across the k-th junction and Φ_0 is the quantum of magnetic flux.

It can be shown that equations (1a) and (1b) represent the written in finite differences main equation of the electrodynamics of the long Josephson junction [15]. Let us introduce parameters $\overline{c}^2 = 1/\left(\mu_0 C^S d\right)$, $\lambda_J = \left[\hbar/\left(2\mu_0 e J_c d\right)\right]^{1/2}$ and $\beta = 1/\left(RC\right)$ with $d = l + \lambda_{L1} + \lambda_{L2}$ is the sum of London depths of penetration of electromagnetic field into the first and the second superconductors λ_{L1} and λ_{L2}, correspondingly, l is the thickness of the insulator barrier, μ_0 is magnetic permeability of vacuum, J_c is the density of the critical current, C^S is the capacitance per unit area and λ_J is the Josephson depth of penetration of magnetic field in the junction. With the use of these parameters for $\zeta\to 0$ one obtains the equation

$$\begin{aligned}&\frac{\partial^2\phi(x,t)}{\partial x^2}-\frac{1}{\overline{c}^2}\left[\frac{\partial^2\phi(x,t)}{\partial t^2}+\beta\frac{\partial\phi(x,t)}{\partial t}\right]= \\ &=\frac{1}{\lambda_J^2}\left[\sin\phi(x,t)-\frac{I_b}{I_c}\right]\end{aligned}. \quad (2)$$

Note that the well-known sine-Gordon equation [16] is obtained from Eq. (2) if terms containing β and I_b/I_c are omitted.

There are not analytical solutions of Eq. (2). Therefore, we solved the corresponding system of Eqs. (1a) and (1b) numerically.

To form boundary conditions, additional contours with capacitances C_{ek}, inductances R_{ek} and inductances L_{ek} were added to both ends of the line. The Kirchhoff’s circuit laws for these contours are following:

$$\begin{aligned}&L_{ek}\frac{d^2 q_k}{dt^2}+R_{ek}\frac{dq_k}{dt}+\frac{q_k}{C_{ek}}= \\ &=\mp\frac{\Phi_0}{2\pi}\frac{d\varphi_k}{dt}\end{aligned}, \quad k = 1, n, \quad (3)$$

where the upper signs in the right side relate to k =*1* (the left end of the junction), the lower signs relate to $k = n$ (the right side of the junction) and q_k is the charge flowing through the inductance L_{ek}. In the beginning of calculations we set the length D and the width W of the long junction, the density of the critical current J_c, the critical voltage V_c, the inductance of the junction per unit of length L_{ul} and the velocity of light in the junction $\bar{c}$. Note that our model is quasi-one-dimensional, so the introduction of the width W is made merely to calculate J_c. Then the junction was divided into n cells with the length $\zeta = D/n$. Parameters of 'elementary junctions' and cells were equal to $I_c = J_c\cdot W\cdot\zeta$, $R = V_c/I_c$, $L = L_{ul}\cdot\zeta$ and $C = \zeta^2/\left(\bar{c}^2 L\right)$. The last relation follows from the constant velocity of light in the long junction that should provide the transmission line (see Fig. 1b). Note that the value of the McCumber parameter $\beta_C=(2\pi I_c R^2_n C)/\Phi_0$ does not depend on ζ. Then Eqs. (1a) and (1b) with boundary conditions (3) were solved by the method of Runge-Kutta for different values of the bias current. IV-characteristics were obtained in calculations. The voltage over the junction was calculated as $V = \frac{\Phi_0}{2\pi n}\left\langle \sum_{k=1}^{n} \frac{d\varphi_k}{dt} \right\rangle$, where the sign $\langle\ldots\rangle$ means full averaging over the large interval of time $T_J >> (1/\nu_J)$ with ν_J is the characteristic frequency of Josephson generation.

Results and discussion.

Values of parameters for calculations were chosen as follows. The parameter D was changed from $50\cdot10^{-6}$ m to $650\cdot10^{-6}$m. Other parameters were $W=300\cdot10^{-6}$ m, $J_{ctot}= 10^5$ A/m^2, $L_{ul}=1.25\cdot10^{-8}$ H/m, V_c = 4.74 mV, $\bar{c} = 6.708\cdot10^7$ m/sec [1], $\beta_C=40.34$, $n=200\div500$. Calculated parameters λ_J and d were $2.97\cdot10^{-5}$ m and $2.98\cdot10^{-6}$ m, correspondingly. The wavelength of the first harmonic of Josephson generation $\lambda = \bar{c}\Phi_0/V_c$ at the characteristic voltage V_c was equal to $\lambda = 29.3\cdot10^{-6}$ m.

Now we discuss the choice of parameters. We chose the described values because they are close to corresponding parameters of intrinsic Josephson junctions in high-temperature superconductors [17]. At the same time, it is known that the model of the resistively and capacitively shunted Josephson junction is not quite adequately describe intrinsic junctions [17], so some parameters like λ_J and β_C are different from those in HTSC. We note also that the thickness of the superconducting layer in HTSC is only two or three tenths of nanometer, whereas in the model we use the value d of order of micrometers. Therefore, we found IV-characteristics of the Josephson junction which has some characteristic parameters of intrinsic Josephson junctions. For the adequate description of intrinsic junctions the present model should be changed to take into account the narrow layers of the superconductor and the periodic layered structure of HTSC.

For boundary conditions we chose values of R_{ei}= 100 Ohm, L_{ei} = 0.2 pH, C_{ei} = 3pF for both boundaries with i=1 and i=n which correspond to approximately 2-5 micrometers of the non-superconducting part at edges. The resonant frequency of the $L_{ei}C_{ei}$-resonance contour is much larger than the characteristic frequency of Josephson generation. We checked that the choice of values of the parameter n did not influence results of calculations.

The example of the IV-characteristic of the junction with the length $1.80\cdot10^{-4}$ m is shown in Fig. 2. It is seen that there are zero-field steps in the IV-characteristic. In Fig. 2 these steps are numbered from 1 to 4. Note that Eqs. (3) describe additional ac current contours through which some electromagnetic excitations enter the long junction. The frequency of these excitations coincides with the frequency of Josephson generation, and they propagate along the long junction and reflect from its ends. Resonance voltages in this model are described by such an expression [8,9]:

$$V_m = \frac{\Phi_0 \bar{c} m}{D}, \tag{4}$$

where m=1,2,3… is an integer. These voltages correspond to even Fiske steps $V_p = (\Phi_0\bar{c}p)(\ 2D)$, with p is an integer, so $p = 2m$. We noted positions of V_m by short arrows in Fig. 2. It is seen that positions of V_m do not coincide with steps obtained from solutions of Eqs. (1a)-(1b). More adequate equidistant steps were found from data of Fig. 2 empirically (they are shown by long arrows). We explain this deviation by the influence of higher harmonics of Josephson generation in the hysteretic region.

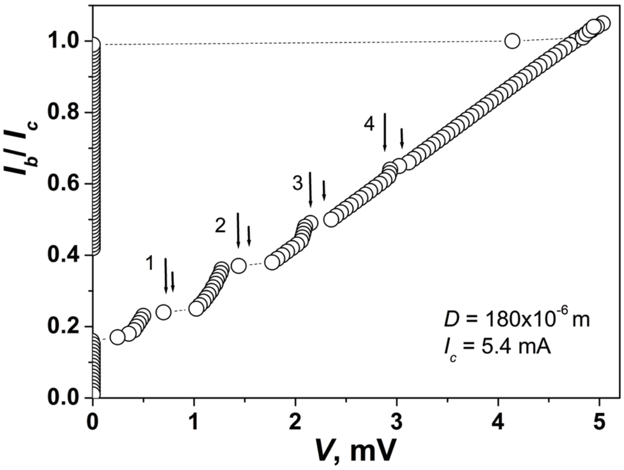

Fig. 2. The IV-characteristic (circles) of the junction with the length 180 micrometers. The jump of voltages at $I_b = I_c$ is marked by dashed line. Steps are numbered from m =1 to m = 4. Short arrows show positions of voltages $V_m = \Phi_0\bar{c}m/D$, long arrows show equidistant steps found empirically.

To show that the distance between steps in IV-characteristics is proportional to the reciprocal length of the junction (see Eq. (4)), we calculated averaged values of $\Delta V=V_m-V_{m-1}$ for the junction with the given D and plotted the difference of frequencies $\Delta f = \Delta V/\Phi_0$ on the value of $1/D$ (Fig. 3). For the comparison the dependence $\Delta f' = \dfrac{\Delta V}{\Phi_0} = \dfrac{\overline{c}}{D}$ obtained from Eq. (4) is also plotted in the same figure. It is seen from Fig. 3 that data obtained from the numerical model is in accordance with the theoretical plot.

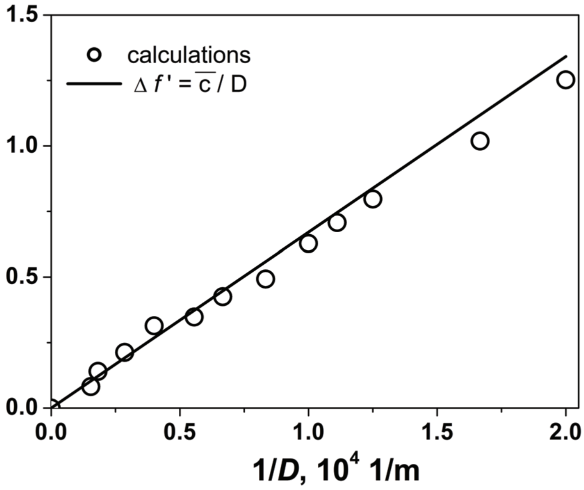

Fig. 3. The dependence of Δf on the reciprocal width of the junctions $1/D$ (circles). Solid line is the dependence $\Delta f' = \overline{c}/D$.

We found that the investigated effect of zero-field steps is observed in the very wide range of parameters R_{ek}, L_{ek} and C_{ek} for boundary conditions Eq. (3) providing and $R_{ek} \neq \infty$. Mentioned parameters can change by many orders of magnitude, but the change of both positions of steps and heights of steps is small. This result proves the supposition that the additional boundary contours plays the role of generators of excitations and makes more probable our supposition that described boundary conditions are responsible for the appearance of zero-field steps in HTSC. We checked that zero-field steps appeared also if ends of the long junction were superconducting but with slightly different critical currents. Thus, self-resonant steps can appear if electromagnetic excitations enter the junction from ends.

Conclusions

In the present paper we calculated IV-characteristics of the long Josephson junction with boundary conditions which correspond to shunts which consist of resistances, inductances and capacitances. These boundary conditions model the single intrinsic Josephson junction with the insufficient content of the oxygen at edges. IV-curves reveal zero-field resonant steps. Frequencies at which these steps are observed correspond to the even geometrical resonances in the structure (even Fiske steps). We analyzed the dependence of the difference between frequencies of steps on the reciprocal length of the junction. This dependence is in agreement with predictions of the theory.

1. L. Ozyuzer, A. E. Koshelev, C. Kurter, N. Gopalsami, Q. Li, M. Tachiki, K. Kadowaki, T. Yamamoto, H. Minami, H. Yamaguchi, T. Tachiki, K. E. Gray, W.-K. Kwok, U. Welp. Science, 318, 1291 (2007).
2. B. Gross, S. Guénon, J. Yuan, M. Y. Li, J. Li, A. Ishii, R. G. Mints, T. Hatano, P. H. Wu, D. Koelle, H. B. Wang, and R. Kleiner. Phys. Rev. B 86, 094524 (2012).
3. Mengyue Li, Jie Yuan, Nickolay Kinev, Jun Li, Boris Gross, Stefan Guénon, Akira Ishii, Kazuto Hirata, Takeshi Hatano, Dieter Koelle, Reinhold Kleiner, Valery P. Koshelets, Huabing Wang, and Peiheng Wu. Phys. Rev. B 86, 060505(R) (2012).
4. I. O. Kulik. Zh. Eksp. Teor. Fiz. Pis. Red., 2, 134 (1965) [JETP Lett., 2, 84 (1965)].
5. I. O. Kulik. Zh. Tekh. Fiz., 37, 157 (1967) [Sov. Phys. Tech. Phys., 12, 111 (1967)].
6. I. M. Dmitrenko, S. I. Bondarenko and T. P. Narbut. Zh. Eksp. Teor. Phys. 57, 1513 (1969). [Sov. Phys. JETP, 30, 817 (1970)].
7. J. T. Chen, T. F. Finnegan and D. N. Langenberg. Physica (Utr.) 55, 413 (1971).
8. T. A. Fulton and R. C. Dynes. Solid State Commun., 12, 57 (1973).
9. K. Takanaka. Solid State Commun., 29,443 (1979).
10. B. Gross, J. Yuan, D. Y. An, M. Y. Li, N. Kinev, X. J. Zhou, M. Ji, Y. Huang, T. Hatano, R. G. Mints, V. P. Koshelets, P. H. Wu, H. B. Wang, D. Koelle, and R. Kleiner. Phys. Rev. B 88, 014524 (2013).
11. Alexander Grib and Paul Seidel. Low Temp. Phys. 38, 321 (2012).
12. Alexander Grib and Paul Seidel., J. Phys.: Conf. Ser., 507, 042038 (2014).
13. A. Grib, M. Mans, M. Büenfeld, J. Scherbel, F. Schmidl, H. Schneidewind, and P. Seidel. IEEE Trans. Appl. Supercond., 24, 1800205 (2014).
14. Alexander Grib, Michael Mans, Jens Scherbel, Matthias Büenfeld, Frank Schmidl and Paul Seidel. Supercond. Sci. Technol., 19, S200 (2006).
15. K. K. Likharev. Dynamics of Josephson junctions and circuits, Gordon and Breach, Philadelphia. (1991), 750 p**.**
16. Antonio Barone and Gianfranco Paternò. Physics and applications of the Josephson effect, A Wiley-Interscience Publication, New York (1982), 529 p.
17. R. Kleiner and P. Müller, Phys. Rev. B, 49, 1327 (1994).

Вісник ХНУ, № 1135, серія «Фізика», вип. 21, 2014. с. 65-67

УДК 620.22.66.067.124
PACS

The influence of zirconium oxide on Al_2O_3-TiC oxide-carbide ceramics

E.S.Gevorkyan[2], G.Ya.Khadzhay[1], R.V.Vovk[1], O.M.Melnik[2]

[1]Харьковский национальный университет имени В.Н. Каразина, 61022, пл. Свободы 4, Харьков, Украина
[2]Украинская государственная академия железнодорожного транспорта, пл. Феербаха 7, Харьков, Украина

Time-dependent change of electrical resistance for 56 vol. % Al_2O_3+36 vol. % TiC + 8 vol. % ZrO_2 sample, obtained by means of electrical consolidation has been investigated in the article. The mechanism of carbon concentration change while compacting has been investigated and it was determined that under the condition that the content is 36 vol. % TiC, that slightly exceeds percolation threshold, it is possible to obtain a dense sample having grain shape different from spherical. That allows us to reach coordination number 4 to provide the percolation process possibility.

Keywords: electrical resistance, oxide-carbide ceramics, percolation threshold, electrosintering.

У статті досліджено зміну електроопору від часу для зразка складу 56% об.Al_2O_3+36% об.TiC+8% об.ZrO_2, отриманого методом електроконсолідації. Досліджено механізм зміни концентрації вуглецю в процесі компактування та встановлено, що при вмісті 36 об.% TiC, що незначно перевищує поріг перколляції, можливе отримання щільного зразка з формою зерен відмінною від сферичної, що дозволяє досягти координаційного числа 4 для забезпечення можливості перколяційних процессів.

Ключові слова: електроопір, оксидо-карбідна кераміка, поріг перколяції, електроспікання.

В статье исследовано изменение электросопротивления от времени для образца состава 56% об.Al_2O_3+36% об.TiC+8% об.ZrO_2, полученного методом электроконсолидации. Исследован механизм изменения концентрации углерода в процессе компактирования и установлено, что при содержании 36 об.% TiC, что несколько превышает порог перколляции, возможно получение плотного образца с формой зерен отличной от сферической, что позволяет достичь координационного числа 4 для обеспечения возможности перколяционных процессов.

Ключевые слова: электросопротивление, оксидо-карбидная керамика, порог перколяции, электроспекание.

Al_2O_3-TiC oxide-carbide ceramics has found wide application as tool material in steel and alloy working. Cutting force, friction force, high temperature, which can reach 1200°C under high speeds, affect tool material during the process of cutting. It is natural, that under such conditions cutting material wears out intensively, that leads to frequent tool failures and disruptions.

Different physics-chemical processes, which take place in the cutting area, influence wear mechanism. The main wear mechanisms are: abrasive, adhesive, diffusive and electrical-chemical [2].

This or that wear mechanism prevails in each separate case, though it is obvious, that all the factors have definite effect.

To increase the instrument lifetime, first of all, it is necessary to improve the hardness and strength of cutting material, chemical inertness to the interaction with the material being worked [3, 4, 5].

From this point of view, zirconium oxide additives to Al_2O_3-TiC oxide-carbide ceramics are interesting. It is known that transformational transitions of zirconium oxide from tetragonal modification to monoclinic create microcrack structure, which substantially increasesfracture toughness of a composite [6].

The obtained material is interesting not only as instrumental but as a structural, particularly to be used as blades of a gas-turbine engine, for rocket nozzle inserts, for oil pumping O-rings etc. It is obvious that the investigation of not only mechanical but physical, particularly electrical, characteristics of the given composite is of great importance.

Electrical characteristics influence the workability of the material while applying electrical- physical methods of geometrically-complex product working. The mentioned methods allow decreasing structure imperfection being formed afterdiamond grinding, particularly diamond-spark grinding electric erosion machining.

The temperature in the cutting area is affected by the thermal conductivity of cutting material; in case of increased thermal conductivity the temperature decreases that in whole influences wear resistance of cutting composite. The investigations of electrical resistance and thermal conductivity of similar composites are practically absent in the literature. The conducted investigations of Al_2O_3+TiC+ZrO_2 sample electrical resistance in the range of temperatures 290÷315 K revealed a number of interesting peculiarities of this material.

Methods of investigation

The sample has been produced by means of compacting a homogeneous mixture of 56 vol. % Al_2O_3+36 vol. % TiC+8 vol. % ZrO_2 powders at T=1550 °C, P=45 MPa and direct (alternating) current I = 5000A. Conducting phase is TiC, volume fraction of which is 0.36. The sample represented parallelepiped with the dimensions 16x16x4.8 mm.

The measuring of electrical resistance of the sample was conducted by means of a conventional four-probe method in ~10^{-5} torr in vacuum at constant temperature, which was supported by an analogue thermoregulator with the accuracy to ~0.1 K and was measured by platinum resistance thermometer. Temperature dependence was obtained in one-day cycle of measurements. Such cycle was repeated during 12 days.

Investigation results

It was determined that specific electrical resistance TiC_n is strongly dependent upon its imperfection on carbon, changing at 25°C from ρ=61 microOhm·cm for $TiC_{0.96}$ to ρ=147 microOhm·cm.

The sample specific resistance, as it was established, is by 2 orders higher than specific resistance of titanium monocarbide that can be the result of percolation nature of investigated samples conductivity.

Coordination number, that effects specific electrical resistance, can appear in the case when carbide grains of titanium monocarbide are bigger than the grains of other phases as well as the in the case when the grain shape of all the phases has the shape that is far from spherical.

The discussion of the results

As it turned out, the sample resistance depends upon the temperature linear, however the parameters of this dependence had been changed with the time passing and their values were stabilized only after 10 cycles. The time change of resistance for T=298 K is presented in Fig. 1. Maximal change of the resistance is 1.5%.

Temperature dependence of a stabilized resistance can be described by the ratio

$$R(T)=R_0+B*T, \qquad (1)$$

Where $R_0=(4.98\pm0.02)\cdot10^{-2}$ Ohm and $B=(3.5\pm0.1)\cdot10^{-5}$ Ohm/K. The parameter $R_0=R(0)$ makes sense of a residual resistance. Temperature coefficient of resistance (TCR) at 298 K is $\frac{1}{R}\frac{dR}{dT}\approx 5.8\cdot10^{-4}K^{-1}$, that approximately 3 times less than ZrC has and approximately 4 times less than HfC has [7]. The ratio $R(298\ K)/R_0\approx1.2$ that features "dirty" conductor.

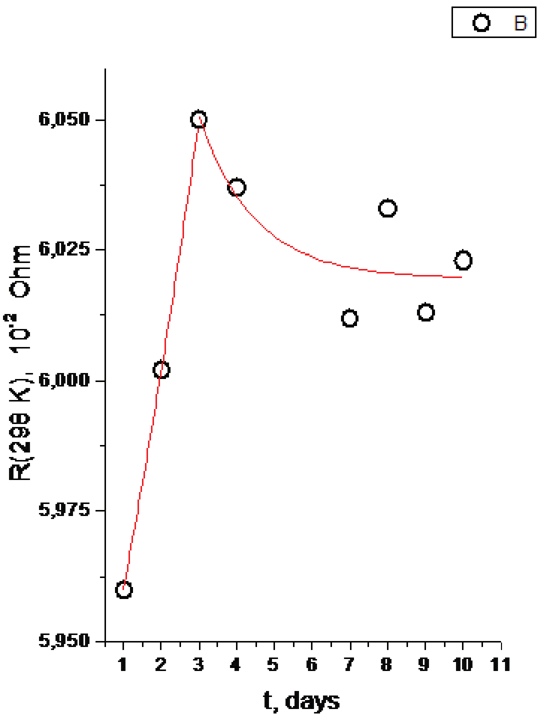

Fig. 1 Time-dependent change of electrical resistance for 56 vol. % Al_2O_3+36 vol. % TiC+8 vol. % ZrO_2 sample for T=298 K

Resistivity TiCn depends heavily upon its carbon faultiness, changing at 25°C from ρ=61 microOhm*cm for $TiC_{0.96}$ to ρ=147 microOhm*cm for $TiC_{0.62}$ [8] and can be described by the ratio

$$\rho(25°C, n)=(302-252*n)\ \text{mcOhm*cm} \qquad (2)$$

As we know virtually nothing about relative position of conducting areas, it is impossible to calculate the sample resistance knowing TiC resistance and its inclusion volume fraction. However, based on the results of the work [9], we can determine the frames within which there is a value of the sample conductivity on the basis of the results of the work:

$$0\le\sigma^*\le\sigma_2\frac{2v_2}{3-v_2} \qquad (3)$$

Here σ* is effective conductance of the system, σ2 and v_2 – productivity and TiC inclusion volume fraction respectively.

We get ρ(25°C, 0.79)=103 microOhm*cm, v_2=0.36 from (2) for n=0.79 then

$$380\ \text{mcOhm*cm} \le \rho^* < \infty, \quad (4)$$

Where ρ* - the sample measured resistance.

We have ρ*(298 K)=2.9·104mcOhm*cm from (2) and the sample geometry, that is the sample measured resistance is within frames (4), however these frames are rather broad because all the other sample components (phases) are insulators.

According to [10] the difference between impedance of the material, i.e. its resistance to the direct current (ρgeneral) and the resistance of the material grain volume (ρvolume) is interpreted as the grain boundary resistance, ρboundary. However, as opposed to the volume, the conductivity of grain boundary depends on crystallite size and the resistivity of intercrystalline boundaries is higher than grain volume resistivity, as the quantity of intercrystalline boundaries per the unit of the sample length, which the current must overcome, changes depending on grain size.

Impurity segregation [11] is considered as one of the reasons of increased specific resistivity of intercrystalline boundaries.

The fact, that measured sample resistivity (specific resistance) is by a factor of hundred higher than TiC resistivity (specific resistance) can be caused by the percolation character of the sample conductivity, namely, by the proximity of conducting phase inclusion volume fraction to percolation threshold.

It is known [12], that percolation threshold for bound system with coordination number (the number of bounds) z=4 equals 1/3, that is quite close to conducting phase inclusion volume fraction (0.36) but less than it. Coordination number 4 can appear in the case if TiC particles are bigger than other phase particles or in a case if the shape of the particles of all phases is far from spherical.

Let's mention that there is a connection between parameters R_0 and B (1) which can be expressed by B=(21.0±0.5)–(3.5±0.1)*R_0 ratio. As (1) testifies to "metallic" conductivity of the system, the residual resistance R_0 is determined by the faults of conducting component (TiC). Thus, the dependence B(R_0) points to the dependence of TCR sample on titanium carbide defects. In this connection we can assume that the concentration of carbon in TiC changes while compacting at high temperatures, but in the sequel this concentration will tend to some equilibrium value including the influence of the experiment conditions – vacuum and weak temperature cycling.

Conclusions

Thus, the conducted investigations allow assuming that the content of TiC has a substantial effect on percolation threshold of Al_2O_3-TiC-ZrO_2 composite as well as on its carbon imperfection which can change, increasing electrical resistance approximately by factor of 2.5. The ratio of 56 vol. % Al_2O_3+36 vol. % TiC+ 8 vol. % ZrO_2 phases is optimal not only from the point of view of mechanical features but also from the point of view of workability by electrosparking method.

Electrical resistance can be substantially decreased by grain size reduction and the creation of nonspherical polyhedral grain size. The coefficient of thermal expansion depends to a large extent on TiC defect rate.

1. Cutting tools equipped with superhard and ceramic materials and their use: Handbook / V.P. Zhed, G.V. Borovsky, Ya.A.Muzykant, G.M. Ippolitov. -Moscow: Mashinostroenie, 1987. – 320 p.
2. N.V. Novikov, A.I. Grabchenko, E.I. Gritsenko and others. The blade tools of superhard materials: Handbook / Ed. N.V. Novikov. - Kiev: Tehnika. - 1988. -118 p.
3. Pat.6,617,271, US, Tungsten carbide cutting tool materials: USA, MCI C04 B 035/56 V.E.Kodash, E.S.Gevorkyan; Appl. 19.03.2002; Publ. 09.09.2003. - 14 p.
4. E.S.Gevorkyan, V.Y. Kodash, M.Kramer The study of properties of various cutting tool materials during processing of Ferrotitanit-S // High Technology in Mechanical Engineering: Collection of scientific papers NTU "KhPI." - Kharkiv. - 2004. - Vol. 2 (a). - P. 59-64.
5. E.S. Gevorkyan. Prospects of application of the electrosintering method for compacting nanopowders to obtain composite materials for tool and constructional purposes // Cutting and tool in technological systems: International Science and Technology collection. - Kharkov: NTU "KhPI". - 2005 - Vol. 68. - P. 123-129.
6. S.Yu.Saenko, N.N. Belash, E.S.Gevorkyan. Obtaining nanoceramics based on zirconia dioxide by hot vacuum pressing. Physics and technology of high pressure. №1, Vol. 18. – 2008. – P. 47-51.
7. Clinard F.W. Jr., and Kempter C.P. J. Less-Common Met. **15**, 59 (1968).
8. S.S.Kiparisov, Y. Levinsky, A.P. Petrov Titanium carbide: production, properties and application. Moscow: Metallurgiya, 1987. - 216 p.
9. Badwal S.P.S. Electrical conductivity of single crystal and polycrystalline yttria-stabilized zirconia // J. Mater. Sci. - 1984. - V. 19. - P. 1767 - 1776.
10. Filal M., Petot C, Mokchah M., Chateau C, Carpentier J.L. Ionic conductivity of yttriumdopped zirconia and the "composite effect" // Solid state ionics. - 1995. - V. 80. - P. 27 - 35.
11. Rossiter P.L. The electrical resistivity of metals and alloys. Cambridge University Press, 1987. 434 p.

Вісник ХНУ, № 1135, серія «Фізика», вип. 21, 2014. с. 68-70

УДК 539.4.014
PACS 81.70. – q

Soft- and hardware system in devices measuring deformation parameters in solids

A.V. Pakhomov

National Research Center 'Kharkiv Institute of Physics and Technology'
Academichna Str. 1, Kharkiv, Ukraine, 61108
pahomov.and@gmail.com

The research resulted in design and development of an original soft- and hardware system which digitizes the analog signal and provides multichannel data collection from strain gauge sensors on the base of a 32-bit microcontroller. This system allows to conduct mechanical tests of solids for tension (compression), and also to control conditions of an experiment (temperature, magnetic field, etc.). The designed complex also provides determining and studying of activating parameters of plastic flow in metals and alloys at tests for tension. The registration speed of deformation processes can reach about 10^{-3} c^{-1}, and accuracy of measuring no less than 10 bits of useful signal.

Keywords: mechanical tests, strain gauge, microcontroller, ADC, mechanical properties, solid.

Разработан и создан оригинальный программно-аппаратный комплекс оцифровки аналогового сигнала, обеспечивающий многоканальность сбора данных с тензометрических датчиков на базе 32-х разрядного микроконтроллера. Данная система позволяет проводить механические испытания твердых тел на растяжение (сжатия), а также контролировать условия эксперимента (температура, магнитное поле и т.п.). Созданный комплекс также дает возможность определять и изучать активационные параметры пластической деформации в металлах и сплавах при испытаниях на растяжение. При этом скорость регистрации деформационных процессов может составлять порядка 10^{-3} c^{-1} и точность измерений не менее 10 бит полезного сигнала.

Ключевые слова: механические испытания, тензодатчик, микроконтроллер, аналого-цифровой преобразователь, механические свойства, твердое тело.

Розроблений і створений оригінальний програмно-апаратний комплекс оцифрування аналогового сигналу, що забезпечує багатоканальність збору даних з тензометричних датчиків на базі 32-х розрядного мікроконтролера. Ця система дозволяє проводити механічні випробування твердих тіл на розтягування (стискування), а також контролювати умови експерименту (температура, магнітне поле і тому подібне). Створений комплекс також дозволяє визначати і вивчати активаційні параметри пластичної деформації в металах і сплавах при випробуваннях на розтягування. При цьому швидкість реєстрації деформаційних процесів може складати близько 10^{-3} c^{-1} і точність вимірів не менше 10 біт корисного сигналу.

Ключові слова: механічні випробування, тензодатчик, мікроконтролер, аналого-цифровий перетворювач, механічні властивості, тверде тіло.

Preliminaries

When studying mechanical properties and activating parameters of solids, modern science predominantly employs strain gauge systems. The analog signal coming from strain gauges wants amplification, its further recording and processing of the data obtained. Precision of measuring mechanical properties of solids for various types of testing is estimated by means of: the strain coefficient, temperature stability of strain gauges and the signal amplifier, the degree of amplification of the signal being tested, and the choice of analog signal registration system. Existing strain gauge systems of computer diagram registering when testing samples employ signal amplification, for example, with the help of a strain test station with further sending the data to a two-dimensional recorder. Such systems bear certain limitations: record lag, lack of possibility to monitor an experiment and to process diagrams for calculating deformation parameters. This paper is aimed at design and development of an original soft- and hardware system digitizing the analog system and providing multichannel data collection, a desired speed and accuracy of measurements, resistance to temperature drift, displaying diagrams, and possibility to estimate deformation parameters in devices for mechanical testing.

Measuring system

The designed system can be used for measuring load and deformation when testing samples on tension (compression). For registration of load and deformation values we use resilient members shaped as a hollow cylinder or a planar wafer to which strain gauge sensors are glued in a bridge pattern [1]. Data from the sensors are collected by means of a multichannel system which converts the output analog signal from the strain gauge bridge into a digital code. As a result, we get data packets which are transmitted to a PC for further procession. In this process we use original software designed for translation of an obtained digital code into values of load-tension (compression) with further drawing a tension (compression) curve and recording the data in a file to be analyzed in the Origin software.

Figure 1 represents a structural diagram of a two-channel system of digitizing and processing test data.

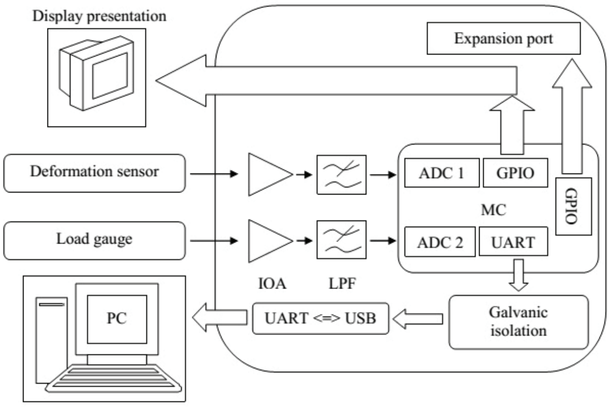

Fig.1. In the structural diagram of the soft- and hardware system LPF stands for low-pass filter, IOA – instrumental operational amplifier, MC – 32-bit microcontroller, ADC – analog-digital converter, GPIO – general purpose input/output, UART – universal asynchronous receiver/transmitter.

Strain gauge sensors are practically always activated in a bridge pattern and glued to the load gauge for temperature compensation on the arms of the strain gauge bridge and for elimination of temperature drift. For accurate measurements metal film strain gauge sensors are most frequently used. Their strain gauge coefficient is considerably lower than that of semiconductors. A distinctive feature of metal strain gauge sensors is a more rigorous linear dependence of variation of resistance on extension and lower temperature drift, which provides better precision in estimating parameters under testing. Since metal strain gauge sensors possess a low strain gauge coefficient, their output signal wants more amplification – about 1,000 times or over. The task set can be effectively solved with the help of instrumental operational amplifiers (IOA), for example, the ones manufactured by Analog Devices [2] and Burr-Brown (TI) companies [3].

Owing to the low value of the tested signal of the strain gauge sensor and the high coefficient of gain in the instrumental operational amplifier, it is rational to employ low-pass filters adjusted to 50 Hz in order to weaken outward interference induction. Further on the amplified and filtered signal goes to the input of an analog-digital converter (with 12-bit capacity and digitization frequency of 1 Msps) built in a 32-bit microcontroller (MC) manufactured, for example, by STMicroelectronics company [4]. After that the outcome gets averaged according to 200 measurements for further formation of data packets and sending them to the Universal Asynchronous Receiver/Transmitter (UART), which virtually reaches a theoretical limit of 2,5 Ksps (corresponds to one measurement in 0.0004 second).

Importantly, the main source of interference induction in a measurement system can be PC power circuits a frequency of 30-200 kHz. To weaken high-frequency interference induction and to protect a PC, the designed system contains an optic isolation implemented in two optically-coupled isolators (for data input into/output from an MC). The isolation physically separates the measuring block of the system from channels of communication with the PC by means of a USB port. To make the process of setting the balance of strain gauge bridges easier, the measurement block contains a graphic display representing tension (compression) curves and current values of the signal entering the ADC.

For a more accurate estimation of mechanical properties of solids in various physical fields and control over the parameters (thermal, magnetic, radiation, etc.) of these fields it seems sensible to upgrade the soft- and hardware system. With this end in view, we have designed an expansion port (GPIO) to which both outer ADC and other devices can be connected. Their modes of functioning are to be set by an algorithm (for instance, switching on/off of a heater at given temperatures, thermal mode, intensity of the magnetic field, radiation intensity, etc.).

Software

To process test curves we use a packet of developed software designed in an object-oriented programming language Delphi and the Origin program. The developed program performs primary data processing: it receives data sent from an MC to a PC, translates them from a digital code into measurands (load-extension) calibrated by standards.

Figure 2 contains the program interface. Most of the interface is taken by the space displaying the curve of samples deformation which is drawn in the course of receiving test data (Point 1). Along the x-axis and the y-axis we get image of values of extension in millimeters and of load in kilograms respectively. Calibrating is carried out with the help of a pop-up menu (Point 2) providing conversion of voltage values in volts into measurands. The program also provides adjustment of digitization speed (Point 3), the desired value of which is translated into a digital code and transmitted to the inner MC register. Further data from the ADC are recorded in a packet to be sent to a PC in a set mode of register interrupt.

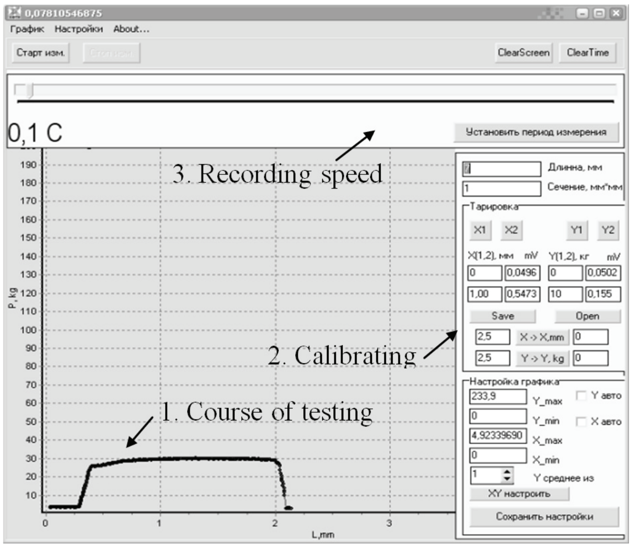

Длинна, мм: 7
Сечение, мм*мм: 1

X(1,2), мм | mV | Y(1,2), кг | mV
0 | 0,0496 | 0 | 0,0502
1,00 | 0,5473 | 10 | 0,155

2,5 X -> X,mm 0
2,5 Y -> Y, kg 0

233,9 Y_max ☐ Y авто
0 Y_min ☐ X авто
4,92339690 X_max
0 X_min
1 Y среднее из

Fig. 2. Interface of the program of data collection and representation on a PC: 1 – space displaying the curve in the course of testing, 2 – the pop-up menu for calibrating, 3 – the interval between two measurements, in seconds.

The array of experimental data is imported to the Origin program for further procession and numerical calculus. Figure 3 contains the interface of the Origin program and deformation curves of steel X18H10T in various structural conditions. Visualized deformation curves can be converted into a format convenient for printing. Basic deformation parameters such as, for example, yield point $\sigma_{0.2}$, rupture point σ_B, total extension ε_o, proportional extension ε_p can be measured automatically.

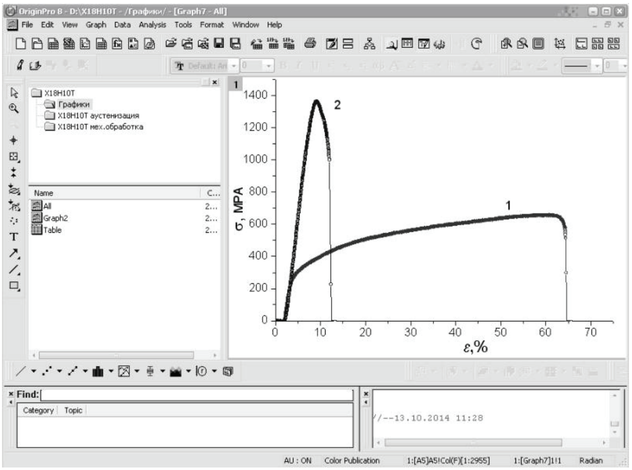

```
//--13.10.2014 11:28
```

Fig. 3. Experimental deformation curves of steel X18H10T processed in the Origin program environment: 1 – austenitic condition, 2 – after rolling deformation.

The developed system of registration of deformation parameters and the software employed also permit measuring and analyzing activation parameters of plastic strain in metals and alloys when tested for tension.

Conclusions

The research resulted in design and development of an original soft- and hardware system digitizing the analog signal which provides multichannel data collection from strain gauge sensors during mechanical tests of solids. Outputting experimental data to a PC enables calculations of deformation and activation parameters of solids.

The given soft- and hardware system provides measurement accuracy of no less than 10 bits of useful signal. The measurement interval can be set within the range of 0,001 ÷ 5 sec with a tuning step of 0,001 sec. The speed of data exchange between the MC and a PC can reach 921600 bps, which provides sufficient speed for registration of deformation processes of about 10^{-3} c^{-1}.

The author would like to express gratitude to Sokolenko V.I. and Volchek O.I. for their interest in the research and valuable advice.

1. Gindin I.A., Kravchenko S.F., Starodubov Ya.D., Chechelnitskiy G.G. И.А., Scientific Instruments and Methods, № 2, 240 (1967).
2. Manufacturer of Electronic Components *Analog Devices* [Electronic resource]: Database. — Access mode: http://www.analog.com/ru/index.html.
3. Manufacturer of Electronic Components *Texas Instruments* [Electronic resource]: Database. — Access mode: http://www.ti.com/.
4. Manufacturer of Electronic Components *STMicroelectronics* [Electronic resource]: Database. — Access mode: http://www.st.com/web/en/home.html.

Вісник ХНУ, № 1135, серія «Фізика», вип. 21, 2014. с. 71-73

PACS 65.40.–b; 75.40.Gb
UDK 537.638.214

Relaxation resonance in magnetic uniaxial crystal during transition from magnetically ordered to paramagnetic state

A.A. Bezlepkin, S.P. Kuntsevich

V.N. Karazin Kharkiv National University,
Svobody Sq. 4, 61022, Kharkiv, Ukraine
anatoliy.a.bezlyepkin@univer.kharkov.ua

Requirements are formulated that allow experimentally observation of the relaxation resonance in the thermal region of second order phase transition in ferromagnets. We show that these requirements can be fulfilled for highly anisotropic hexaferrites of structure type M in alternating magnetic field with frequency in the range 10–120 MHz.

Keywords: the relaxation resonance, a Curie point, phase transition, hexagonal ferrite.

Сформульовано умови, при виконанні яких у феромагнетиках можна експериментально виявити релаксаційний резонанс у температурній області фазового переходу другого роду. Показано, що ці умови можуть бути виконані для високоанізотропних гексаферитів структурного типу М у змінному магнітному полі в інтервалі частот 10–120 МГц.

Ключові слова: релаксаційний резонанс, точка Кюрі, фазовий перехід, гексаферит.

Сформулированы условия, при выполнении которых в ферромагнетиках можно экспериментально обнаружить релаксационный резонанс в температурной области фазового перехода второго рода. Показано, что эти условия могут быть выполнены для высокоанизотропных гексаферритов структурного типа М в переменном магнитном поле в интервале частот 10–120 МГц.

Ключевые слова: релаксационный резонанс, точка Кюри, фазовый переход, гексаферрит.

Introduction

The concept of spontaneous symmetry breaking is the basis for the theory of phase transition of the second kind [1]. Quantity theory was based on the self-consistent field approximation. While it was thought that the order parameter fluctuations are negligible. In [2, 3] it is shown that the fluctuations of the order, even if they are small far away from the transition point, become large near the phase transition. It was found that with the fluctuations increase, when approaching the phase transition point, there must be critical slowing-down of the relaxation parameter order. Theory of critical slowing-down was established in [4]. It was based on the phenomenological assumption that with the fluctuation nature of the phase transition, the critical dynamics of the order parameter is relaxing in nature. It has been shown that with such approval the relaxation time of order parameter τ, when approaching the temperature of transition T_C from lower temperatures, will increase as

$$\tau \sim \frac{1}{T_C - T}, \qquad (1)$$

where T_C – temperature of transition.

For ferro- and ferrimagnets, if the frequency of the external alternating magnetic field ω is less than the relaxation frequency $\omega_r = 1/\tau$ at temperatures T lower Curie temperature T_C, then at the Curie point approaching, in consequence of the critical slowing-down of the relaxation and growth velocity τ, the conditions $\omega\tau = 1$, that correspond to the relax resonance, can be realized [5]. The fact of relaxation response existence can be considered as experimental proof of critical slowing-down of the speed of relaxation order parameter at the fluctuation nature of the phase transition.

This paper outlines the conditions under which you can experimentally detect the critical slowing-down and relaxing resonance in the temperature range of the phase transition of the second kind in ferromagnets.

Magnetic susceptibility in magnetouniaxial crystal

In a multiple-domain magnetouniaxial crystal there are regions of the uniform magnetization – domains and transitional areas – domain boundaries. In highly anizotropic magnetouniaxial crystals domain boundaries volume is 10^3 times less than a volume of domains [6]. This fact suggests that if the orientation of the alternating magnetic field is the direction of easy magnetization the effect of domain boundaries on the processes of magnetization is oblique and their contribution to the magnetic susceptibility value can be neglected.

The equation of motion for the areas of a homogeneous magnetization $\vec{I}$ is [7]

$$\frac{\partial \vec{I}}{\partial t} = -\gamma\left[\vec{I}\times\vec{H}\right]+\vec{R} \tag{2}$$

where $\vec{H}$ – is the effective magnetic field; γ – is the gyromagnetic ratio; $\vec{R}$ – relaxation term.

For the magnetouniaxial crystal with the orientation of the magnetic field $\vec{h}(t)$ and magnetization along the field of the anisotropy the first term on the right side of the expression (1) disappears and the order parameter – magnetization – becomes single. So, the expression (2) takes the form:

$$\frac{dI}{dt} = R, \quad R = \frac{I_p - I(t)}{\tau} \tag{3}$$

where τ is the relaxation time; I_p – equilibrium value of the magnetization, corresponding to the magnetic field at time *t*; $I(t)$ – value of the magnetization, corresponding to the magnetic field at the time t.

The expression (1) is recorded in the model when the magnetization relaxes to the value I_p determined by the instantaneous field value $h(t)$. In this model $h(t)$ changes with frequency ω by the harmonic law

$$h(t) = h_0 e^{-i\omega t}, \tag{4}$$

where h_0 is the amplitude value of the magnetic field.

In consequence of ultimate speed of magnetization processes, $I(t)$ is angle δ behind a phase of a magnetic field

$$I(t) = I_0 e^{-i(\omega t-\delta)}, \tag{5}$$

where I_0 is the amplitude value.

Magnitude $I_p(t)$ can be represented as

$$I_p = \chi_0 h(t) = \chi_0 h_0 e^{-i\omega t}, \tag{6}$$

where χ_0 is the static magnetic susceptibility when $\omega \to 0$.

From relationships (2) – (5) it should be

$$\chi_a e^{-i\delta} = \frac{\chi_0}{1-i\omega\tau}; \quad \chi_a = \frac{I_p}{h_0}. \tag{7}$$

The expression (7) can be represented as

$$\chi' + i\chi'' = \frac{\chi_0}{1+\omega^2\tau^2} + i\frac{\chi_0\cdot\omega\tau}{1+\omega^2\tau^2}, \tag{8}$$

where $\chi' = \chi_a \cos\delta$; $\chi'' = \chi_a \sin\delta$.

$$\chi' = \frac{\chi_0}{1+\omega^2\tau^2}; \quad \chi'' = \frac{\chi_0\cdot\omega\tau}{1+\omega^2\tau^2}. \tag{9}$$

Dependences χ'/χ_0 and χ''/χ_0 from the ωτ under condition when the χ_0 is the constant value, are shown in the figure. 1. As follows from the figure, the magnitude χ″, and consequently relaxation losses are maximal at ω τ =1. Increase of ωτ at fixed frequency and τ growth leads to a monotonous decrease of χ’ and at $\tau \to \infty$ the value $\chi' \to 0$.

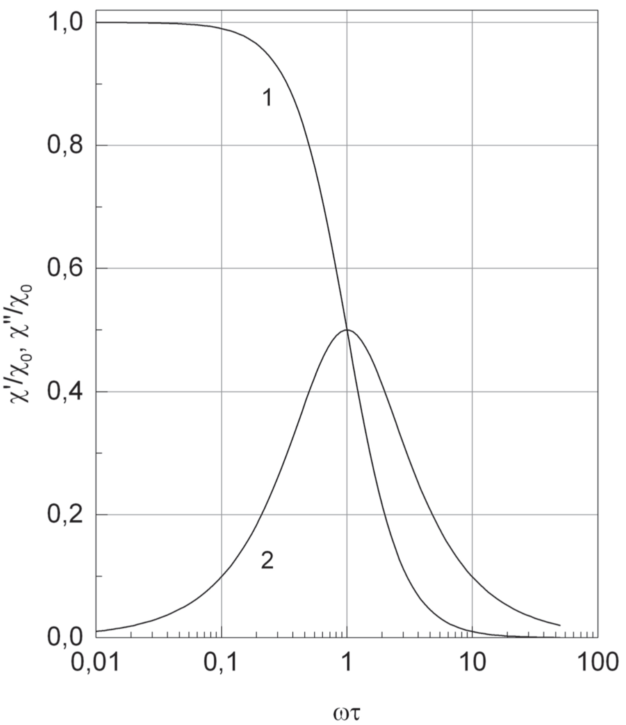

Fig. 1. The dependence of the variable part of the real and imaginary component of magnetic susceptibility on ωτ.

From the expression (1) it follows that the condition ωτ=1 of the relax resonance, you can reach within a narrow temperature range near the Curie temperature. However, for the sample of arbitrary shape and an arbitrary orientation relative to the external magnetic field, will depend on the temperature and intensity of a magnetic field. The condition χ_0=const can be achieved in a determined form magnetouniaxial crystal when demagnetizing field is uniform and oriented along the direction of easy magnetization [8]. In work [9] it is shown that for spherical single crystal gexaferrites with the orientation of the magnetic field along the direction of easy magnetization, the value χ_0 will be determined by the ratio

$$\chi_0 = 1/N = const, \tag{10}$$

where $N = 4\pi/3$ is the demagnetizing factor of the sample.

The condition (10) occurs in magnetic fields $H < NI_S$ (I_S – magnetization of saturation).

In the Curie temperature T_C range the quantity I_S is small and therefore experiments must be realized for small values of $h(t)$.

Considered characteristics point to the principle possibility to detect the relaxation resonance and, respectively, critical slowing-down of relaxation parameter order in magnetouniaxial crystals under alternating magnetic field orientation along the direction of easy magnetization in crystals of a determined form at very small values of alternating magnetic fields. In addition to that for the temperature $T << T_C$ relaxation frequency $1/\tau$ must be greater than the magnetic field change frequency ω.

For hexaferrites of structural type M the width of the FMR curve is 16–80 Oe at room temperature [10, 11 , 12]. To this interval the interval of relaxation frequency 50-230 MHz corresponds. Therefore, the condition $\omega << \omega_r$ when $T << T_C$, can be realized in the radio-frequency range of external magnetic fields 10–120 MHz, when it is possible to use passive LC circuits for small magnetic fields making.

The considered features suggest the possibility to detect relaxation resonance and, accordingly, the critical slowing-down of relaxation of magnetization at highly anizotropic M type ferrites in the temperature range near the Curie temperature.

1. L.D. Landau. ZhJeTF, 7, 627 (1937) (in russian).
2. A. P. Levanjuk. ZhJeTF, 36, 810 (1959), (in russian).
3. V.A. Ginzburg. FTT, 2, 2031 (1960) (in russian).
4. L. D. Landau, N.M. Khalatnikov. DAN SSSR, 96, 469 (1954) (in russian).
5. Fizicheskij jenciklopedicheskij slovar'. Gl. red. A.M. Prohorov, redkol. D.M. Alekseev, A.M. Bonch-Bruevich, A.S. Borovik-Romanov i dr. M.: Sov. jenciklopedija (1984), s. 633(in russian).
6. S.V. Vonsovskij. Magnetizm. Izd-vo Nauka, 1971, 1032 s. (in russian).
7. L.D. Landau, E.M. Lifshic. «Jelektrodinamika sploshnyh sred», Moscow: Nauka (1982) (in russian).
8. G.S. Krinčik. Fizika magnitnyh javlenij. Izd-vo Mosk. un-ta, 1976, 367 p. (in russian).
9. A.A. Bezlepkin, S.P. Kuntsevich, S. P. Palekhin. „Izvestia Vuzov.Physika, N 7, 111 (1987) (in russian).
10. S. Dixon. J. Appl. Phys. 41, 1357 (1970).
11. J.A. Sweschnikow. Nachrichtentechn. Electronik, 26, 262 (1976).
12. A.A. Bezlepkin, S.P. Kuntsevich, V.I. Kostyukov. FTT, 30, N 1, 115 (1997) (in russian)

ІНФОРМАЦІЯ ДЛЯ АВТОРІВ СТАТЕЙ

журналу «Вісник ХНУ». Серія «Фізика»

У журналі «Вісник ХНУ». Серія «Фізика» друкуються статті та стислі за змістом повідомлення, в яких наведені оригінальні результати теоретичних та експериментальних досліджень, а також аналітичні огляди літературних джерел з різноманітних актуальних проблем фізики за тематикою видання.

Мова статей – українська, російська та англійська.

ТЕМАТИКА ЖУРНАЛУ

1. Теоретична фізика.
2. Фізика твердого тіла.
3. Фізика низьких температур.
4. Фізика магнітних явищ.
5. Оптика та спектроскопія.
6. Загальні питання фізики і серед них: методологія та історія фізики, математичні методи фізичних досліджень, методика викладання фізики у вищій школі, техніка та методика фізичного експерименту тощо.

ВИМОГИ ДО ОФОРМЛЕННЯ РУКОПИСІВ СТАТТЕЙ

Загальний обсяг тексту рукопису статті повинен займати не більше, ніж 15 сторінок.

Рукопис статті складається з титульної сторінки, на якій вказанно: назва статті; ініціали та прізвища авторів; поштова адреса установи, в якій була виконана робота; класифікаційний індекс за системами PACS та УДК; анотації на окремому аркуші з прізвищем та ініціалами авторів і назвою статті, викладені українською, російською та англійською мовами; основний текст статті; список літератури; підписи під рисунками; таблиці; рисунки: графіки, фотознімки.

Текст рукопису треба роздрукувати на принтері з подвійним інтервалом на аркуші паперу формату А4 (210x297) з полями ліворуч, праворуч, зверху і знизу по 2,5 см, шрифтом розміром 14 pt гарнітурою TimesNewRoman.

Електронний варіант рукопису статті повинен відповідати таким вимогам: текст рукопису статті повинен бути набраний у форматі MicrosoftWord версії 2003, вирівнювання тексту повинне бути здійснене за лівим краєм, розмір шрифту 10 pt, гарнітураTimesNewRoman, без відступів і виступів, без відступів після абзаців, без прописних букв у назвах, букви звичайні рядкові, накреслення жирного й курсивного шрифту не допускається, формули повинні бути набрані в MathType (не нижче версії 6,5), у формулах кирилиця не допускається, символи з нижніми і верхніми індексами слід набирати в MicrosoftWord, ширина формули не більше 70 мм, графіки та фотографії необхідно подавати в графічному форматі, кольоровий рисунок повинен бути в рукописі чорно-білим (grayscale), розрізнення не менше 300 dpi, поширення файлів повинно бути *.jpg, шириною в одну чи дві колонки, для однієї колонки розміри: завширшки 8 мм, для двох колонок – 16 мм. Масштаб на мікрофотографіях необхідно представляти у вигляді масштабної лінійки.

ВИМОГИ ДО ОФОРМЛЕННЯ ГРАФІКІВ

Товщина ліній не більше 0,5 мм, але не менше 0,18 мм. Величина літер на підписах до рисунків не більш 14 pt , але не менше 10 pt, гарнітура Arial.

ПРИКЛАД ОФОРМЛЕННЯ СПИСКУ ЛІТЕРАТУРИ

1. Л.Д. Ландау, Е.М. Лифшиц. Теория упругости, Наука, М. (1978), 730 с.
2. И.И. Іванов. ФТТ, 25, 7, 762 (1998).
3. A.D. Ashby. Phys.Rev., A19, 213 (1985).
4. D.V. Vert. In Progress in Metals, ed. by R. Speer, USA, New York (1976), v.4, p.17.

ДО РЕДАКЦІЇ НАДАЄТЬСЯ

1. Два роздруковані примірники рукопису статті, які підписані її авторами.
2. Електронна версія рукопису та дані щодо контактів для спілкування з її авторами. Для цього потрібно надіслати електронною поштою, тільки на адресу vestnik_phy@mail.ru.
3. Направлення від установи, де була виконана робота, і акти експертизи у двох примірниках; адресу, прізвище, повне ім’я та батькові авторів; номери телефонів, E-mail, а також зазначити автора рукопису, відповідального за спілкування з редакцією журналу.

Матеріали рукопису статті потрібно направляти за адресою: Редакція журналу «Вісник Харківського національного університету імені В.Н. Каразіна. Серія: фізика», Криловському В.С., фізичний факультет, майдан Свободи, 4, Харківський національний університет імені В.Н. Каразіна. тел. (057)-707-53-83.

Наукове видання

Вісник Харківського національного університету імені В.Н.Каразіна

№ 1135

Серія "Фізика"

випуск 21

Збірник наукових праць

Українською, російською та англійською мовами.

Комп'ютерне верстання С.В. Лебедєв

Підписано до друку 21.11.2014. Формат 60x84 1/8.

Папір офсетний. Друк ризограф. Ум. друк. арк. 8,7. Обл.-вид. арк 13,7.

Тираж 100 пр.

Надруковано: ХНУ імені В.Н. Каразіна
61022, Харків, майдан Свободи, 4.
Тел.705-24-32

Свідоцтво суб'єкта видавничої справи ДК №3367 від 13.01.09